Top Quark Pair Production in ATLAS

Karl Gellerstedt

Stockholm
University

ISBN 978-91-7447-572-2

Printed in Sweden by Universitetsservice AB, Stockholm 2012
Distributor: Department of Physics, Stockholm University

Cover image: ©Gerner Design

Abstract

The Large Hadron Collider (LHC) at the international particle physics laboratory CERN in Switzerland is currently the most powerful particle accelerator on earth. This thesis presents analyses of proton-proton collisions at the energy $\sqrt{s} = 7$ TeV, recorded by ATLAS, one of the detectors at the LHC. The goal of the LHC and its detectors is to find new phenomena not described by the Standard Model (SM) of particle physics.

The top quark is the heaviest known elementary particle and it is produced in very large numbers at the LHC. Measuring the production cross-section of top pairs ($t\bar{t}$) is important for many reasons: for validating the strong production mechanism of the SM, for commissioning and calibration of the detector and analysis software and because several scenarios for physics beyond the SM predict changes to the $t\bar{t}$ production cross-section.

Five different measurements of the $t\bar{t}$ cross-section will be presented in this thesis. The first three are measurements of the total cross-section, the fourth is a simultaneous measurement of the $t\bar{t}$, $Z \to \tau^+\tau^-$ and WW cross-sections and the fifth is a measurement of the *relative differential* $t\bar{t}$ cross-section. The most accurate measurement of the total cross-section is 176 pb with a total uncertainty of 9%, and the relative differential cross-section for $t\bar{t}$ masses above ~ 1 TeV is 0.007 TeV^{-1} with an uncertainty of 43%. Both values agree with the SM predictions.

Measurements or searches in particle physics often have to be conducted in the presence of uninteresting background processes. Reducing and providing estimates of these backgrounds is one of the main analysis tasks. Many backgrounds can be simulated with sufficiently good accuracy. However, the background due to mis-identified leptons cannot be accurately simulated. This thesis presents and evaluates a method for estimating this background from data, and this is then used in the total $t\bar{t}$ cross-section measurements.

Sammanfattning

LHC (Large Hadron Collider) vid det internationella partikelfysiklaboratoriet CERN i Schweiz är för närvarande världens mest kraftfulla partikleaccelerator. I den här avhandlingen presenteras anlyser av proton-protonkollisioner vid $\sqrt{s} = 7$ TeV, registrerade med ATLAS som är en av detektorerna vid LHC. Målet med LHC och dess detektorer är att upptäcka nya fenomen som inte kan beskrivas av partikelfysikens nuvarande standardmodell (SM).

Toppkvarken är den tyngsta elementarpartikeln man känner till och den produceras i stort antal vid LHC. Att mäta produktionstvärsnittet för par av topkvarkar ($t\bar{t}$) är viktigt av flera skäl: för att validera den starka produktionsmekanismen i SM, och för att testa och kalibrera detektorn och analysverktygen. Dessutom förutsäger flera teoretiska utvidgningar av SM ändringar av tvärsnittet för $t\bar{t}$.

Fem olika mätningar av tvärsnittet för $t\bar{t}$ presenteras i den här avhandlingen. De första tre är mätningar av det totala tvärsnittet, den fjärde är en simultan mätning av tvärsnitten för produktion av $t\bar{t}$, WW och $Z \to \tau^+\tau^-$ och den femte är en mätning av det *relativa differentiella* tvärsnittet. Det mest noggranna mätningen av det totala tvärsnittet är 176 pb med 9% total osäkerhet, och det relativa differentiella tvärsnittet för $t\bar{t}$-massor över ~ 1 TeV är $0.007\ \text{TeV}^{-1}$ med 43% osäkerhet. Båda mätresultaten stämmer med respektive förutsägelse från standardmodellen.

Mätningar eller sökningar inom partikelfysiken måste ofta utföras i närvaro av ointressanta bakgrundsprocesser. Att reducera och skatta dessa bakgrunder är en av huvuduppgifterna inom en dataanalys. Många bakgrunder kan simuleras med tillräcklig precision. Men bakgrunden av felidentifierade leptoner kan däremot inte simuleras tillräckligt noggrant. Den här avhandlingen presenterar och utvärderar en metod för att skatta bakgrunden av felidentifierade leptoner från data, och resultatet används i mätningarna av det totala tvärsnittet för $t\bar{t}$.

Contents

Nomenclature

α_S The strong coupling constant, page 16

ΔR $\Delta R = (\phi_1 - \phi_2) \oplus (\eta_1 - \eta_2)$, page 28

η Pseudo rapidity, page 28

γ Photon, page 8

$\mathscr{L}$ Integrated luminosity, page 23

$\sqrt{s}$ Centre of mass energy, page 18

A Effective acceptance, page 41

m_T Transverse mass, page 68

y Rapidity, page 28

$E_{\mathrm{T}}^{\mathrm{miss}}$ Missing transverse energy, page 37

AIDA An Inclusive Di-lepton Analysis, page 87

AOD Analysis Object Data, page 37

ATLAS A large Toroidal LHC ApparatuS, page 23

Barn (b) U unit of area 10^{-24} cm^2, page 23

BLUE Best Linear Unbiased Estimate, page 108

CASE Combination And Systematics Evaluation tool, page 107

CKM Cabibbio-Kobayashi-Maskawa, page 12

CMS Compact Muon Solenoid, page 23

CSC Cathode Strip Chambers, page 34

DAQ Data Acquisition, page 35

DPD Derived Physics Data, page 37

EDM Event Data Model, page 37

EF Event Filter, page 36

EM Electro Magnetic, page 31

EMEC Liquid argon electromagnetic end cap calorimeter, page 32

ESD Event Summary Data, page 37

EWK Electro-weak, page 47

FCal liquid argon forward calorimeter, page 32

FSR Final state radiation, page 17

GUT Grand Unification Theory, page 20

HEC Liquid argon hadronic end cap calorimeter, page 33

hMM High fake rate Matrix Method, page 54

ID Inner Detectors, page 28

ISR Initial state radiation, page 17

JES Jet Energy Scale, page 45

L Instantaneous luminosity, page 23

L1 First level trigger, page 35

L2 Second level trigger, page 36

LAr Liquid Argon electro-magnetic calorimeter, page 31

LHC Large Hadron Collider, page 23

lMM Low fake rate Matrix Method, page 54

LO Leading order, page 17

MC Monte Carlo, page 4

MDT Monitored Drift Tube chambers, page 34

ML Maximum Likelihood, page 42

MS Muon Spectrometer, page 34

NLO Next to Leading Order, page 17

NNLL Next to next to leading log, page 17

PCM Principle of Maximum Conformality, page 115

PDF Parton Distribution Function, page 16

PS Parton Shower, page 17

PS Proton Synchrotron, page 24

QCD Quantum Cromo Dynamics, page 9

QED Quantum Electro Dynamics, page 9

ROI Region Of Interest, page 36

RPC Resistive Plate Chambers, page 34

SCT Semiconductor Tracker, page 29

SM Standard Model, page 7

SPS Super Proton Synchrotron, page 24

SUSY Supersymmetry, page 20

TGC Thin Gap Chambers, page 34

TileCal Hadronic tile calorimeter, page 31

TRT Transition Radiation Tracker, page 30

W $W^{\pm}$ boson, page 8

Z Z^0 boson, page 8

Acknowledgements

First and foremost I would like to thank my supervisors Jörgen Sjölin and Kerstin Jon-And. Jörgen, I am truly grateful for all our discussions, all the things you have explained to me and all every day talk about hundreds of various topics. I admire your patience and your impressive understanding of the subject as well as your ability and willingness to share it with others.

Kerstin, with knowledge and calm, you inspire and bring order into to a chaotic field. Your warm and frequent laughter always tells me that nothing is as difficult as it might seem and that everything is possible.

Jörgen and Kertin, you not only guided and helped me through the PhD process, you are also largely responsible, together with my father and Dave Milstead, for inspiring me to start studying physics in the first place.

I also had the pleasure of having Aras Papadelis as co-supervisor. Aras, you added much skill, quick energy and enthusiasm to the top team at Stockholm University. Working with you was just as easy and rewarding as it was fun.

During my time in the Elementary Particle Physics Group I have shared office, both at Fysikum and CERN, with a number of great people I would like to take my hat of for: Elin Bergeås Kuutman, for technical-, LaTeX- and moral support; Christian Ω, thanks for many fun and uplifting chats, but too bad I've missed your gigs; Marianne Johansen, for bringing much ingenuity and humour to the office; Katarina Bendtz, for doing physics at 200 km/h with max cleverness and curiosity, while managing to keep a healthy distance, and arranging really fun parties; Maja Tylmad and Björn Nordkvist, for sharing a nightmarish flight to Helsinki followed by a good time and hard work; Olle Lundberg, for our common affection for cats; Pawel Klimek, for putting up with all the crap that flows from my side of the desk.

I owe a debt of gratitude to the entire ATLAS group at Stockholm University for accepting me as a student, I hope I have lived up to your expectations. I especially recognise: Sten Hellman, for invaluable input and hard questions; Dave Milstead, for career advice, feedback and for teaching me the essentials of particle physics and Cockney; Torbjörn Moa, for maintaining our computers and our well-spring of life (i.e. the coffee machine). And many thanks to other present and past members of the ATLAS group: Christophe Clément, Barbro Åsman, Sven-Olof Holmgren, Erik Johansson, Sara Strandberg, Björn Sellden, Hyeon Jin Kim, Hovhannes Khandanyan.

I am also thankful for help from Christian Bohm and Sam Silverstein at the System and Instrumentation Physics group at SU, as well as the members of the ICE-Cube group at SU, especially Christian Walck, Chad Finley and Per Olof Hult. Also thanks to Bengt Lund-Jensen, Emma Kuwertz and Jelena Jovicevic in the ATLAS group at KTH.

At CERN I have met several people that I am indebted to: Francesco Spano, for a great co-operation; Sasha Solodkov, for introducing and guiding me through the ATLAS software framework; Daniel Whiteson, for professional co-operation and competition that gave me a better understanding of the fake leptons; Jörgen Dalmau, for lending me his couch in St. Genis and for fun evenings at Charlies; Per Johansson, for making countless meals at R1 enjoyable despite the lousy food; Elias Coniavitis, for realising that we actually are related. And greetings to Thomas Burgess, Johan Lundberg and Karl-Johan Grahn for shared interest in the finer arts (Chip/SID music, programming etc.).

I would also like to thank my dear Amanda and my parents Eva and Gunnar for all their help and backing: Amanda for putting up with my strange habits and working hours, and for reminding me about the world outside physics; my mother for believing in me and my father for inspiring me, giving technical help, and for proofreading this thesis. And many warm thanks and greetings to the rest of my family and to my friends.

Finally, my thoughts go to Thomas Gerner, the creator of the wonderful art on the cover of this thesis. Thank you for all great gigs, parties, travels, laughs and talks. Dear friend, I miss you.

1 About this thesis

1.1 Overview

This thesis is a work in the field of high energy physics. Studying physics at high energies means studying nature at a small scale; it is the study of particles, their properties and how they interact with each other. Understanding physics at the small scales is important for understanding the universe as a whole. Some of the questions one wants to answer are for instance: What happened at the very early moments in the life of the universe? How do the fundamental particles obtain their masses? What is the so called dark matter that, from cosmological observations, is estimated to be far more abundant than ordinary matter in the universe?

Some particle physicists study high energy particles produced in nature, e.g. in satellite experiments that measure gamma rays or in ground based neutrino telescope experiments. Other physicists *create* high energy particles in laboratories and study what happens when these particles collide, which is the topic of this thesis. Currently, the best picture of particle physics is contained in the theory called the Standard Model (SM). The basics of this theory is presented in chapter 2.

The Large Hadron Collider (LHC) is a particle accelerator at the European organization for nuclear research, CERN, located in Geneva Switzerland. Chapter 3 gives an overview of this huge machine and the detectors used to study collision processes. All data used in this thesis were collected with ATLAS, one of the detectors at LHC, during 2010 and 2011 when the LHC operated at the energy $\sqrt{s} = 7$ TeV. The ATLAS detector is described in chapter 4.

One of the main goals of LHC and ATLAS is to find evidence for the existence of “new physics", i.e. new particles and phenomena not described by the SM. The top quark, predicted by the SM, was discovered in 1995; its large mass makes it difficult to produce and when produced it decays rapidly. At the LHC it will be abundantly produced, thus understanding the properties of the top quark is of great importance for several reasons. The top quark final state is complicated, with a high multiplicity of particles and jets and a high total energy. Because of its large mass, the top quark physics at the LHC probes a high energy region of phase space never before explored. This is demanding for both the detector hardware and the software. Before one can make statements about heavier or more rare particles, the top quark and its decay has to be understood. The strong production mechanism in the Standard Model has

to be tested to see if higher order (more accurate) theoretical computations are needed to predict the cross-section and its dependency on kinematic variables. Related to this are the tests of parton distribution functions (PDF:s) and parton shower models at a new energy level.

In searches for new particles, top quark production is likely to be a significant background that has to be estimated with the highest possible precision. But top quarks may also be an important part of a discovery process or measurement of new phenomena. One possibility is that new heavy particles decay to top quarks or top antitop quark pairs. Another highly relevant point, in light of the observation at the LHC of a new boson that shares many properties with the long sought Higgs boson, is that the top quark should couple very strongly to the mass generating mechanism. To establish if the new boson is indeed the Higgs boson, its couplings to top quarks must be investigated.

Chapter 5 gives an introduction to measurements on top quarks, in particular the measurement of the production cross-section for a top antitop quark pair ($t\bar{t}$). Event and object selections as well as backgrounds and sources of uncertainties are presented.

The rapid decay of the top quark means that it is not the particle itself but its decay products that are observed in the ATLAS detector, and the same holds for many other particles in the SM as well as hypothetical new particles. Based on the decay products one defines an *event signature*. This thesis treats event signatures with one or two leptons: the single lepton and the di-lepton final states. Several processes give rise to the same signature, some of them interesting (signal) and others of no interest (background).

A background process that is difficult to model is the background due to mis-identified leptons, more commonly referred to as the *fake lepton* background. Starting from the signal processes of interest, an ideal *signal lepton* is defined. However, the measured data sample will contain leptons from other sources and they are referred to as fake leptons. A general method for dealing with this background is presented in chapter 6, and the resulting method is applied in four different cross-section measurements: three measurements of the $t\bar{t}$ total cross-section, summarized in chapter 7, and one simultaneous measurement of the $t\bar{t}$, $Z \rightarrow \tau^+\tau^-$ and WW cross-sections, summarised in chapter 8. The total cross-section is an important quantity to measure since the presence of new particles or phenomena is likely to affect the value.

When enough data has been collected and the analysis machinery has matured, the focus changes from total cross-sections to differential cross-sections, i.e. the cross-section measured as a function of some variable. Presently unknown particles and new phenomena that affect the top quark production may change the *shape* of the $t\bar{t}$ differential production cross-section in some variable, without altering the total cross-section significantly. A new resonance decaying to $t\bar{t}$ may also give a “peak" in the cross-section spectrum. A measurement of the $t\bar{t}$ differential cross-section is summarized in chapter 9.

1.2 Aim

The aim of the work behind this thesis is to measure the top quark pair ($t\bar{t}$) total and differential production cross-sections as accurately as possible. This is done in the semi- and di-leptonic channels, i.e. the measurements are made in final states with exactly one or exactly two leptons. In order to measure the cross-section in a final state with leptons, the background due to fake leptons must be estimated. A fundamental requirement on the method is that is should be adaptable to the particulars of a certain analysis; it should be able to provide estimates in such a way that the background can be given as a histogram in any variable of interest, in a region of phase space given by variable cuts. It should also be possible to validate the obtained fake lepton estimate in a control region.

Concerning the differential cross-section measurement, the aim is to provide a measurement with as low uncertainty as possible, that can be used outside of the ATLAS collaboration. This means that the result must be *unfolded*, i.e. translated to a common theoretical context. In this way the results may be directly compared to new physics scenarios, without having to simulate the entire ATLAS detector.

1.3 Contributions from the author

This thesis is a summary of five articles, Papers I–V, containing measurements of $t\bar{t}$ cross-sections.

For the total cross-section measurements, summarized in chapter 7, the main contributions from the author were fake lepton estimates, described in chapter 6. The method was developed, implemented and executed by the author, with substantial help from my supervisors and other members of the ATLAS top working group. In order to estimate the fake lepton background, most of the analysis chain must be implemented with the exception of the cross-section computation and some systematic uncertainties. The fake lepton method was applied to three successively larger datasets, with some small adjustments of the details of the method. For the first paper on $t\bar{t}$ observation and cross-section measurement in ATLAS from the first $3pb^{-1}$ of data, the method referred to as the *weighting method* in paper I and the *low rate matrix method* in chapter 6, was implemented and executed by the author. The result was used as a cross check in the final analysis:

- **Paper I [1]** The ATLAS Collaboration, "Measurement of the top quark-pair production cross section with ATLAS in pp collisions at $\sqrt{s} = 7$ TeV", *Eur.Phys.J.* **C71** (2011) 1577

The high rate matrix method, described in chapter 6, was used as primary di-lepton fake lepton background estimate to the $t\bar{t}$ cross-section analyses in Papers II–IV:

- **Paper II [2]** The ATLAS Collaboration, "Measurement of the top quark pair production cross section with ATLAS in pp collisions at $\sqrt{s} = 7$ TeV in dilepton final states", ATLAS-CONF-2011-034 (2011)
- **Paper III [3]** The ATLAS Collaboration, "Measurement of the top quark pair production cross section in pp collisions at $\sqrt{s} = 7$ TeV in dilepton final states with ATLAS", *Phys.Lett.* **B707** (2012) 459-477
- **Paper IV [4]** The ATLAS Collaboration, "Measurement of the cross section for top-quark pair production in pp collisions at $\sqrt{s} = 7$ TeV with the ATLAS detector using final states with two high-pt leptons", *JHEP* **1205** (2012) 059

In addition to the cross-section analyses, the results from high rate matrix method were also used in the following published top quark measurements:

- The ATLAS Collaboration, "Measurement of $t\bar{t}$ production with a veto on additional central jet activity in pp collisions at $\sqrt{s} = 7$ TeV using the ATLAS detector" [5]
- The ATLAS Collaboration, "Observation of spin correlation in $t\bar{t}$ events from pp collisions at $\sqrt{s} = 7$ TeV using the ATLAS detector" [6]

For the measurement of the differential $t\bar{t}$ cross-section, I made significant contributions in terms of producing analysis level histograms, for data as well as Monte Carlo (MC) simulations with all systematic uncertainties. All data and MC comparison plots were made by me. The combination and uncertainty propagation toolkit, called CASE, was developed in Stockholm, but I made only marginal contributions to this. The analysis is summarised in chapter 9 and the paper has been submitted to EPJC:

- **Paper V [7]** The ATLAS Collaboration, "Measurements of top quark pair relative differential cross-sections with ATLAS in pp collisions at $\sqrt{s} =$ 7 TeV"

The small timing calibration software described in section 4.8 was implemented in the ATLAS software framework by me, but the original algorithm was developed by colleagues from Stockholm University.

This thesis is an extension of my licentiate thesis [8]. Chapters 2, 3 and 4 were taken from the licentiate thesis with some alterations, and the same is true for chapter 8. Most of chapter 6 was taken from the licentiate thesis, but results for 689 pb^{-1} were added, and many plots were omitted.

Part I:
Theory

2 The Standard Model of particle physics

2.1 Overview

All known matter is made up of a rather small number of different elementary particles. Atoms are made up of a nucleus consisting of neutrons and protons, surrounded by electrons. However, neither the neutron, nor the proton are fundamental, they are made up of quarks.

After several decades of experimental and theoretical work by particle physicists, a picture called the Standard Model has emerged. The material in this chapter was mostly taken from references [9], [10], [11], [12] and [13].

2.2 Leptons

The electron is an electrically charged and stable particle with two heavier cousins, the muon and the tauon (or simply tau) also charged. Each charged lepton has an associated electrically neutral neutrino. Neutrinos and charged leptons are collectively referred to as *leptons*.

Neutrinos have very small, but nonzero, observable mass. Muons and tauons are unstable particles. Both muons and taus are produced in nature, for instance when cosmic radiation interacts with our atmosphere, and muons can be observed at the earth's surface. Table 2.2 summarizes the properties of the charged leptons.

Particle	Symbol	Mass (MeV)	Life time (s)
Electron	e^-	0.511	Stable
Muon	μ^-	105.7	$2.2 \cdot 10^{-6}$
Tauon	τ^-	1780	$2.9 \cdot 10^{-13}$

Table 2.1: The charged leptons and their properties.

All leptons are *fermions*, i.e. they have half integer spin (quantum number), in this case with value 1/2. Every particle has a corresponding antiparticle, with the same mass as the particle but with opposite charge.

2.3 Quarks

Protons and neutrons, the building blocks of all atomic nuclei, are composite particles and their constituents are called quarks. The proton contains two up quarks and one down quark, and the neutron contains one up and two down quarks. Table 2.3 summarizes the quarks and their properties; they are grouped in three families of increasing mass. Quarks carry electric charge and just like leptons they are fermions with spin 1/2, and they have antiparticles.

All particles containing quarks are called *hadrons* and particles with two quarks, one quark and one antiquark, are called *mesons*, e.g. pions. Particles containing three quarks, like the proton and the neutron, are called *baryons*.

The top quark is the heaviest known elementary particle with a lifetime of only $5 \cdot 10^{-23}$ *s*, too short for it to hadronize, i.e. form a hadron together with another quark. All other quarks can hadronize, although the hadrons often have short lifetimes. A top quark does nearly always decay to a W-boson and a b-quark.

Fam.	Particle	Q	Mass (GeV)	Particle	Q	Mass (GeV)
1	Up	2/3	$2.3^{+0.7}_{-0.5} \cdot 10^{-3}$	Down	-1/3	$4.8^{+0.7}_{-0.3} \cdot 10^{-3}$
2	Charm	2/3	1.275 ± 0.025	Strange	-1/3	0.095 ± 0.005
3	Top	2/3	173.5 ± 1.0	Bottom	-1/3	4.18 ± 0.03

Table 2.2: The quarks and their properties. Q denotes the charge in units of the electron charge.

2.4 Forces

There are three fundamental forces of nature described by the SM. Each force has mediator particles which are all *bosons*, that is they have integer spin, in fact they all have spin 1:

- The electromagnetic force is mediated by the massless photon (γ). The photon couples to particles with electric charge.
- The weak force is mediated by the massive intermediate vector bosons, $W^{\pm}$ and Z^0. The vector bosons couple to particles with weak isospin charge. In weak interactions, only particles (antiparticles) that are left handed (right handed) take part. For left (right) handed particles the spin projection onto the momentum vector is negative (positive).
- The strong force is mediated by the massless gluon (g). Gluons couple to particles with color charge. Quarks carry colour charge, while antiquarks carry anticolour charge and gluons themselves carry both a colour and an anticolour charge, which means that gluons couple to each other.

In addition to these three forces, there is the gravitational force, not included in the SM. At currently accessible small distances the other forces are much

stronger than the gravitational force, and it is in most cases ignored in particle physics computations. It is however believed that at some very high energy scale, the strength of the gravitational force will be equal to that of the other forces.

2.5 Conservation laws

Three types of charges have so far been mentioned: the electric charge, the weak isospin charge and the strong colour charge. These charges are conserved in all reactions. Energy, momentum and angular momentum are also conserved in all interactions.

Lepton number is a set of three quantum numbers, one for each lepton family. The electron and the electron neutrino has +1 electron-lepton number while the antiparticles have -1. The same holds for muons with muon-lepton number and tau with tau-lepton number. Lepton numbers are approximately conserved in all interactions.

Quark flavour, i.e. type of quark, is approximately conserved in strong and electromagnetic interactions, but *not* in weak interactions. Not even the quark family, see Table 2.3, is conserved in weak interactions. However, the number of quarks is approximately conserved. This means that mesons have quark number 0 and baryons have +3 or -3. To simplify things a *baryon* number is introduced, which is +1 for baryons, -1 for antibaryons and 0 for all mesons. Baryon number is approximately conserved in all reactions.

2.6 A quantum field theory of particles

In essence, the original SM is a quantum field theory that mathematically describes all the above mentioned fermions, bosons and their interactions except that neutrinos are considered massless. Assuming zero neutrino masses is a good approximation in most cases. The SM consists of a number of matter fields and gauge fields together with a set of symmetries that give rise to interactions between the fields or to conservation laws. One field, not corresponding to a particle already mentioned, is introduced to generate masses for both bosons and fermions (except neutrinos): the Higgs field.

The part of the SM that describes strong interactions is called Quantum Cromo Dynamics (QCD) and the part describing the electromagnetic interactions is called Quantum Electro Dynamics (QED). The electromagnetic and the weak forces are unified in the SM into a theory known as the electro-weak theory.

Fermions are described by Dirac (spinor) fields, denoted by ψ, that are split in left and right handed parts (ψ^L and ψ^R). Left handed charged lepton and the corresponding neutrino spinors are grouped in weak isospin doublets, in

anticipation of the introduction of the weak force:

$$\Psi_l^L = \begin{pmatrix} \psi_{\nu_l}^L \\ \psi_l^L \end{pmatrix}$$

l is an index over the three lepton families $\{(e,\mu_e),(\mu,\nu_\mu),(\tau,\nu_\tau)\}$. A similar procedure is applied to quark fields, where left handed up type quark fields are grouped with the corresponding down type quark fields. The picture is complicated by the fact that quarks come in three different colours:

$$u_q = (\psi_{u,q}^r, \psi_{u,q}^g, \psi_{u,q}^b)^T \qquad d_q = (\psi_{d,q}^r, \psi_{d,q}^g, \psi_{d,q}^b)^T \qquad \Psi_q^L = \begin{pmatrix} u_q^L \\ d_q^L \end{pmatrix}$$

q is an index over the three quark families $\{(u,d),(c,s),(t,b)\}$.

The SM lagrangian is required to have the following symmetries:

- Global Poincaré symmetry: Invariance under translations, rotations and boosts in space-time. Leads to conservation of energy, momentum and angular momentum.
- Global gauge $U(1)\otimes SU(2)\otimes SU(3)$ symmetry: Leads to conservation of charges: electric, weak isospin, color and weak hypercharge.

A lagrangian determining the dynamics of the Dirac fields for the leptons can be written as (spinor indices are suppressed):

$$\mathcal{L}_L = \bar{\Psi}_l^L i\not{D}\Psi_l^L + \bar{\psi}_l^R i\not{D}\psi_l^R + \bar{\psi}_{\nu_l}^R i\not{D}\psi_{\nu_l}^R$$

$\not{D}$ is a shorthand for $\gamma_\mu D^\mu$ where the Einstein summation convention applies for repeated indices. Invariance of $\mathcal{L}_L$ under the local gauge transformations $U(1)\otimes SU(2)\otimes SU(3)$ is ensured by the *covariant derivatives*:

$$\begin{aligned} D^\mu \Psi_l^L &= \left(\partial^\mu + \frac{ig}{2}\tau^a W_a^\mu - \frac{ig'}{2}B^\mu\right)\Psi_l^L \\ D^\mu \psi_l^R &= \left(\partial^\mu - \frac{ig'}{2}B^\mu\right)\psi_l^R \\ D^\mu \psi_{\nu_l}^R &= \partial^\mu \psi_{\nu_l}^R \end{aligned}$$

τ_{jk}^a are three generators of $SU(2)$. The introduced real vector field B_μ (defined to be $SU(2)$ invariant) and three real vector fields W_μ^a (defined to be $U(1)$ invariant) describe the electro-weak bosonic fields before symmetry breaking. After symmetry breaking, linear combinations of the fields will describe the gauge bosons γ, Z and $W^\pm$:

$$\begin{pmatrix} A^\mu \\ Z^\mu \end{pmatrix} = \begin{pmatrix} \cos\theta_w & \sin\theta_w \\ -\sin\theta_w & \cos\theta_w \end{pmatrix}\begin{pmatrix} B^\mu \\ W_3^\mu \end{pmatrix}$$

$$W_\mu^+ = \frac{1}{\sqrt{2}}(W_\mu^1 - iW_\mu^2) \qquad W_\mu^- = \frac{1}{\sqrt{2}}(W_\mu^1 + iW_\mu^2)$$

where θ_w is the Weinberg weak mixing angle and A^μ the electromagnetic field. All lepton fields, B_μ and W_μ^a are $SU(3)$ singlets, invariant under global $SU(3)$ transformations. Left (right) handed lepton fields are $SU(2)$ doublets (singlets).

The lagrangian for quarks, that participate in both electro-weak and strong interactions, is:

$$\mathcal{L}_Q = \bar{\Psi}_q^L i\not{D}_{jk}\Psi_q^L + \bar{\psi}_{u_q}^R i\not{D}\psi_{u_q}^R + \bar{\psi}_{d_q}^R i\not{D}\psi_{d_q}^R$$

The quark lagrangian $\mathcal{L}_Q$ must also be invariant under local $U(1)\otimes SU(2)\otimes SU(3)$ gauge transformations:

$$\begin{aligned} D^\mu \Psi_q^L &= \left(\partial^\mu + \frac{ig\tau_j}{2}W_j^\mu + \frac{ig'}{6}B^\mu + ig_s G_a^\mu T^a\right)\Psi_q^L \\ D^\mu u_q^R &= \left(\partial^\mu + \frac{ig'2}{3}B^\mu + ig_s G_a^\mu T^a\right)u_q^R \\ D^\mu d_q^R &= \left(\partial^\mu - \frac{ig'}{3}B^\mu + ig_s G_a^\mu T^a\right)d_q^R \end{aligned}$$

where G_a^μ are the 8 (indexed by a) gluon fields and T^a are 8 generators of $SU(3)$.

To complete the lagrangian describing fermions and their interactions through bosons, suitable terms for the bosonic fields must be added:

$$\mathcal{L}_B = -\frac{1}{4}B_{\mu\nu}B^{\mu\nu} - \frac{1}{8}W_{\mu\nu}^i W_i^{\mu\nu} - \frac{1}{2}G_{\mu\nu}^a G_a^{\mu\nu}$$

where field strength tensors (B,W and G) have been introduced for the gauge bosons. Apart from containing kinetic terms, they also describe self interactions among the bosons. These fields must also be invariant under the local gauge transformations.

The final part of the SM consists of mass terms for both fermions and bosons. Simply adding boson mass terms will lead to theory that is *non-renormalizable*. Renormalizability is a desired property of a fundamental theory of nature. Adding lepton mass terms will violate gauge invariance because of the different properties of left and right handed lepton fields under $SU(2)$. The solution is to introduce a new weak isospin doublet field, the Higgs field, invariant under $SU(3)$:

$$\Phi = \begin{pmatrix} \phi_a \\ \phi_b \end{pmatrix}$$

with dynamical terms:

$$\mathcal{L}_H = (D^\mu\Phi)^\dagger D_\mu\Phi - \mu^2\Phi^\dagger\Phi - \lambda(\Phi^\dagger\Phi)^2 \tag{2.1}$$

The covariant derivative for the Higgs field is defined as:

$$D^{\mu}\Phi = \left(\partial^{\mu} + \frac{ig'}{2}B^{\mu} + \frac{ig\tau_j}{2}W_j^{\mu}\right)\Phi \tag{2.2}$$

From this it is clear that the Higgs field couples to the electro-weak bosons. Masses for the electrically charged fermions are generated by introducing Yukawa like couplings between the Dirac fields and the Higgs field. Neutrinos are considered massless in the original SM, but the charged leptons couple directly to the Higgs field, with coupling constants g_l:

$$\mathcal{L}_{LH} = -g_l(\bar{\Psi}_l^L \psi_l^R \Phi + \Phi^{\dagger}\bar{\psi_l^R}\Psi_l^L)$$

The corresponding terms for quarks are more complicated because the electro-weak and strong quark eigenstates (u_q, d_q) are *not* the same as the physical particles or quark mass eigenstates (u'_q, d'_q). This is manifested in the flavor changing weak interactions. Instead of a single Yukawa coupling constant per particle, two 3×3 matrices ($Y^d_{qq'}$, $Y^u_{qq'}$) are needed:

$$\mathcal{L}_{QH} = -(Y^d_{qq'}\bar{\Psi}^L_q d^R_{q'}\Phi + Y^{d*}_{qq'}\Phi^{\dagger}\bar{d}^R_q\Psi^L_{q'} + Y^u_{qq'}\bar{\Psi}^L_q u^R_{q'}\tilde{\Phi} + Y^{u*}_{qq'}\bar{u}^R_q\tilde{\Phi}^{\dagger}\Psi^L_{q'})$$

With $\lambda > 0$ and $\mu^2 < 0$ in the dynamical terms for the Higgs field eq. (2.1), the $U(1)\otimes SU(2)$ symmetry is broken spontaneously. The Higgs field is parametrized around its nonzero vacuum expectation value:

$$\Phi = \langle 0|\Phi|0\rangle + \frac{1}{\sqrt{2}}\begin{pmatrix} 0 \\ \sigma \end{pmatrix} = \frac{1}{\sqrt{2}}\begin{pmatrix} 0 \\ (-\mu^2/\lambda)^{1/2} + \sigma \end{pmatrix} = \frac{1}{\sqrt{2}}\begin{pmatrix} 0 \\ v+\sigma \end{pmatrix}$$

which leads to mass terms for the weak bosons by eq. (2.1) together with eq. (2.2), while the photon remains massless. σ is the Higgs scalar field. To get the masses for the physical quarks, the matrices $Y^d_{qq'}$ and $Y^u_{qq'}$ are diagonalized by the matrices V:

$$M^u = \frac{v}{\sqrt{2}}V_L^u Y^u V_R^{u\dagger} \qquad M^d = \frac{v}{\sqrt{2}}V_L^d Y^d V_R^{d\dagger}$$

Masses of the up-type quarks are given by the diagonal of the matrix M^u and the same for down-type quarks from M^d. The couplings of the weak fields to physical quarks are now given by the Cabibbio-Kobayashi-Maskawa (CKM) mixing matrix:

$$V_{CKM} = V_L^u V_R^{d\dagger}$$

The final SM lagrangian is then the sum of the above specified terms:

$$\mathcal{L}_{SM} = \mathcal{L}_B + \mathcal{L}_H + \mathcal{L}_L + \mathcal{L}_Q + \mathcal{L}_{LH} + \mathcal{L}_{QH} + h.c. \tag{2.3}$$

In addition to the symmetries the SM is required to have, it also possesses some other approximate symmetries: All quark fields together have a global

$U(1)$ symmetry which leads to the approximate conservation of baryon number. Lepton fields possess three approximate global $U(1)$ symmetries, one for each family, leading to the approximate conservations of electron, muon and tauon lepton numbers. These quantum numbers are only approximately conserved according to the SM because of nonperturbative effects, the Adler-Bell-Jackiw anomalies [14]. However, because these anomalies will only come into effect at very high energies, the baryon and lepton numbers can be considered good quantum numbers at the currently accessible energies.

The SM lagrangian is split in a part describing free fields and a part describing interactions among the fields. In a scattering process, the interaction part is treated as a perturbation of initial ($\vec{i}$) and final states ($\vec{f}$), which are eigenstates of the free field. The probability amplitude for a particular process is $\langle f|S|i\rangle$ where S is the *scattering* matrix, determined by a Dyson series expansion of the interaction lagrangian.

A short cut to the computations of the S-matrix was developed by R. Feynman. The idea is to draw diagrams of the possible interactions, corresponding to different terms in the series expansion, given initial and final states. The nodes and edges in the diagrams correspond to factors in the S-matrix terms. Feynman diagram pieces will be shown in the following sections for some of the interactions mentioned above. Complete leading order Feynman diagrams of important processes are shown later in this thesis. In leading order diagrams, only the first term in the series expansion is shown.

2.6.1 Electromagnetic interactions

Figure 2.1 shows the basic electromagnetic interaction vertex. Any electrically charged particle, i.e. quark, W boson or charged lepton, couples to the photon.

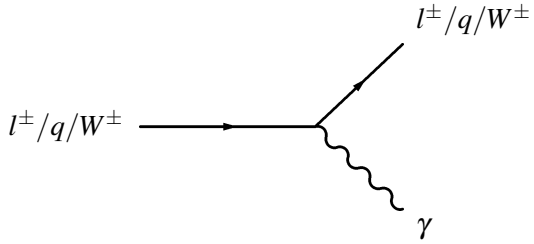

Figure 2.1: Basic electromagnetic interaction

2.6.2 Weak interactions

The weak interaction vertices are shown in Figure 2.2. Charged antileptons are denoted by l^+ and other antiparticles by a symbol with a bar, e.g. $\bar{q}$ for an antiquark. One striking feature of the weak force is that it can transform charged leptons into their corresponding neutrino and an up type quark (of

charge 2/3) to a down type quark (of charge -1/3), or the other way around; this is an example of quark flavour violation, or quark mixing, in weak interactions. The weak force is mediated by the intermediate vector bosons Z^0, W^+ and W^-. As indicated, the $W^\pm$ bosons are charged while the Z boson is electrically neutral.

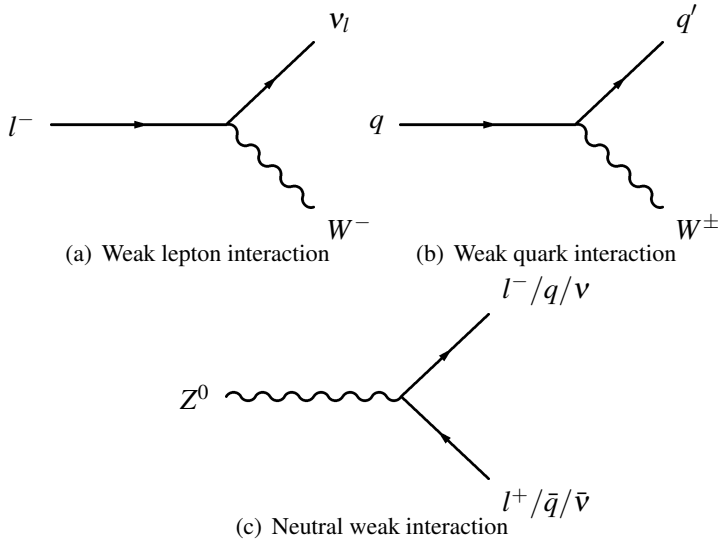

(a) Weak lepton interaction (b) Weak quark interaction

(c) Neutral weak interaction

Figure 2.2: Basic weak interactions

Production of Z bosons in proton-proton collisions, and the subsequent decays to two charged leptons is an important process in the analysis described in later chapters.

In the SM, the electromagnetic and the weak forces are unified, which means that the two theories are different manifestations of the same underlying theory. One of the consequences is that there is an interaction between bosons from the weak and the EM forces, shown in Figure 2.3

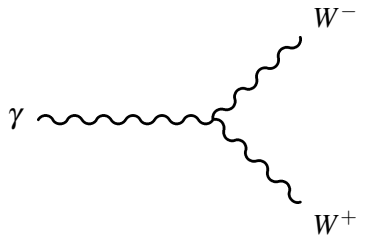

Figure 2.3: Interaction between photons and W bosons

2.6.3 Strong interactions

As mentioned above, the gluon couples to colour charged particles, which means quarks and gluons. Figure 2.4 shows the basic string interaction vertices; most notably are the gluon self interaction vertices shown in Figures 2.4(c) and 2.4(b).

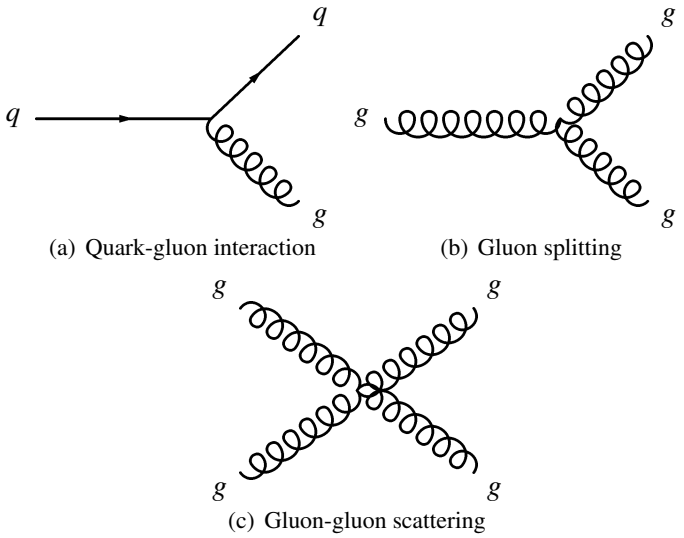

(a) Quark-gluon interaction (b) Gluon splitting

(c) Gluon-gluon scattering

Figure 2.4: Basic strong interactions

The strong interaction is responsible for binding quarks into hadrons. Contrary to the electromagnetic force that decreases with distance, the strong force *increases* with distance. All observable hadrons are colour singlets, implying that they are colour neutral and since quarks always carry colour, this has the effect that there are no free quarks. If for instance a quark inside a proton obtains momentum, say in a proton-proton collision, a strong colour field is created between the quark and the proton remnants. When the energy stored in the field is strong enough, a quark-antiquark pair is created from vacuum and a meson is formed with the single quark and a baryon with the proton remnants. This is an example of a phenomenon called *hadronization*.

2.6.4 The Higgs boson

Higgs couples to particles with mass, the heavier the particle the stronger the coupling. At small Higgs masses (< 200 GeV) the branching ratio to $b\bar{b}$ and $\tau^+\tau^-$ dominate, but for higher masses the branching fraction to W^+W^-, ZZ and $t\bar{t}$ dominate. Another final state of interest for small masses is the $\gamma\gamma$ with

a small branching ratio on the one hand, but a clean signal on the other. Higgs does not couple directly to photons, because photons are massless, but the photons are emitted in a one loop diagram of W or top, shown in Figure 2.5.

One of the motivations for building LHC and its experiments was to search for this particle. In recent results from both ATLAS [15] and CMS [16], a new boson with a mass of about 126 GeV is observed.

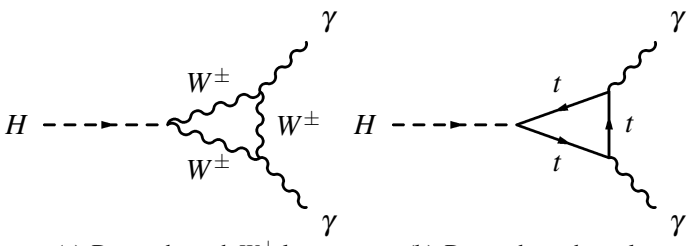

(a) Decay through $W^{\pm}$ loop (b) Decay through top loop

Figure 2.5: Decay of Higgs to $\gamma\gamma$ through W and top quark loops.

2.7 Computations for hadron colliders

At hadron colliders, the colliding particles are composite. This thesis only deals with proton collisions, so this section will handle this case exclusively. Protons are made up of three valence quarks and a number of sea *partons*, where a parton is either a quark or gluon. The QCD interactions that bind the quarks together inside a proton must be low energy processes, otherwise the proton would decay. The proton momentum is split between its partons, sea and valence; the fraction for a given type cannot be computed in perturbative QCD, it has to be measured. The parton distribution function, PDF for short, $f_i(X, Q^2)$, gives the probability for finding a parton of flavour i with a fraction of the proton momentum in the interval x to $x + dx$, at an energy scale of Q^2.

Perturbative QCD does not work below energy scales of about 1 GeV; in the low energy limit the strong coupling constant α_S becomes larger than one. Because of this, the PDF:s contain a non perturbative part that has to be estimated from measurements, typically from deep inelastic scattering experiments. This non perturbative part is then evolved to some higher energy scale by adding soft or collinear parton emissions.

The hard scattering process is what is often of interest. A hard scattering process, in the high energy physics context, is a process with such a high momentum transfer that it can be treated entirely perturbatively [17, 18]. The partonic cross-section ($\hat{\sigma}$) consists of the hard scattering between two initial state partons, and it is evaluated in perturbative QCD. This has to be folded with the PDF:s to compute a hadronic cross-section (σ), the quantity that is

actually measured in a hadron collider since there are no free partons:

$$\sigma = \sum_{ij} \int dx_1 dx_2 f_i(x_1, Q^2) f_j(x_2, Q^2) \hat{\sigma}(x_1, x_2, Q^2)$$

Because there are no complete analytic expressions available for the PDF:s, the cross-section expression must be integrated numerically. The integration can either be done in a dedicated cross-section integrator such as HATHOR [19] or MCFM [20], or an event generator such as PYTHIA [21], MC@NLO[22], ALPGEN[23] or HERWIG[24] [25].

Both initial and final state partons emit radiation, mainly in QCD processes because the strong coupling is greater than the coupling for QED, but electromagnetic radiation is also possible, e.g. emission of photons from quarks. Radiation from an initial state parton is called initial state radiation (ISR) and the corresponding emissions from final state partons is called final state radiation (FSR). ISR and FSR are treated in several different ways: resummed leading logarithm cross-sections, partons shower (PS) MC and explicit matrix elements. The advantage of the two latter, implemented in event generators, is that the changed event kinematics due to the radiation, is treated correctly.

Resummation and parton showers will include radiation effects to all orders in the soft and collinear limit, with the strong coupling evaluated at a fixed order. The MC integrator HATHOR computes cross-sections with resummation at NNLL (next to next to leading log)+NLO (next to next to leading order) precission. NNLL means that resummation is performed with NNLO accuracy. NLO means that the partonic cross-section ($\hat{\sigma}$) includes diagrams with one power more of α_S compared to leading order (LO)[1], i.e. diagrams with one real emission or one loop.

Parton shower simulation is implemented in the event generators PYTHIA and HERWIG; although they differ in implementation details, they both approximate the effects of soft and collinear emissions with Monte Carlo methods.

Event generators with extra matrix elements for radiation, such as ALPGEN, include tree level diagrams with emissions of up to about five extra partons, in the high energy and wide angle region.

Parton shower and matrix element evaluation with extra radiation complement each other. The former deals with the low energy region, while the latter handles the high energy emissions. There might be an overlap between the two, so merging procedures have to be implemented. In ALPGEN this is done with a procedure called MLM [23].

All emitted partons, both from the hard matrix element and parton shower, will undergo hadronization because they are not colour singlets, see section 2.6.3. Both PYTHIA and HERWIG have phenomenological models of the formation of final state hadrons that make up jets.

[1]Leading order diagrams contain the smallest possible number of vertexes to make a transition from desired initial to final states.

2.8 Top-antitop pair production

At the LHC energy of $\sqrt{s} = 7$ TeV and above, top quark pairs are mainly produced through gluon fusion or gluon scattering while production through quark annihilation is suppressed. Figure 2.6 shows leading order Feynman diagrams for the $t\bar{t}$ production through gluon fusion (2.6(a)), gluon scattering (2.6(b)) and quark annihilation (2.6(c)). The three different decay channels are shown: di-leptonic (2.6(a)), semi-leptonic (2.6(b)) and all hadronic (2.6(c)). The branching ratio to the di-lepton final state is small (6.5%), but it provides a clean event topology with a high signal to noise ratio. The branching fraction for $t \to Wb$ is assumed to be 100%.

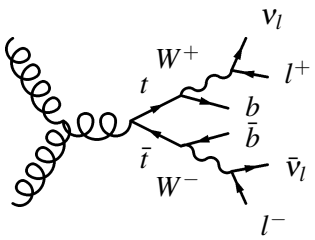

(a) $t\bar{t}$ production through gluon fusion with di-leptonic decay

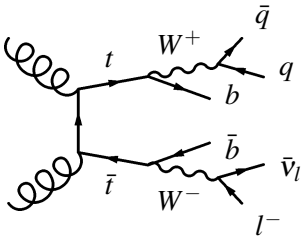

(b) $t\bar{t}$ production through gluon scattering with semi leptonic decay

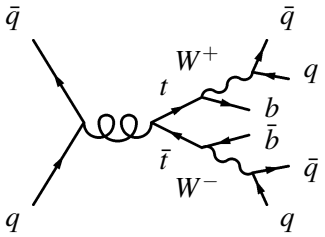

(c) $t\bar{t}$ production through quark annihilation with all hadronic decay

Figure 2.6: $t\bar{t}$ production diagrams with three decay channels.

2.8.1 Expected cross-section

For the analyses in this thesis, the $t\bar{t}$ signal is mainly simulated with the event generator MC@NLO [22, 26, 27]. As the name suggests, this is done at next to leading order (NLO) accuracy. Figure 2.7(a) shows the theoretical cross-section versus centre of mass energy ($\sqrt{s}$) for proton-proton collisions, computed with HATHOR using the parton distribution function set CTEQ66 [28]. Uncertainties are from both PDF variations together with renormalization and factorization scale variations.

The production cross-section is highly dependent on the top mass, which is shown in Figure 2.7(b). A top mass of 172.5 GeV has been used in all

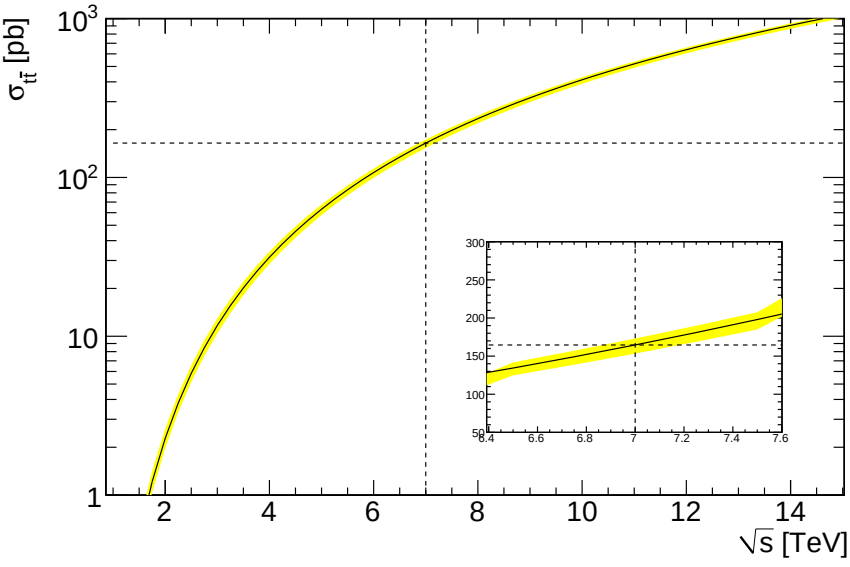

(a) Total $t\bar{t}$ cross-section as a function of energy

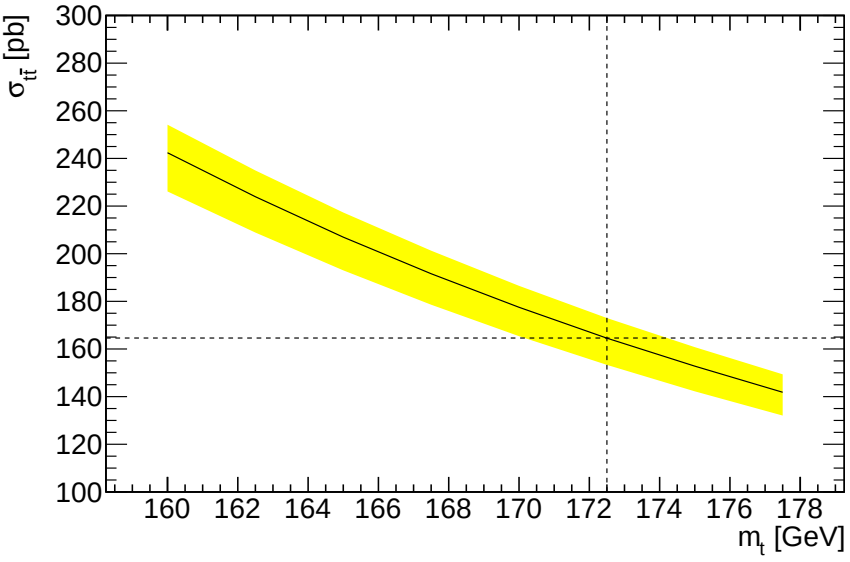

(b) Total $t\bar{t}$ cross-section versus top mass

Figure 2.7: Expected total $t\bar{t}$ cross-section computed at near NNLO using HATHOR.

simulations. This value differs from the currently best measurement of the mass (173.5 [12]) and the reason for choosing to simulate at this particular mass is to be able to compare the result to other measurements.

The total cross-section from the NLO generator MC@NLO differs slightly from the more accurate result from HATHOR, which is why a *k-factor* is introduced. This factor simply scales the event weights from MC@NLO in such a way that the total cross-section agrees with the result from HATHOR.

2.9 Beyond the Standard Model

There are several problems with the SM described in the previous section:

- There is no quantum field theory for general relativity.
- The electro-weak and strong forces are not unified, their coupling constants do not tend to some common value at high energies. Any theory that *do* unify these three forces is called a *Grand Unification Theory* (GUT).
- There is experimental evidence for non-zero neutrinos masses, but the SM describes massless neutrinos.
- The observed baryon asymmetry between matter and antimatter cannot be quantitatively described by the CP violating parts of the SM alone.
- Cosmological observations suggests the existence of *dark matter* in the universe, needed to describe large scale gravitational effects. But the SM does not provide enough candidate particles that could make up this matter. The matter is said to be dark because it emits no detectable electromagnetic radiation.
- The SM Higgs is described by a scalar field, but it is unclear if such a fundamental scalar field exists[2]. It is possible that the Higgs mechanism is just an effective low energy manifestation of a more fundamental theory.

2.9.1 Supersymmetry

One of the most popular extensions to the SM is Supersymmetry (SUSY). The idea behind SUSY is a proposed symmetry between fermions and bosons in such a way that every SM fermion should have a boson super partner and vice verse for every SM boson. It has been shown, in reference [29], that this is the *only* symmetry left to impose on the four dimensional SM. Both Poincaré and local $U(1) \otimes SU(2) \otimes SU(3)$ symmetry have been exploited and no significant deviation from their predictions has been observed. SUSY may provide particles that can solve, at least partially, the problem of dark matter.

[2]The spin of the observed new boson has not yet been determined.

Part II:

The experiment

3 The Large Hadron Collider

3.1 Overview

The Large Hadron Collider (LHC) is the most powerful particle accelerator in the world today. It has been built to explore physics beyond the Standard Model and to make more precise measurements of already discovered particles and processes. The accelerator, shown in Figure 3.1, is located near the city of Geneva in Switzerland and it is housed in a 27 kilometre long circular tunnel, 100 meters below ground.

When the LHC is fully commissioned it will be able to accelerate two proton beams to such velocities that each proton has an energy of 7 TeV, which gives a centre of mass energy of 14 TeV. Currently energy of each proton is a world leading 4 TeV, although the analysis presented in this thesis use data for proton collisions as 3.5 TeV. In addition to protons, the LHC has also accelerated and collided heavy ions (lead).

Besides the energy of the protons, the most important property of the beam is the instantaneous luminosity:

$$L = \frac{fkN_1N_2}{4\pi\sigma_x\sigma_y} \tag{3.1}$$

where f is the orbit frequency, k the number of colliding bunches, N_i the number of protons in each bunch and σ_x (σ_y) the horizontal (vertical) beam size at the collision point. This formula assumes that the proton bunches collide head on, but at the LHC the bunches collide at a small crossing angle. The target instantaneous luminosity of the LHC is $10^{34}\ cm^{-2}s^{-1}$ or $10\ nb\ s^{-1}$, where a barn (b) is $10^{-24}\ cm^2$. The analyses in this thesis uses the time integral of L, the integrated luminosity:

$$\mathscr{L} = \int L dt$$

In reality, this quantity is measured, details can be found in reference [30].

There are four main experimental locations around the accelerator ring. The two general purpose detectors are ATLAS (A large Toroidal LHC ApparatuS) and CMS (Compact Muon Solenoid). Both names refer to the magnet type used for the respective experiment; ATLAS uses a system of large toroid magnets to create the magnetic field required to measure the momentum of muons and CMS uses a solenoidal magnet for the same reason. The other two experiments are special purpose detectors; LHCb studies b-hadrons in search for new physics and ALICE is designed to search for new physics in heavy ion collisions.

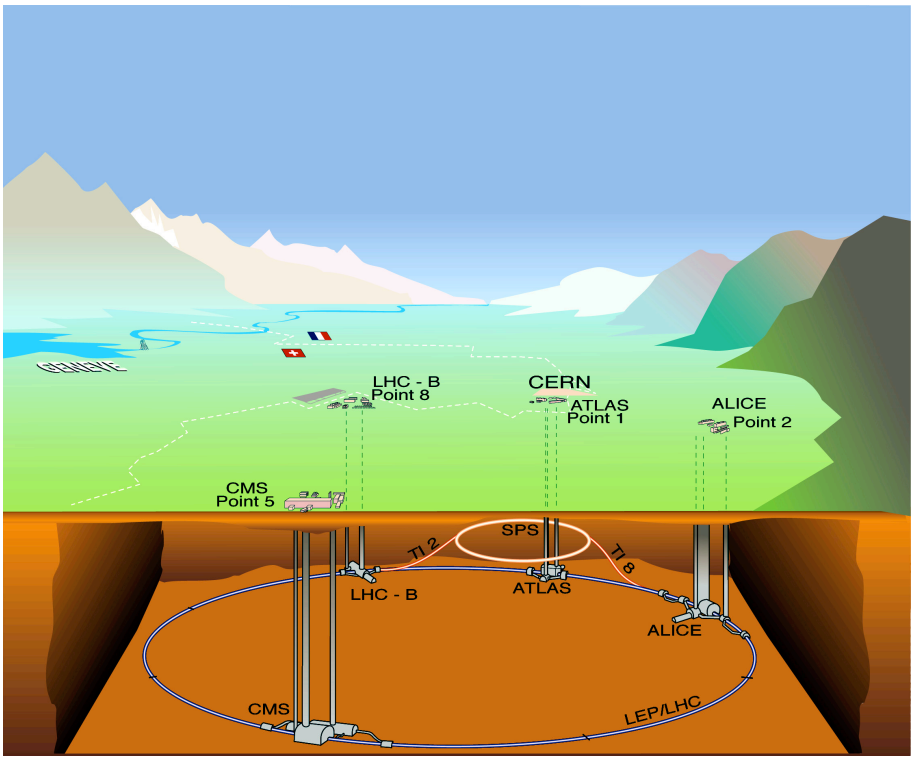

Figure 3.1: Overview of the LHC accelerator and its experiments

3.2 The accelerator

In order to reach the final energies of the protons, a highly complex chain of accelerators is required. Figure 3.2 shows a simplified overview of the LHC accelerator complex.

Protons are injected into the main LHC accelerator from the Super Proton Synchrotron (SPS) at an energy of 450 GeV, per proton. The proton beam is not homogeneous, the protons are lumped together in *bunches*. The SPS is, in turn, fed by 20 GeV protons from the Proton Synchrotron (PS). The PS accelerates the 50 MeV protons it receives from Linac2 to 20 GeV. LHC, SPS and PS are all circular accelerators while Linac2 is a linear accelerator.

The beams in LHC are kept in orbit by 1232 superconducting dipole magnets cooled to 1.9K by liquid Helium. To bend the beam sufficiently at these energies, a 8 T field is required. A number of multipole magnets are required to focus the beam, especially at the four interaction points.

As can be seen from eq. (3.1) the luminosity increases with the square of the number of protons in each bunch, so when one wishes to increase the luminosity is it important to raise this number as high as possible. But besides technical difficulties with creating and maintaining a beam with more protons in each bunch, another effect becomes a problem; as the number of protons

increase, so does the probability for multiple collisions which is referred to as *pile-up* collisions.

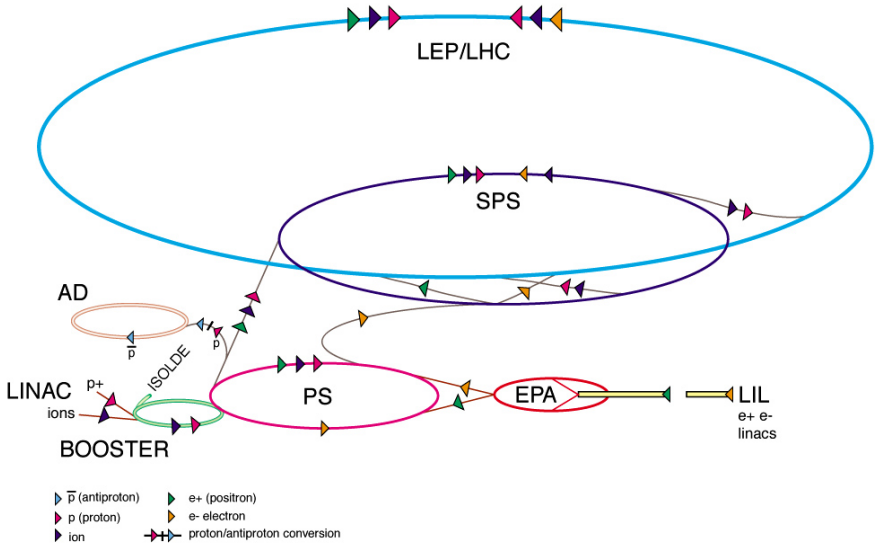

Figure 3.2: LHC accelerator complex

4 The ATLAS detector

4.1 Overview

ATLAS is a general purpose particle detector, designed to observe and measure Standard Model signals as well as signals from new physics. This chapter will give a brief overview of the detector and its sub detectors, further details can be found in reference [31].

With a weight of about 7000 tonnes, a radius of 11 meters and a total length of 44 meters, the detector is truly a giant. Figure 4.1 shows an overview of the detector. Innermost, starting from the interaction point, is the inner detector that consists of three parts: the Pixel detector, the Transition Radiation Tracker (TRT) and the Semiconductor Tracker (SCT), all contained in a superconducting solenoid magnet. The solenoid produces a 2 Tesla magnetic field that is essential for momentum measurements of charged particles, one of the primary functions of the inner detector. Outside the solenoid surrounding the inner detector are the calorimeters situated. Furthest out is the muon spectrometer which measures the momentum of muons. This system is built inside a toroid magnet.

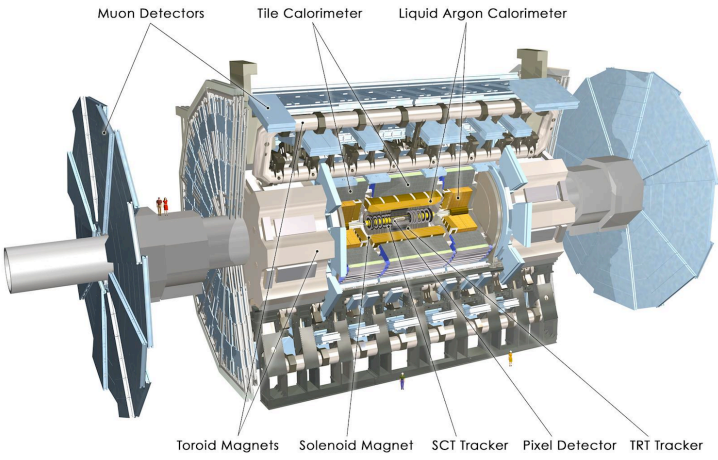

Figure 4.1: The ATLAS detector

4.2 Geometry and coordinate system

To describe directions and positions of objects in the detector and collision products it is common to use a cylindrical or spherical system of coordinates, besides a standard Cartesian coordinate system. The x axis of the Cartesian system is directed along the LHC radius towards the centre, the y axis is directed upwards and the z axis is directed along the beam line and the origin is in the ideal collision point, i.e. the mid point of ATLAS.

As the total energy and momentum in a parton collision is unknown, one can only use the fact that the total transverse momentum, i.e. the momentum perpendicular to the beam axis (z), is approximately zero. Therefore, the four-momentum of an object is given in the coordinates η, ϕ, p_T and E, where η is the pseudo rapidity, related to the elevation angle θ, the angle in the y-z plane, by:

$$\eta = -\ln\tan(\theta/2), \tag{4.1}$$

ϕ is the azimuthal angle in the plane perpendicular to the z (beam) axis. p_T is the transverse component of the three momentum. For massive objects such as jets, the *rapidity*(y) is used instead of the pseudo rapidity:

$$y = 1/2\ln\left(\frac{E+p_z}{E-p_z}\right) \tag{4.2}$$

The products from collisions are approximately evenly distributed in η, which is why most of the cells of the hadronic calorimeter have the same width (0.1) in η.

A commonly used quantity is the angular distance ΔR between two four-vectors, defined as:

$$\Delta R = (\phi_1 - \phi_2) \oplus (\eta_1 - \eta_2) \tag{4.3}$$

where

$$a \oplus b = \sqrt{a^2 + b^2}$$

4.3 Inner detectors

The purpose of the inner detectors (ID) is to measure the tracks left by charged particles as they pass through and interact with the material of the detector. Information about the tracks is used to determine momentum, impact parameter and vertex position.

Because of the Lorentz force, any charged particle that passes through a magnetic field will experience a force perpendicular to the field and the velocity. The 2T field produced by the solenoid is directed along the z axis which means that charged particles will bend in the transverse plane. The momentum of the particles are determined by the bending radius of the reconstructed tracks.

Figure 4.2 shows the inner detector with its three sub detectors, and Figure 4.3 shows a schematic view of the inner detector layers and their distances from the beam pipe. The entire detector covers $|\eta| < 2.5$. The track momentum resolution can be parametrized as:

$$\frac{\sigma}{p_{\mathrm{T}}} \sim 3.8 * 10^{-4} p_{\mathrm{T}}[GeV] \oplus 0.015$$

where σ denotes the standard deviation of the momentum. The resolution increases, i.e. worsens, with inceasing p_{T}.

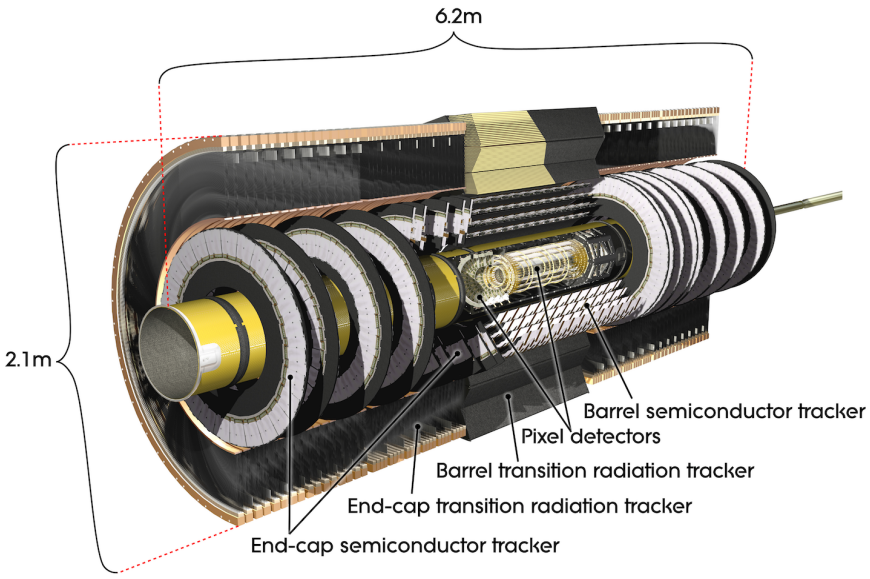

Figure 4.2: The ATLAS inner detectors

4.3.1 Pixel detector

With a total of over 80 million silicon pixel diodes, the Pixel detector provides good position measurements and track separation. Each pixel has an area of 40 by 500 μm and the silicon has a thickness of 250 μm. In the central barrel region there are three layers of pixel detectors. The innermost layer, called the B-layer, is only 5 cm from the center of the beam pipe. On each side of the barrel are five disks of pixel modules.

4.3.2 Semiconductor tracker

The Semiconductor tracker (SCT) is made up of four layers of silicon micro strip detectors in the barrel and 9 disks in each end cap. In total there are 6.5 million readout channels. Instead of pixels the detector is based on silicon

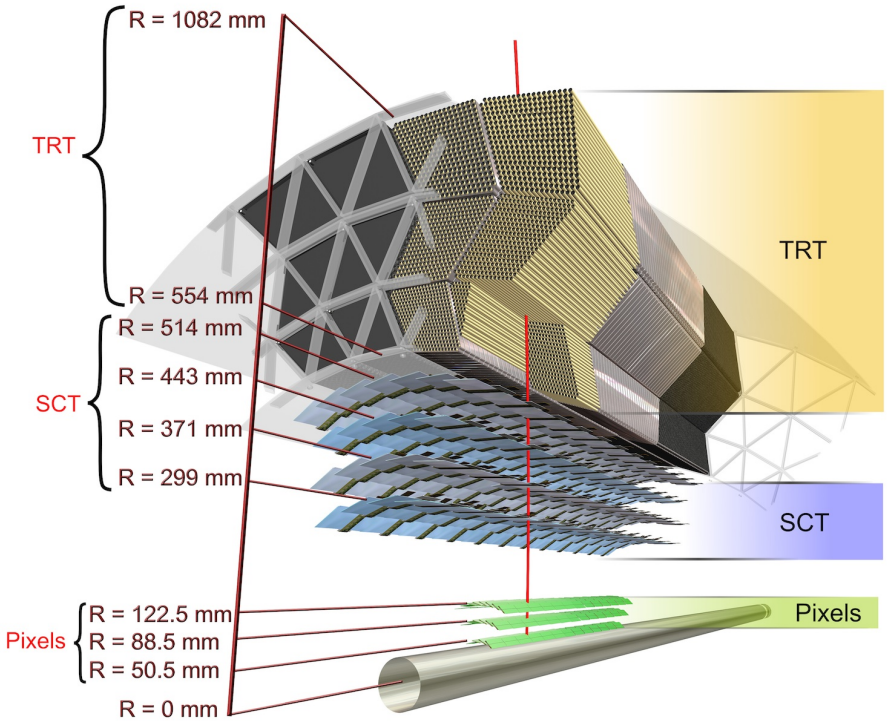

Figure 4.3: The ATLAS inner detectors and their distances from the beam pipe

strips. Each layer consists of two sub layers of silicon plates with strips, with a small angle between each layer to be able to measure the z-position of the hit.

4.3.3 Transition radiation tracker

The Transition Radiation Tracker (TRT) is made up of thin drift tubes, or *straws*. The straws are 4mm in diameter with a 30 μm gold plated tungsten wire at its center. There are about 50 000 straws in the barrel parallel to the beam pipe, each divided in two parts and read out at each end. In the end cap there are about 320 000 straws, perpendicular to the beam pipe.

Between the straws there is material with varying refractive indices. Charged and highly relativistic particles, i.e. particles with a speed close to the speed of light, passing between two materials of different refractive indices will radiate transition radiation photons. The straws contain a gas

mixture with 70% Xenon that can detect the transition radiation. There are thus two types of hits in the TRT, the ordinary hits from charged particles and the detection of transition radiation, which leaves a higher signal. The latter is referred to as high threshold hits. The goal is to be able to discriminate between charged hadrons and electrons that leave the most transition radiation of the two. About 36 hits in the TRT are expected for each track.

4.4 Calorimeters

The calorimeter system of ATLAS consists of several subsystems, Figure 4.4 shows an overview. In the barrel region the innermost calorimeter is the Liquid Argon electro-magnetic calorimeter (LAr), primarily designed to measure the energy of electrons and photons. Outside the LAr calorimeter is the hadronic tile calorimeter (TileCal), which primarily measures the energy of hadronic jets. All calorimeters in ATLAS are sampling calorimeters, i.e. they only measure part of the shower that develops in the detector when particles interact with the material. Part of the detector is high Z absorber material and the rest is active material.

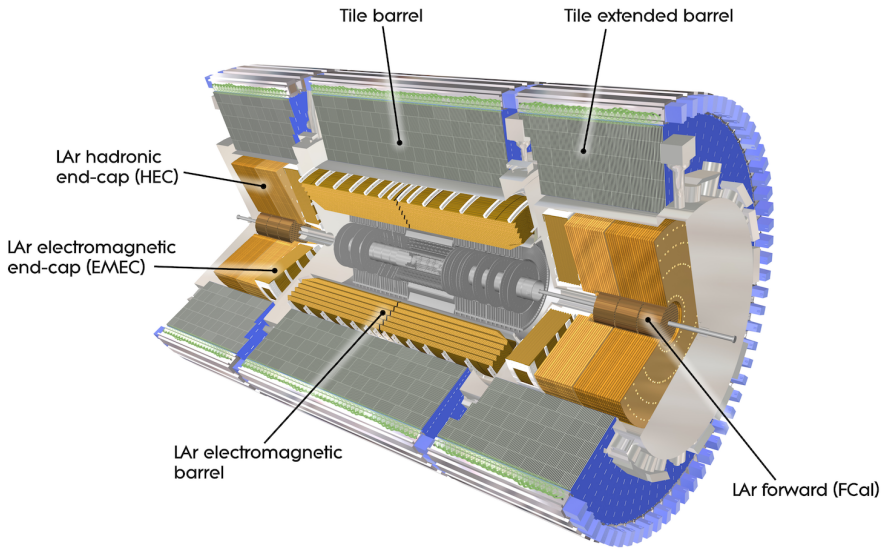

Figure 4.4: The ATLAS calorimeters

4.4.1 Electromagnetic calorimeters

Figure 4.4 shows an overview of the calorimeters in ATLAS. In the central part, covering $|\eta| < 2.5$ is the LAr barrel calorimeter that is divided in two

parts. The coverage of the electromagnetic calorimeter extends in $|\eta|$ up to 3.2, with the liquid argon electromagnetic end cap calorimeter (EMEC), and up to 4.9 with the liquid argon forward calorimeter (FCal).

The LAr barrel part consists of three layers with decreasing granularity, shown in Figure 4.5. Layer 1 consists of strips that extend $0.0245 * 4$ in the ϕ direction and with a width in η of 0.0031. The detector is made up of accordion shaped lead absorbers with surrounding liquid Argon as active material together with copper electrodes. To measure energy losses in the material in front of the calorimeter, a presampler has been installed that covers the region $|\eta| < 1.8$. The presampler is an 11 mm thick layer of liquid Argon.

The FCal consists of three parts shaped as wheels, the innermost is an electromagnetic calorimeter and the two outer are hadronic. FCal is located in the same cryostat as the EMEC.

The energy resolution for the electromagnetic calorimeters is approximately:

$$\frac{\sigma}{E} = \frac{10\%}{\sqrt{E}}$$

which means that the resolution decreases with increasing energy, i.e. it gets better, in contrast to the momentum resolution of the inner detector, c.f. section 4.3.

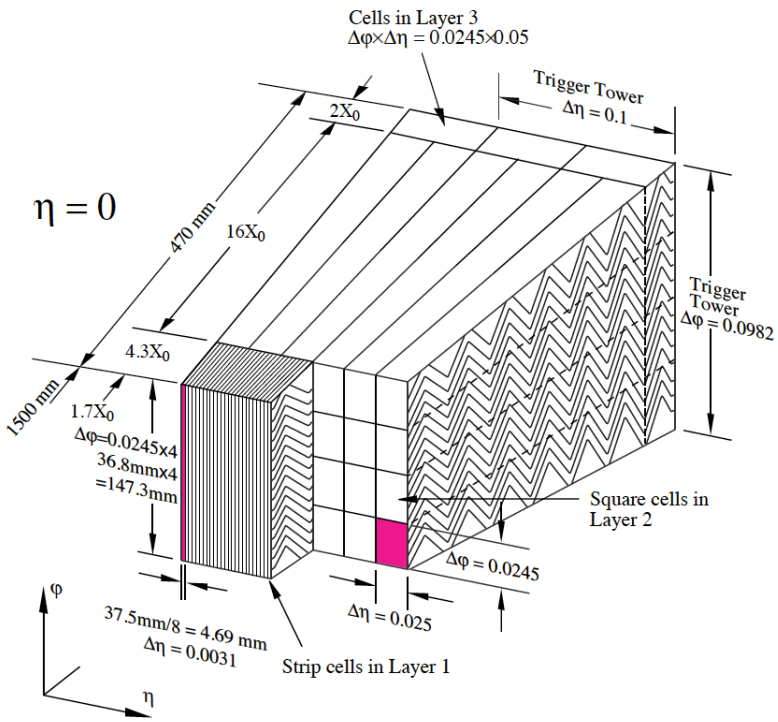

Figure 4.5: Details of the electromagnetic liquid Argon calorimeter

4.4.2 Hadronic calorimeters

Hadronic calorimetry in ATLAS is provided in the interval $|\eta| < 1.7$ by TileCal, in $1.5 < |\eta| < 3.2$ by the liquid argon hadronic end cap (HEC) and up to $|\eta| < 4.9$ by the FCal. The different hadronic calorimeters are shown in Figure 4.4.

TileCal consists of a barrel part and two extended barrels. Iron tiles are used as absorbers and the active detecting material consists of plastic scintillator tiles. TileCal has 256 modules, 64 in each extended barrel and two times 64 in the barrel. Figure 4.6 shows details of a module. The geometry of the modules in the extended barrel and the barrel are slightly different. The scintillator tiles are grouped together in cells, 48 in each barrel module with three in depth. The cells are read out through plastic fibres and the signal measured with photomultiplier tubes located at the back of each module. The front end electronics is located next to the photo multipliers and includes a signal shaper and digitizer boards containing AD-converters and pipeline memories.

The energy resolution for the hadronic calorimeters is approximately:

$$\frac{\sigma}{E} = \frac{50\%}{\sqrt{E}} \oplus 0.03$$

As with the electro magnetic calorimeter, the resolution improves with increased energy.

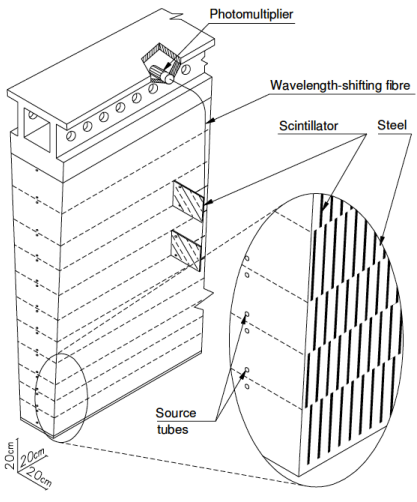

Figure 4.6: Details of the hadronic Tile calorimeter

4.5 Muon spectrometer

The ATLAS muon spectrometer (MS) measure charged particles that manages to pass through the calorimeters. In the barrel region, covering $0 < |\eta| < 2.7$, precision tracking chambers are located in between eight coils of the toroidal superconducting magnet. The precision tracking chambers consist of monitored drift tube chambers (MDT) in the region $0 < |\eta| < 2.7$, except for the innermost end cap layer where the MDT's cover $0 < |\eta| < 2.0$ and $2.0 < |\eta| < 2.7$ is covered by Cathode Strip Chambers (CSC). Each MDT chamber contains several layers of drift tubes, from three to eight. The CSC:s are multiwire proportional chambers and they are used because of their capacity for higher rates and better time resolution.

The muon system provides dedicated muon triggers, by using Resistive Plate Chambers (RPC) in the barrel region $0 < |\eta| < 1.05$ and Thin Gap Chambers (TGC) covering $1.05 < |\eta| < 2.4$.

The expected momentum resolution is less than 10% for muon energies up to 1 TeV.

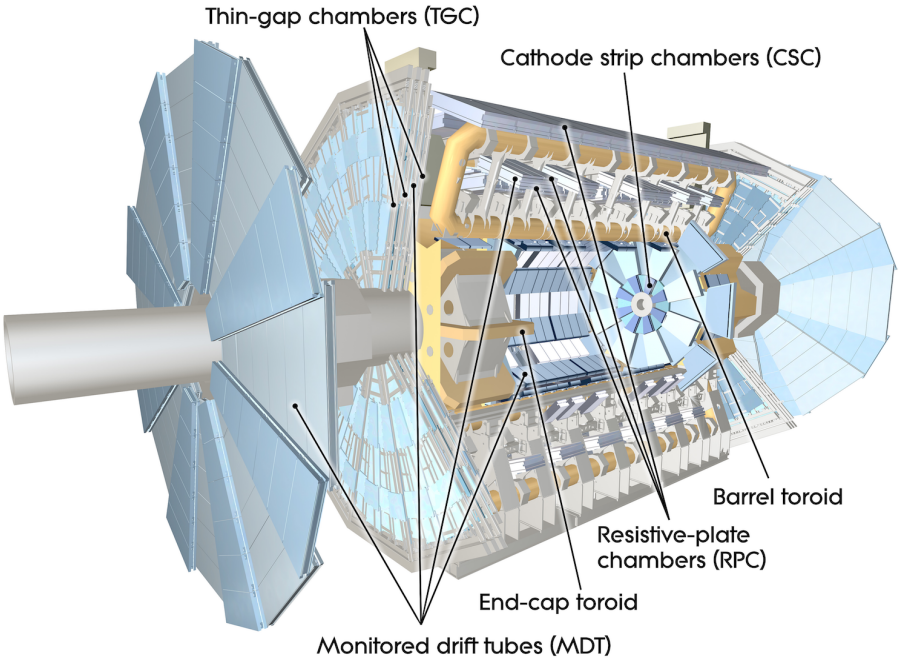

Figure 4.7: The ATLAS muon system

4.6 Trigger and data acquisition

When the LHC has reached its intended target luminosity of $10^{34}\ cm^{-2}s^{-1}$, the bunch crossing frequency, i.e. the collision frequency in the interaction points, will be 40 MHz. However, only a tiny fraction of these collisions will result in interesting processes. Finding these collisions is the responsibility of the trigger system, while the data acquisition (DAQ) system is responsible for keeping, transferring and storing data from all detectors for the collisions deemed interesting by the trigger.

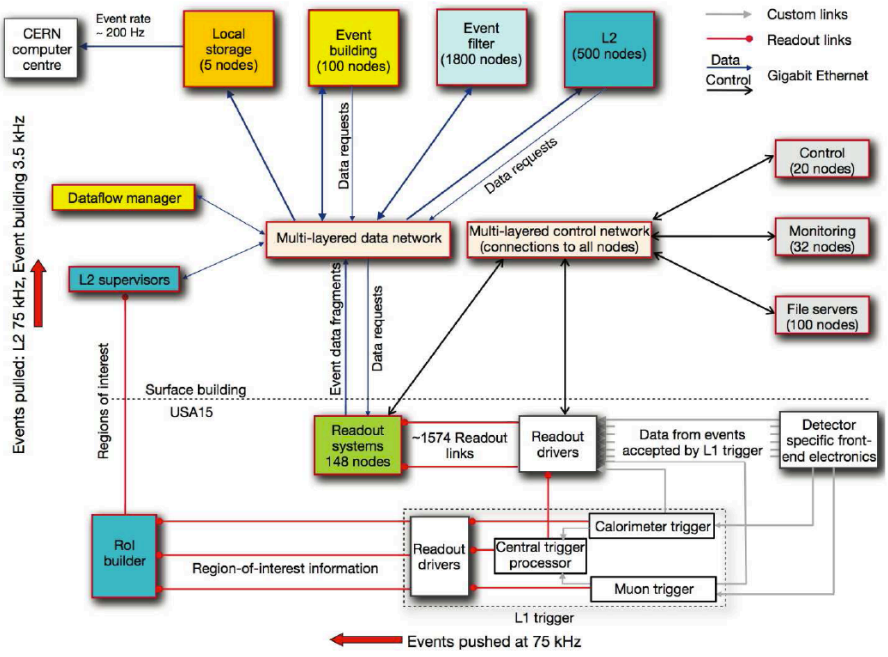

Figure 4.8: Overview of the ATLAS trigger and data acquisition

An important requirement of the DAQ is that data corresponding to one bunch crossing should be stored together as an *event*. This is complicated by the fact that light only travels about 7 meters in between two bunch crossings. Precise synchronization of all hardware is therefore essential. Figure 4.8 shows an overview of the trigger and DAQ system, which is implemented both in hardware and software. The detector front end electronics contains pipeline memories that can store data for several collisions while the first level trigger makes a decision. Decisions in the first level trigger are based on coarse grained data from the calorimeters and the muon system, reflecting the fact that interesting events may contain high energy jets, muons or electrons.

The general layout of the first level trigger (L1) is shown in Figure 4.9. Being required to deliver its decision in 2.5 μs the L1 trigger must be implemented in custom made hardware. The output rate from L1 is about 75 kHz, which can be tuned by varying for instance energy thresholds or introducing

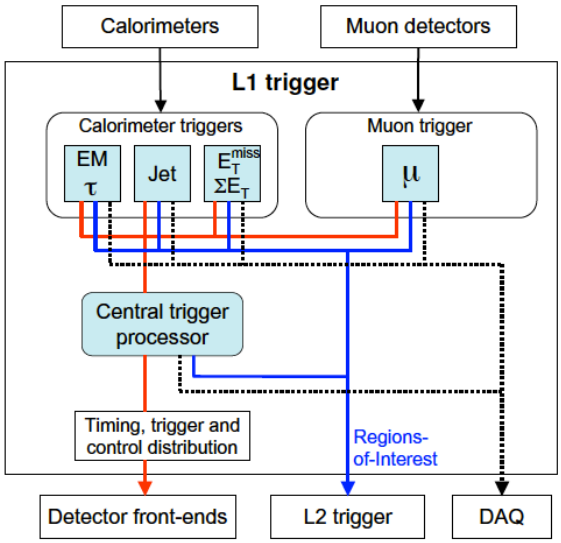

Figure 4.9: The first level trigger

prescales, i.e. picking only some fraction of the otherwise accepted events of a type. On a L1 trigger accept (or fire) data from all sub detectors are read out through detector specific read out drivers (ROD). The second level trigger (L2) will receive regions of interest (ROI) from L1, corresponding to regions in η-ϕ that might contain something interesting. Together with detailed data from the sub detectors the L2 trigger, implemented in software, makes its decision in about 40 ms and reduces the total rate to about 3.5 kHz.

An event accepted by the L2 trigger is processed by the event filter (EF) that can be thought of as the third level trigger. The EF runs a special version of the standard reconstruction software (ATHENA) and has access to all data from the event as well as details about the L1 and L2 decisions. Events accepted by the EF are stored for further offline processing into different streams depending on what features it has. The most important streams are "egamma" (electrons and photons), muons and jet/tau/$E_{\mathrm{T}}^{\mathrm{miss}}$. An event may end up in several streams.

4.7 Software

4.7.1 Reconstruction and simulation

Data processing and detector simulation [32] are both implemented in the ATHENA software framework. Events from real collisions and simulation are reconstructed by essentially the same software.

Simulated events are first *generated* at the level of a particular parton-parton process using an event generator, see section 2.7. The next step in the sim-

ulation chain is to propagate all generated particles through the detector and simulate their interactions with the detector material. The software framework GEANT4 [33, 34] is used in this step. This is followed by a simulation of the particular electronic signals produced by each detector front end. The result will be a raw event that is similar to a real measured event. Multiple pp interactions are added to every sample to simulate the effects of pile-up. Event generation and detector response simulation both deploy probabilistic algorithms of Monte Carlo type, i.e. with finite running time but with an uncertainty on the result. This is why simulated data is often referred to as Monte Carlo, or MC for short.

Raw events, either from simulation or collisions, are thereafter reconstructed in several steps. Hits in the inner detector are grouped into tracks, energy depositions in the calorimeters are grouped into clusters and muon tracks are formed from hits in the muons system. Information from several sub systems are then used to form high level objects such as electrons from ID tracks and EM clusters, jets from clusters in the calorimeters, and ID tracks and muons from ID and muon tracks. The first reconstruction step produces *event summary data* (ESD) files and *analysis object data* (AOD) files are produced in the subsequent step. The size of each event is reduced in every step. This size reduction procedure is referred to as *slimming*. An important part of the reconstruction is the application of different calibrations.

Data analysis could be performed on both ESD and AOD level, at least in principle, but in most cases the events contain much information that is unnecessary for a particular analysis. One also wishes to reduce the number of events by selecting only a subsets of the events based on triggers and properties of the event objects, which is referred to as *skimming*. There are several common slimming and skimming procedures that, when applied to AOD files, are called *derived physics data* (DPD) files. Both AOD and DPD files are object databases with a common event data model (EDM).

4.7.2 Analysis objects

One of the primary functions of the reconstruction software is to provide analysis level objects representing detected particles, including jets, electrons, muons, taus and photons. A very important quantity is the missing transverse energy, denoted $E_{\mathrm{T}}^{\mathrm{miss}}$, which ideally represent the momentum of undetected particles such as neutrinos or hypothetical particles that, like neutrinos, only interact weakly.

The details of the analysis object definitions are not centrally specified for the entire ATLAS, but rather optimized for a particular analysis. In practise, an expert *performance group* will define and maintain reconstruction algorithms for a number of baseline object definitions that can be customized by the analysers.

4.8 TileCal timing software

A piece of software for estimating timing calibration factors for the TileCal, was written by the author. The original procedure was developed by two colleagues at Stockholm University, Björn Nordkvist and Christophe Clément [35], and it was translated into software components for the ATLAS software framework ATHENA. Precise knowledge of the absolute and relative timing of different components in the detector front ends is important, electronic pulses generated by energy depositions in the calorimeter cells must be sampled as close to the peak value as possible to get the most accurate energy measurement. The procedure implemented uses a special calibration system that sends light pulses to the photo multiplier tubes in the TileCal front end electronics. Relative time differences between readout channels can then be estimated which in turn makes it possible to compute calibration coefficients that compensate for the time differences.

4.9 Analysis

The analysis starts with either AOD or DPD files that are transformed into ROOT NTuples by a special ATHENA package called SYNTMaker (Stockholm and Yale NTuple), which is developed and used by several universities. The SYNT NTuples are produced on the Grid and then transferred to local storage.

The analysis is performed locally on the SYNT NTuple files using a specially designed ROOT based framework called ATLANA.

Part III:

$t\bar{t}$ cross-section measurements

5 Introduction to $t\bar{t}$ production cross-section measurements

5.1 Overview

This thesis treats measurements of the $t\bar{t}$ production cross-section in the semi- and di-leptonic channels. The production mechanism for $t\bar{t}$ in proton-proton collisions was described in section 2.8. The branching fraction for the semi-leptonic channel, or $\ell+$jets for short, is 47.8% while it is 6.5% for the di-lepton channel, with a total branching fraction of 54.3% from $t\bar{t}$ to *at least* one lepton. The $\ell+$jets channel is further split in the sub-channels $e+$jets and $\mu+$jets, while the di-lepton channel consists of three sub-channels: ee, eμ and $\mu\mu$. These include the cases where a W decays to a τ that subsequently decays leptonically to e or μ.

This chapter introduces general properties of and techniques used in $t\bar{t}$ measurements in a final state with at least one lepton, including statistical methods (5.2), generic event selections (5.3), object definitions (5.4), background processes (5.5) and systematic uncertainties (5.6). The chosen lepton definitions below have been shown to be efficient at high jet multiplicities and mass scales, such as top pair production [31, 36]. The same definitions, with only small adjustments, apply to all top analyses presented in this thesis:

- The three measurements of the total $t\bar{t}$ cross-section in paper I for 2.9 pb^{-1}, paper III for 35 pb^{-1} and paper IV for 689 pb^{-1} that are summarised in chapter 7.
- The inclusive template measurement in paper II that is summarised in chapter 8.
- The measurement of the relative differential $t\bar{t}$ cross-section in paper V that is summarised in chapter 9.

5.2 Statistical methods

The cross-section is computed using the following expression:

$$\sigma = \frac{N^{data} - N^{bg}}{A\mathscr{L}} \tag{5.1}$$

where A is the effective acceptance, $\mathscr{L}$ is the integrated luminosity, N^{data} is the number of measured events in data and N^{bg} is the number of estimated background events. A has to be be estimated from simulations and it is given

by the number of events passing the event selection, divided by the total number of simulated events. All efficiencies and scale factors as well as branching ratios are included in A; hence the term effective acceptance. For brevity, the term acceptance will be used from this point instead of affective acceptance, but it should not be confused with with the purely kinematic acceptance.

Systematic uncertainties affect both the background estimate N^{bg} and the acceptance A. Two different methods for computing the cross-section and evaluating the impact of uncertainties are used for the analyses in this thesis: direct computation of e.q. (5.1) together with pseudo experiments, and a maximum likelihood (ML) [37] method with profiling, sometimes combined with pseudo experiments.

In both approaches the impact of systematic uncertainties on the quantities in eq. (5.1) are estimated for plus and minus one standard deviation. Take acceptance A as an example; A^0 denotes the baseline value and $A^{(+)k}$ ($A^{(-)k}$) denotes the value of the acceptance when uncertainty k is evaluated at plus (minus) one standard deviation. The shifts in the quantity are:

$$\Delta A^{(+)k} = A^{(+)k} - A^0 \qquad \Delta A^{(-)k} = A^0 - A^{(-)k}$$

A parameter d_k is assigned to systematic uncertainty k and the set of them ($\vec{d}$) is used as a parameter in a linear expansion of the quantity in question:

$$A(\vec{d}) = A^0 + \sum_k d_k \left\{ \theta(d_k)\Delta A^{(+)k} + \theta(-d_k)\Delta A^{(-)k} \right\}$$

where θ is the Heaviside step function.

Each uncertainty is modelled by some distribution, usually a Gamma distributions for asymmetric uncertainties or a Gaussian distribution ($\mathcal{G}$) for symmetric uncertainties. The integrated luminosity uncertainty ($\delta\mathscr{L}$) is modelled by a Gaussian in all analyses in this thesis.

For direct evaluation of the cross-section with pseudo experiments, like in the measurement of the relative differential cross-section in chapter 9, the d_k:s are pulled from their respective distributions, either all at once to evaluate the total uncertainty, or one at a time to estimate the impact of a single uncertainty. The statistical uncertainty is modelled by a Poisson distribution of the observed number of events. The cross-section is then evaluated enough times to make the statistical uncertainty from the method negligible:

$$\sigma(\vec{d}) = \frac{Po(N^{data}) - N^{bg}(\vec{d})}{A(\vec{d})\mathscr{L}(\vec{d})}$$

The impact of a single uncertainty is estimated by evaluating the cross-section and its uncertainty with statistical uncertainty alone ($\delta\sigma_{stat}$), then evaluating with statistical and one other uncertainty enabled ($\delta\sigma^k_{stat}$). The impact for systematic uncertainty k is then:

$$\delta\sigma^k = \sqrt{(\delta\sigma^k_{stat})^2 - (\delta\sigma_{stat})^2}$$

In ML estimates of the cross-section, used is the analyses in chapters 7 and 8, uncertainties can be incorporated by both profiled nuisance parameters and pseudo experiments. Each profiled uncertainty k has an associated nuisance parameter (α_k), normalized such that $\alpha_k = 0$ is the baseline and $\alpha_k = \pm 1$ corresponds to a shift $\pm 1\sigma$ of the uncertainty. A constraint factor is included in the likelihood for each nuisance parameter. To construct the likelihood, the cross-section formula eq. (5.1) is rewritten as:

$$N^{exp}(\sigma, \mathscr{L}, \vec{\alpha}) = \mathscr{L}(\vec{\alpha})A(\vec{\alpha})\sigma + N^{bg}(\vec{\alpha})$$

where $\vec{\alpha}$ denotes the set of nuisance parameters and N^{bg} is the sum of the background contributions. The expected number of events N^{exp} is modelled by a Poisson, and the likelihood function can be written:

$$\mathcal{L}(\sigma, \mathscr{L}, \vec{\alpha}) = Po(N^{obs}|N^{exp}(\sigma, \mathscr{L}, \vec{\alpha}))\mathcal{G}(\mathscr{L}|\mathscr{L}_0, \delta\mathscr{L})\prod_k f_k(\vec{\alpha}) \qquad (5.2)$$

where f_k is the distribution for uncertainty k and $\mathscr{L}_0$ is the measured integrated luminosity. A profile likelihood ratio [12] is then constructed:

$$\lambda(\sigma) = \frac{\mathcal{L}(\sigma, \hat{\hat{\mathscr{L}}}, \hat{\hat{\vec{\alpha}}})}{\mathcal{L}(\hat{\sigma}, \hat{\mathscr{L}}, \hat{\vec{\alpha}})}$$

from which the cross-section, its total uncertainty and the contribution from a single uncertainty, can be evaluated. Quantities with a single circumflex represents maximum likelihood estimates, while the quantities with double circumflexes are conditional maximum likelihood estimates with respect to a fixed σ. The statistical uncertainty is estimated by profiling a likelihood ratio:

$$r(\sigma) = \frac{\mathcal{L}(\sigma, \hat{\mathscr{L}}, \hat{\hat{\vec{\alpha}}})}{\mathcal{L}(\hat{\sigma}, \hat{\mathscr{L}}, \hat{\hat{\vec{\alpha}}})}$$

which means that the purely systematic uncertainty term can be computed as the difference between the total ($\delta\sigma_{total}$) and the statistical only uncertainties ($\delta\sigma_{stat}$) in quadrature, i.e.:

$$\delta\sigma_{syst} = \sqrt{(\delta\sigma_{total})^2 - (\delta\sigma_{stat})^2}$$

The same expression is used to get the impact of a single systematic uncertainty, $\delta\sigma_{stat}$ is replaced by the uncertainty from the profile likelihood ratio when one systematic is disabled.

5.3 Event selections

$t\bar{t}$ events are characterized by high jet multiplicity and a large amount of missing transverse momentum ($E_{\mathrm{T}}^{\mathrm{miss}}$) due to the escaping neutrinos. High p_{T} leptons are also expected and they are required to be *isolated*, i.e. the energy sum

in a cone around the lepton is required to be below some threshold. This requirement reflect the fact that signal leptons, defined below, originate from the leptonic decay of W or Z bosons. In effect, the cut reduce the background contamination from non-signal leptons. In the case of $\ell+$jets, at least 4 jets are required, which means that ideally all the jets from the $t\bar{t}$ decay are reconstructed, c.f. Figure 2.6(b). There is a chance that jets escape the detector acceptance. Furthermore, jets from initial of final state radiation could be reconstructed instead, which would bring the total jet multiplicity back up to 4, or above. Two jets are required in the di-lepton channel, in addition to two leptons of opposite charge, c.f. Figure 2.6(a).

For di-lepton events in the ee and $\mu\mu$ channels, the Drell-Yan background is reduced by imposing two cuts on the invariant mass of the lepton pair (m_{ll}). By demanding that the invariant mass is above some level (typically 15 GeV in the later analyses) the low mass Drell-Yan and the non-signal lepton backgrounds are reduced. The contribution from $Z+$jets at the Z pole mass is reduced by demanding that $|m_{ll}-91| > 10$ GeV. Since the ATLAS trigger is fully simulated, all events are required to have a global lepton trigger fire, in both data and MC, as well as having match between the EF trigger objects and the analysis leptons.

All objects are reconstructed with respect to a primary vertex, which is required to have at least 5 tracks. Each of the tracks should have a significant amount of p_{T}, typically at least 1 GeV.

Two of the jets in $t\bar{t}$ events originate from b-quarks. There are several ways to *tag* such jets using the fact that b-hadrons have large masses, relatively long lifetimes and often decay to unisolated leptons. Such b-tagging procedures are used in some of the analyses to purify the signal region.

5.4 Object definitions

5.4.1 Electrons

The base of an electron object is a LAr energy cluster matched in η and ϕ to an inner detector track [31]. There is a gap in the LAr calorimeter between the barrel and the extended barrels $1.37 < |\eta| < 1.57$ that is excluded. Electrons are then classified according to their *tightness*: A tighter electron definition means a higher jet rejection [38], i.e. higher purity, but lower efficiency. A “loose" electron has requirements on the shower shape variables of the second layer in the calorimeter and on the hadronic leakage. A “medium" electron satisfy the loose electron requirements as well as additional requirements on the shower shape variables in the first calorimeter layer and track quality. A “tight" electron has additional requirements on: the E/p ratio (E is the calorimeter energy and p is the track momentum), pixel b-layer hits and the number of TRT hits.

Analysis electrons must satisfy the “tight" requirements and have a p_{T} above 20 GeV in the early analyses and above 25 GeV in the later analyses. Also, the isolation energy sum within a cone $\Delta R < 0.2$ of the electron is required to be less than some analysis dependent upper threshold. This energy sum is corrected for hadronic leakage and pile-up effects.

The energy scale of electrons in data is calibrated to the Z peak, and the energy resolution in MC is adjusted by smearing the energy to match the measured resolution of the detector. Scale factors are applied to MC to adjust for differences in identification-, reconstruction and trigger efficiencies. The scale factors are computed from data and MC efficiencies (ε) estimated in $Z \rightarrow ee$ events: $SF = \varepsilon^{data}/\varepsilon^{MC}$.

5.4.2 Jets

Jets are reconstructed starting from topological clusters of energy depositions in the calorimeters, using the anti-k_t algorithm [39, 40, 41] with a radius of $\Delta R = 0.4$. The cluster energy is calibrated to the electromagnetic (EM) energy scale, i.e. the energy scale for electrons and photons. The energy of the entire jet is then adjusted to the hadronic scale using calibration factors derived from MC, and the jet is said to be calibrated to EM+JES (Jet Energy Scale) [42, 31].

The coordinates of the jet (in η and ϕ) are defined relative to the primary vertex. The original detector coordinates, relative to the centre of ATLAS, are kept and used to avoid overlap with electrons and muons. The jet p_{T} is required to be above 20 GeV for the early analysis and 25 GeV for the later and $|\eta| < 2.5$. Jets within $\Delta R < 0.2$ of an electron are removed. Only one jet, the closest, per electron is removed this way.

5.4.3 Muons

Muon objects are reconstructed with the MuID algorithm [36], using information from the inner detector, calorimeters and the muon spectrometer. A track in the MS is constructed starting with track segments in the outer layer and then proceeding inwards, matching to further track segments. The MS muon track is then matched to an inner detector track. The measured energy losses in the calorimeter are taken into account when matching the momentum of the inner (ID) and outer (MS) tracks. The final tight muons are reconstructed by performing a global refit of both tracks. Analysis muons must have $p_{\mathrm{T}} > 20$ GeV, $|\eta| < 2.5$ and there are requirements on the inner detector track quality, including a minimum amount of hits together with checks on the number of dead sensors the track passes through. There are also requirements on the maximum amount of calorimeter isolation in a cone with $\Delta R < 0.3$, and on track isolation in a cone $\Delta R < 0.3$. For both track and calorimeter isolation, the contribution from the muon itself is removed. A muon that lie within $\Delta R < 0.4$ of an analysis jet is removed.

Differences in detector modelling with respect to reconstruction, identification and trigger are corrected for by applying scale factors to MC. The muon momentum is smeared in MC to match the detector resolution, measured in $Z \to \mu\mu$ events.

5.4.4 Missing transverse energy - $E_{\mathrm{T}}^{\mathrm{miss}}$

The $E_{\mathrm{T}}^{\mathrm{miss}}$ is the negative transverse vector sum of all energy depositions in the detector. It includes contributions from all objects according to the object definitions given above. Contributions from all calorimeter cells with energy above the noise level are added, the fraction of energy associated with a specific type of analysis object (jet, electron, tau, muon or photon) is calibrated to the appropriate energy scale. The following terms are included in the $E_{\mathrm{T}}^{\mathrm{miss}}$ [43]:

- $\vec{E}_T^{ele}$: Tight electrons, calibrated to the EM scale.
- $\vec{E}_T^{\gamma}$: Tight photons, calibrated to the EM scale.
- $\vec{E}_T^{\tau}$: Tight taus calibrated to the EM scale.
- $\vec{E}_T^{jet}$: AntiKt4 jets with $p_{\mathrm{T}} > 20$ GeV with energy calibrated to EM+JES scale.
- $\vec{E}_T^{SoftJet}$: AntiKt4 jets with $7 < p_{\mathrm{T}} < 20$ GeV, calibrated to the EM scale.
- $\vec{E}_T^{\mu}$: Tight muons with distance to jet $\Delta R > 0.4$.
- $\vec{E}_T^{CellOut}$: All energy not associated to an object, could be cells completely disconnected from or partially connected to an object. This contribution is calibrated to the EM scale.

The final result is:

$$\vec{E}_T^{\mathrm{miss}} = -(\vec{E}_T^{ele} + \vec{E}_T^{\gamma} + \vec{E}_T^{\tau} + \vec{E}_T^{jet} + \vec{E}_T^{SoftJet} + \vec{E}_T^{\mu} + \vec{E}_T^{CellOut}) \tag{5.3}$$

The absolute value of this vector, $E_{\mathrm{T}}^{\mathrm{miss}} = |\vec{E}_T^{\mathrm{miss}}|$, is a commonly used quantity.

5.5 Backgrounds

Several processes in the Standard Model have significant cross-sections in the $t\bar{t}$ region, and many of them also have at least one signal lepton in their final state. Before proceeding with specifying these processes, a formal definition of “signal lepton" is required.

Definition 5.5.1 (Signal lepton) *A signal lepton is an electron or a muon from the leptonic decay of a W− or Z boson that is produced in a hard scattering, c.f. section 2.7. Leptonic boson decays through taus to electrons or muons are included.*

There is also a class of events with leptons that are *not* signal leptons and they are introduced in section 5.5.1.

The following processes contain at least one signal lepton in the final state:

- Production of a single top with leptonic decay: Section 5.5.2.
- Di-boson production, WW, WZ or ZZ with leptonic decays: Section 5.5.3.
- Production of a single W and subsequent leptonic decay: Section 5.5.4.
- The Drell-Yan process, i.e. the production of a Z/γ^* and the subsequent decay into two same flavor leptons: Section 5.5.5.

5.5.1 Non-signal leptons

The concept of signal leptons is an idealization; the detector and reconstruction software produces *reconstructed leptons*. Due to detector and software imperfections, not all signal leptons, that otherwise satisfy lepton criteria such as momentum, η and ϕ cuts, will end up as reconstructed leptons. The probability that a signal lepton will be reconstructed is referred to as the *reconstruction efficiency*, which is highly dependent on the lepton definition used in the analysis.

The set of all reconstructed leptons is made up of two disjoint subsets; reconstructed signal leptons and *fake* leptons, sometimes referred to as non-signal leptons. A fake lepton is an object reconstructed as a lepton, electron or muon, but not produced according to definition 5.5.1. An event containing at least one fake lepton is called a fake event. The probability for a non-signal lepton to be reconstructed as a lepton is called *intrinsic fake rate*.

Because the detector and reconstruction software are designed to distinguish between signal and fake leptons, the rejection of fake leptons is very high. This implies that a very large number of events have to be simulated to produce a statistically significant result. Furthermore, the origin of the fake leptons is uncertain, i.e. what processes that do contribute and their intrinsic fake rates for the produced non-signal leptons.

In electro-weak (EWK) processes the dominating source of fake leptons is photon conversions. Photons can produce a lepton pair early in the detector, which means that there are both tracks and an electro-magnetic cluster. In some cases this is reconstructed as a single electron.

For QCD processes, jets are responsible for inducing fake leptons. Top quark pair production is a special case because the top quark itself has such a short lifetime and decays to W and a b-quark, with 100% probability, before it can hadronize to a jet. Real leptons can be created inside jets, but they are not signal leptons because they are not isolated.

A data driven method is needed because of the mentioned difficulties with simulating the fake lepton background. Such a method will be presented in chapter 6.

5.5.2 Single top production

Of the four single top production processes shown in Figure 5.1, only the Wt channel is a signal process in the di-lepton final state. All processes may

contribute to fake di-lepton events and to the EWK background in $\ell+$jets. The processes where the W decays hadronically gives a tiny contribution to the fake lepton background in the $\ell+$jets. The computed cross-section for the t-channel is $64.57^{+2.71}_{-2.01}$ pb [44], the s-channel cross-section is $4.63^{+0.19}_{-0.17}$ pb [45] and the Wt channel cross-section is $15.74^{+1.06}_{-1.08}$ pb [46]; all three cross-sections are computed at NNLL precision.

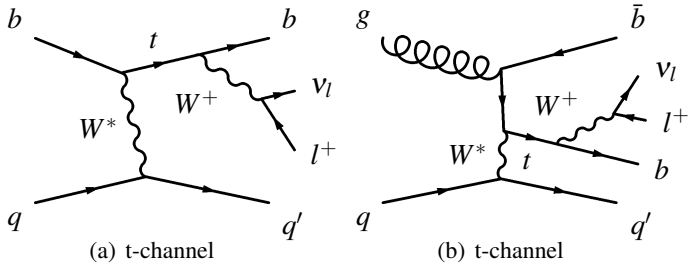

Figure 5.1: Single top production with leptonic W decays.

5.5.3 Di-boson production

There are three different di-boson processes that contribute signal leptons, both in the $\ell+$jets and di-lepton final states: WZ shown in Figure 5.2, WW and ZZ shown in Figure 5.3. The decay products of the bosons are not shown, but the possible final states are: fully hadronic, semi-leptonic, di-leptonic, tri-leptonic and quad-leptonic in case of ZZ. Leptonic decays of W bosons will result in neutrinos that contribute to $E_{\mathrm{T}}^{\mathrm{miss}}$. The cross-sections for the processes were computed at NLO by MCFM to: $\sigma(WW) = 44.9 \pm 2.2$ pb, $\sigma(WZ) = 18.5 \pm 1.3$ pb and $\sigma(ZZ) = 9.53 \pm 0.46$ pb, when both Z masses are assumed to be above 12 GeV.

5.5.4 W+jets production

Figure 5.4(a) shows an example of single W boson production together with a gluon jet and the subsequent leptonic decay of the boson. The neutrino will contribute to the $E_{\mathrm{T}}^{\mathrm{miss}}$. In the di-lepton final state this process is one of the

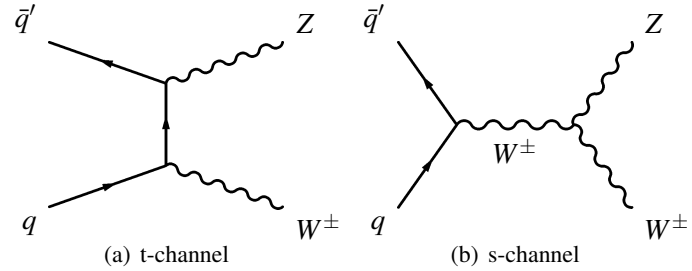

(a) t-channel (b) s-channel

Figure 5.2: WZ production.

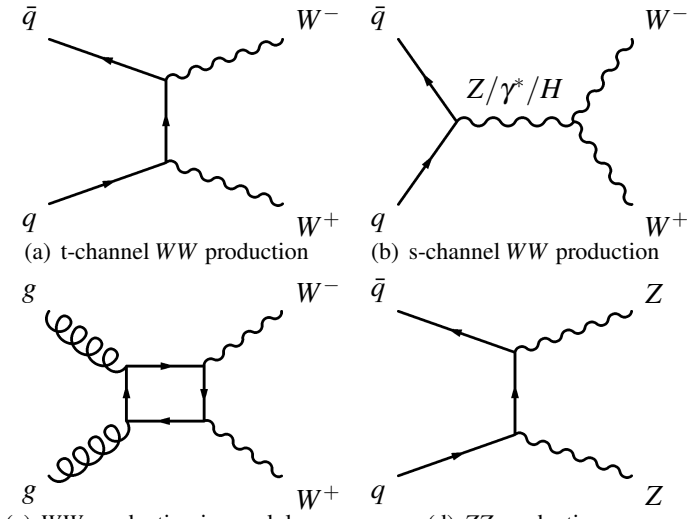

(a) t-channel WW production (b) s-channel WW production

(c) WW production in quark loop (d) ZZ production

Figure 5.3: WW and ZZ production.

larger sources of fake lepton events, when the jet is miss-reconstructed as a lepton. The cross-section $\sigma(W^{\pm} \to l\nu) = 10.46 \pm 0.52$ nb was computed at NNLO precision by the FEWZ tool [47][73]. Because LHC collides protons, the cross-section for W^+ is larger than that for W^-, $\sigma(W^+ \to l^+\nu) = 6.16 \pm 0.31$ nb and $\sigma(W^- \to l^-\nu) = 4.30 \pm 0.21$ nb.

5.5.5 Drell-Yan+jets

Examples of the Drell-Yan process are shown in Figures 5.4(b) and 5.4(c). A Z boson or a virtual photon (γ^*) is produced together with zero (b) or one (c) jet created by an ISR gluon, c.f. section 2.7. Close to zero intrinsic $E_{\mathrm{T}}^{\mathrm{miss}}$ is generated in this process when Z/γ^* decays to ee or $\mu\mu$.

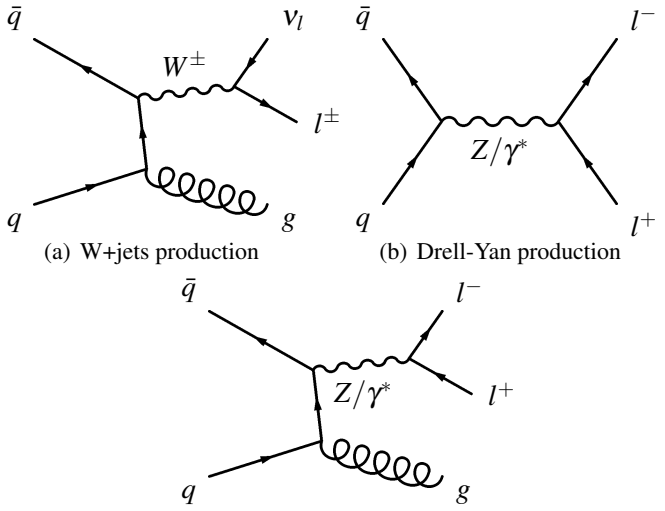

(a) W+jets production

(b) Drell-Yan production

(c) Drell-Yan production with one ISR gluon jet

Figure 5.4: W+jets and Drell-Yan production with leptonic decays.

The invariant mass spectrum in the di-lepton final state has a narrow peak around the Z boson mass (91 GeV). This process is in itself well understood and it is a good source of signal leptons that can be used for energy calibrations and efficiency studies of both leptons and jets. The cross-section at NNLO precision is $\sigma(Z/\gamma^* \to ll) = 1.07 \pm 0.054$ nb [47][73].

5.6 Systematic uncertainties

There are two main categories of systematic uncertainties: detector modelling uncertainties and signal or background modelling uncertainties. The former contains the following sources of uncertainty:

- The energy scale (LES) and energy resolution (LER) of the lepton. Uncertainty on the efficiency for triggering, identifying and reconstructing.
- Jet energy scale (JES) and energy resolution (JER). Jet reconstruction efficiency (JEE) and b-tagging uncertainties.
- Variations in energy scales of objects in the event is propagated to the $E_{\mathrm{T}}^{\mathrm{miss}}$, but the uncertainty on the energy of the cells not associated to any jet or soft jet, the SoftJet and CellOut terms in eq. (5.3), has to be estimated (MET).
- The luminosity uncertainty is often reported as a separate uncertainty in measured cross-sections, but kept in the detector section for completeness.

- Other detector imperfections not properly modelled in the default simulation may require additional uncertainties.

The signal and background modelling uncertainties are:

- Comparison between different event generators for the $t\bar{t}$ signal (GEN).
- Difference between parton shower models for the $t\bar{t}$ signal (PS).
- Initial (ISR) and final (FSR) state radiation modelling. Estimated by adjusting the scale for the computation of α_s and PDF value, in case of ISR, in the parton shower model. For ISR the maximum allowed parton virtuality is also adjusted. These shifts are only evaluated for the $t\bar{t}$ signal.
- The experimental and theoretical uncertainty for parton distribution functions (PDF).
- Normalization and shape of dominant backgrounds such as fake leptons, $W+$jets and $Z+$jets.

The actual implementation, magnitude and final impact of these uncertainties vary between the different analyses. All uncertainties are evaluated by changing the model; data is not shifted, only calibrated to a baseline.

6 Estimation of the non signal lepton background to $t\bar{t}$

6.1 Overview

This chapter deals with the $t\bar{t}$ background due to non signal leptons, i.e. objects not produced according to the definition 5.5.1. To estimate the number of fake lepton events in the signal region[1], a data driven method is required. The QCD processes giving rise to fake leptons are probably not modelled well enough by the simulation, nor is the reconstruction efficiency for such objects expected to be accurately described by simulations. A high jet rejection for the tight analysis lepton also makes simulation of the background very inefficient especially for di-lepton double fake leptons. The jet rejection is expected to be at least 50000 for electrons [48]. A data driven method for determining the fake lepton background, known as the *matrix method*, is introduced in section 6.3. This is not a single method, but rather an approach that leads to different solutions depending on the assumptions being made. Two different, and complementary, solutions will be presented and compared.

The main part of the results presented in this chapter was obtained from the 35 pb^{-1} of data taken during 2010 used for paper III and the 689 pb^{-1} of data taken during 2011 used for paper paper IV. Some results are also shown for the earliest analysis of the 2.9 pb^{-1} of data used for paper I. More details, particularly control region plots, can be found in reference [8].

6.2 Origins of fake leptons

The primary origins of fake leptons are: photon conversions, light flavour jets and heavy flavour jets.

For muons, the number of fake leptons from photon conversions is expected to be very small. Fake electrons from conversions are produced when a photon interacts with detector material and splits into an electron-positron pair; when this happens in the inner detector, a track can be left which, combined with the EM cluster from the electron and positron, may be reconstructed as an electron. The majority of conversion fake leptons are removed by a requirement of a hit in the very first layer of the tracker, but random calorimeter clusters can still be combined with conversion tracks to form fake electrons.

[1] The signal regions used in the final analysis are defined in section 5.3.

Jets are produced in a number of different ways, such as in hard QCD processes, from ISR/FSR[2] in electro-weak processes or in the hadronic decay of gauge bosons. A typical jet consists of a number of hadrons, some of them charged that leave tracks in the ID. If the jet is reconstructed with a large fraction of EM energy and there is a random track that matches the calorimeter cluster, this could be interpreted as an electron. Pions are commonly produced in jets and they might decay to photons, leaving a high EM energy fraction. Leptons produced inside a jet in EWK processes, eg. leptonic decay of a b-hadron, is another source. Many fake electrons and a majority of the fake muons are expected to be produced this way.

In the di-lepton final state, the largest fake lepton contribution in the high $E_{\mathrm{T}}^{\mathrm{miss}}$ region is expected from W+jets where the W decays leptonically and the jets may result in fake leptons, c.f. Figure 5.4(a). In the low $E_{\mathrm{T}}^{\mathrm{miss}}$ regions $b\bar{b}$ production gives a large contribution and this process result in two heavy flavour jets with expected higher probability to generate fake leptons. Another big source is $t\bar{t}$ itself, where one of the top quarks decays hadronically, i.e. the W decays to a quark pair, c.f. Figure 2.6(b). QCD processes such as quark pair production are expected to give the largest fake lepton contribution in the $\ell+$jets final state.

6.3 Method overview

6.3.1 Lepton definitions

The first step in the fake lepton estimation procedure is to define a *loose lepton*. The loose lepton is, as suggested by the name, an object with a looser definition than that of the analysis lepton, defined in section 5.4. In the context of fake leptons, the analysis lepton is often referred to as a *tight lepton*[3]. Definitions of the loose electrons and muons used in the following analyses are given in section 6.4. There are two different loose lepton definitions for both muons and electrons. The reason for this is that the two different variants of the matrix method uses different loose lepton definitions. The first variant is called the *low rate* matrix method (lMM), and the corresponding loose leptons are much looser than those of the other variant, called the *high rate* matrix method (hMM). An important point is that the same tight lepton, defined by the analysis, is used in both methods.

6.3.2 Fake rate and real efficiency measurements

The next step in the procedure is to measure a *fake rate* (f) and a *real efficiency* (r) for the loose lepton definitions, with $r > f$ required. In the following equa-

[2] see section 2.7

[3] The label *tight lepton* should not be confused with a lepton fulfilling the “tight" quality requirement which is also called a tight lepton in some cases, c.f. section 5.4.

tions T refers to a reconstructed tight lepton, L refers to a reconstructed loose lepton that *fails* the tight requirements while l denotes a lepton that is reconstructed as loose but may also satisfy the tight lepton requirements. R refers to a signal (real) lepton while F refers to a fake lepton.

The fake rate is the probability for a loose fake lepton to be reconstructed as a tight lepton:

$$f = \frac{N_F^T}{N_F^l} \tag{6.1}$$

This ratio is measured in a control sample, dominated by fake leptons, that contains N_F^l loose leptons out of which N_F^T also satisfy the tight lepton definition. One can choose the loose lepton to be close to the tight lepton which gives a high fake rate. The other alternative is to choose very loose lepton definition which gives a low fake rate.

The real efficiency is the probability for a loose signal lepton to be reconstructed as a tight lepton:

$$r = \frac{N_R^T}{N_R^l} \tag{6.2}$$

This ratio is measured in a control sample dominated by signal leptons, that contains N_R^l loose leptons out of which N_R^T also satisfy the tight lepton definition.

6.3.3 Fake lepton matrix

In the matrix method, the number of real loose (N_R^l) and fake loose (N_F^l) events are related to the observed number of tight (N_T) and loose (N_L) events by a matrix built from the real efficiency and fake rate. The single lepton matrix equation is written as:

$$\begin{pmatrix} N_T \\ N_L \end{pmatrix} = \begin{pmatrix} r & f \\ 1-r & 1-f \end{pmatrix} \begin{pmatrix} N_R^l \\ N_F^l \end{pmatrix} \tag{6.3}$$

The inverse of this matrix gives the relation between the number of real and fake lepton events, given the observed number of tight and loose lepton events:

$$\begin{pmatrix} N_R^l \\ N_F^l \end{pmatrix} = \frac{1}{r-f} \begin{pmatrix} 1-f & -f \\ r-1 & r \end{pmatrix} \begin{pmatrix} N_T \\ N_L \end{pmatrix} \tag{6.4}$$

The superscripts l in the equations above indicate that the number of fake lepton events is given in the loose basis, i.e. N_F^l is the number of fake events in the inclusive sample of loose leptons. To move from the loose sample to the tight sample, a factor f is needed. Thus, the number of fake lepton events in the tight sample can be written:

$$N_F^T = \frac{fr}{r-f} N_L + \frac{f(r-1)}{r-f} N_T \tag{6.5}$$

By definition $r < 1$, and since $r > f$ is required, the second term will be strictly negative. This term is interpreted as a correction for the contamination of real leptons that fail the tight lepton acceptance and end up in the exclusive loose sample.

6.3.4 Extrapolation to the signal region

The rate for the three (two) different origins of fake electrons (muons) may be different for the chosen lepton definitions. In order to investigate and quantify this, the fake rate is measured in three (two) sub samples that are enriched in the different origins of fake leptons. Furthermore, the compositions of both the loose control sample and the loose signal sample are unknown, i.e. the fractions of fake loose leptons from conversions, heavy flavour and light flavour. The MC truth information is used to estimate these fractions both in the signal and the control samples. The flavour fractions are then used to extrapolate the rate from the control region where it is measured, to the signal region where the fake lepton yield is estimated.

6.3.5 Signal region fake lepton yield

To estimate the yield in the di-lepton final state, a sample with one tight lepton and one loose lepton is used in the low rate matrix method. A sample with two loose leptons is used for the high rate. The reason for using only one loose lepton in the low rate method is because the loose lepton is too loose to match the lepton trigger requirements. In the $\ell +$ jets final state, a sample with one loose lepton is selected.

Each event in the loose signal sample is then weighted according to the elements of the inverted fake lepton matrix. For $\ell +$ jets, the weights from eq. (6.5) are used.

Systematic uncertainties of the fake lepton yield then has to be estimated. Kinematic and sample compositions differences between the control sample and the loose lepton signal sample are expected to be the dominating sources of systematic uncertainties.

Summary

Figure 6.1 shows a diagram summarizing all the steps in the fake lepton yield estimation procedure. Details of all the steps will be given in the following sections. The diagram should be read from left to right:

- The control samples are used to determine raw fake rates (f_l for the low rate, f_h for the high rate) and real efficiencies (r_l and r_h).
- The raw fake rates are extrapolated to the loose signal region using information about sample composition from simulation.

- A matrix with the extrapolated rate (hM_1 for single lepton high rate, hM_2 for di-lepton high rate and lM_2 for low rate di-lepton) will then be applied to the loose signal samples to give a fake lepton yield (Nf_1 the number of single fake lepton events and Nf_2 is the number of di-lepton fake events).
- The yield will be validated in various distributions, like transverse mass M_T (or w_T) and $E_{\mathrm{T}}^{\mathrm{miss}}$, in control regions with either one or two leptons.

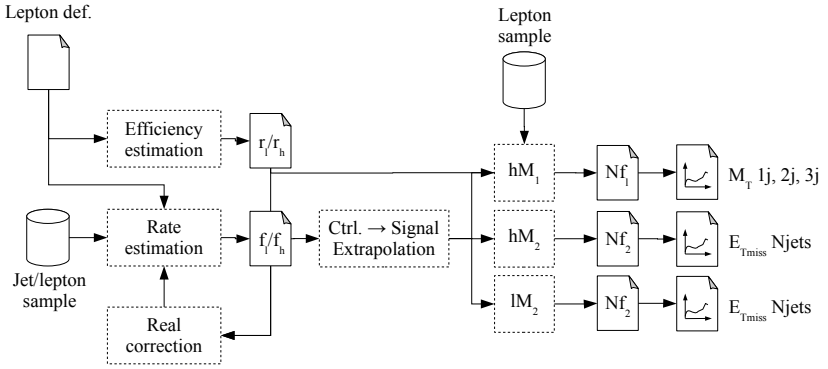

Figure 6.1: Overview of the fake lepton estimation procedure, should be read from left to right. Cylinders represent input data, measured or simulated. Boxes with dotted borders represent computations and initial, intermediate or final information is represented by file symbols.

6.4 Loose object definitions

6.4.1 Low rate loose lepton definitions

A low rate loose electron is an electro-magnetic cluster with a track, satisfying quality requirements "loose", which means cuts on the shower shape and the hadronic leakage variables [38]. An inner detector track, with charge compatible with +1e or -1e must be matched to the cluster. For 35 pb^{-1}, the object cuts are similar to those of the tight analysis lepton, defined in section 5.4.1, except that the cut on the corrected calorimeter isolation in a cone $\Delta R \leq 0.2$ has been loosened and is required to be less than $6 + 0.3 p_{\mathrm{T}}$ GeV. For 2.9 pb^{-1} the calorimeter isolation, with the same cone size, is required to be less than $4 + 0.023 p_{\mathrm{T}}$ GeV.

A low rate loose muon is an isolated track. For 35 pb^{-1} the cut on the track are similar to those applied to the tight analysis muons 5.4.3, except for loosened isolation cuts; track isolation in a cone $\Delta R \leq 0.3$ is required to be less than 10 GeV and calorimeter isolation in a cone $\Delta R \leq 0.3$ must be less than 10 GeV. For 2.9 pb^{-1} the calorimeter isolation in a cone $\Delta R \leq 0.2$ is required

to be less than $0.1 p_{\mathrm{T}}$ GeV and the track is required to have 3 SCT hits as well as 2 hits in the pixel detector.

6.4.2 High rate loose lepton definitions

High rate loose electrons satisfy the "medium" quality requirements for an electron. The cuts on the loose electron are similar to the ones for the tight analysis electron, defined in section 5.4.1, except for loosened calorimeter isolation. The isolation in a cone $\Delta R \leq 0.2$ is required to be less than $6 + 0.3 p_{\mathrm{T}}$ GeV in the 35 pb^{-1} analyses, and less than 6 GeV in the 689 pb^{-1} analysis. Compared to the tight electron, the requirements on track matching is looser, there is no conversion check and there are no TRT hit requirements.

The only difference between the tight analysis muon and the high rate loose muon is the absence of isolation cuts on the latter.

6.5 The di-lepton matrix

To estimate the contribution from fake leptons in the tight signal sample one starts with the fake rate f, defined in eq. (6.1), and the real efficiency r, defined in eq. (6.2).

There are four disjoint subsets in the di-lepton loose signal sample, if the leptons are ordered in p_{T}: N_{TT}, N_{TL}, N_{LT} and N_{LL}. Now construct a matrix that relates these numbers to the "true" contents of the sample : N^{ll}_{RR} events with two signal leptons, N^{ll}_{RF} (N^{ll}_{FR}) events where the first (second) lepton is a signal lepton and the other a fake lepton and N^{ll}_{FF} where both leptons are fake:

$$\mathbf{M} = \begin{bmatrix} r_1 r_2 & r_1 f_2 & f_1 r_2 & f_1 f_2 \\ r_1(1-r_2) & r_1(1-f_2) & f_1(1-r_2) & f_1(1-f_2) \\ (1-r_1) r_2 & (1-r_1) f_2 & (1-f_1) r_2 & (1-f_1) f_2 \\ (1-r_1)(1-r_2) & (1-r_1)(1-f_2) & (1-f_1)(1-r_2) & (1-f_1)(1-f_2) \end{bmatrix} \tag{6.6}$$

where the index on r and f refers to the first (1) or second (2) lepton in the event, where the leptons are ordered by p_{T}. There is an analytical expression for the inverse of $\mathbf{M}$:

$$\mathbf{M}^{-1} = \frac{1}{(r_1 - f_1)(r_2 - f_2)} \begin{bmatrix} (1-f_1)(1-f_2) & (f_1-1) f_2 & f_1(f_2-1) & f_1 f_2 \\ (f_1-1)(1-r_2) & (1-f_1) r_2 & f_1(1-r_2) & -f_1 r_2 \\ (r_1-1)(1-f_2) & (1-r_1) f_2 & r_1(1-f_2) & -r_1 f_2 \\ (1-r_1)(1-r_2) & (r_1-1) r_2 & r_1(r_2-1) & r_1 r_2 \end{bmatrix} \tag{6.7}$$

The equation for the sample becomes:

$$\begin{bmatrix} N_{TT} \\ N_{TL} \\ N_{LT} \\ N_{LL} \end{bmatrix} = \mathbf{M} \begin{bmatrix} N_{RR}^{ll} \\ N_{RF}^{ll} \\ N_{FR}^{ll} \\ N_{FF}^{ll} \end{bmatrix} \tag{6.8}$$

which can be solved for the expected number of fake di-lepton events:

$$\begin{bmatrix} N_{RR}^{ll} \\ N_{RF}^{ll} \\ N_{FR}^{ll} \\ N_{FF}^{ll} \end{bmatrix} = \mathbf{M}^{-1} \begin{bmatrix} N_{TT} \\ N_{TL} \\ N_{LT} \\ N_{LL} \end{bmatrix} \tag{6.9}$$

The matrix inverse in eq. (6.7) solves for the expected number of fake di-lepton events in the loose signal sample. Changing the basis in eq. (6.9) to tight according to eq. (6.2) and eq. (6.1), the fake lepton contribution becomes:

$$\begin{aligned} N_f^{TT} &= N_{RF}^{TT} + N_{FR}^{TT} + N_{FF}^{TT} \\ &= r_1 f_2 N_{RF}^{ll} + f_1 r_2 N_{FR}^{ll} + f_1 f_2 N_{FF}^{ll} \\ &= \alpha r_1 f_2 \left[(f_1 - 1)(1 - r_2) N_{TT} + (1 - f_1) r_2 N_{TL} + f_1 (1 - r_2) N_{LT} - f_1 r_2 N_{LL} \right] \\ &\quad + \alpha f_1 r_2 \left[(r_1 - 1)(1 - f_2) N_{TT} + (1 - r_1) f_2 N_{TL} + r_1 (1 - f_2) N_{LT} - r_1 f_2 N_{LL} \right] \\ &\quad + \alpha f_1 f_2 \left[(1 - r_1)(1 - r_2) N_{TT} + (r_1 - 1) r_2 N_{TL} + r_1 (r_2 - 1) N_{LT} + r_1 r_2 N_{LL} \right] \end{aligned} \tag{6.10}$$

where

$$\alpha = \frac{1}{(r_1 - f_1)(r_2 - f_2)} \tag{6.11}$$

$\alpha > 1$, since $f < r$. For clarity, eq. (6.10) can be rewritten as:

$$N_f^{TT} = A N_{TT} + B N_{TL} + C N_{LT} + D N_{LL} \tag{6.12}$$

where

$$A = 1 - r_1 r_2 (1 - f_1)(1 - f_2)\alpha \qquad B = r_1 r_2 f_2 (1 - f_1)\alpha$$

$$C = r_1 r_2 f_1 (1 - f_2)\alpha \qquad D = -r_1 r_2 f_1 f_2 \alpha$$

If the fake rates and lepton efficiencies were *constants*, the fake lepton estimate would be obtained by counting the exclusive event numbers N_{TT}, N_{TL}, N_{LT} and N_{LL}, then weight by the corresponding constant numbers A through D. However, the rates and efficiencies are *not* constants but rather dependent on object quantities such as p_{T} and η of the leptons. Dependencies on topological variables such as the number of jets in each event or $E_{\mathrm{T}}^{\mathrm{miss}}$ is undesirable since that would require a more complicated transformation from the control region to the signal region.

With real efficiencies and fake rates dependent on object variables, the weights in eq. (6.12) must be applied to *each event* in the loose signal sample. The resulting yield, in a bin or in total, is the sum of these weights. For this procedure to work, the fake rate and efficiency for an object must be sufficiently different for any η and p_{T}, otherwise the denominator in the weight expressions, eq. (6.11), will be very small and the weights will be large.

The fake rate will depend greatly on the loose lepton definition. If the loose lepton is defined to be *very* loose, the rate will be low. This can be exploited by making simplifications to the weights expression eq. (6.12); higher order terms in f can be ignored. If one further assumes that the contribution from double fake lepton events can be neglected, then $D = 0$ and the fake di-lepton contribution can be written as:

$$N_f^{\prime TT} = f_2 N_{TL} + f_1 N_{LT} - \left[\frac{f_1(1-r_1)}{r_1} + \frac{f_r(1-r_2)}{r_2} \right] N_{TT} \tag{6.13}$$

In this approach the requirement on exactly 2 leptons is relaxed; one tight lepton and at least one loose (inclusive) is selected. Every pair of tight and loose lepton in the event contribute to the total weight.

The weights in eq. (6.13) are used for the low rate matrix method, while the weights in eq. (6.12) are used for the high rate method.

6.6 Real efficiency measurements

To estimate the real efficiencies, a control sample dominated by signal leptons is needed. Di-lepton events from Z decays provide such a sample, under the assumption that the efficiency is an object quantity, approximately independent of other objects in the event. For the high rate, events with two loose leptons are selected. In the case of the low rate leptons, events with one loose and one tight lepton are selected, again because the low rate loose leptons do not fulfil the lepton trigger requirements. The two leptons are required to have opposite sign and to have an invariant mass compatible with the Z mass, $|m_{ll} - 91| < 10$ GeV.

The number of loose leptons (N_{os}^{l}) and the number of loose leptons that also passes the tight requirements (N_{os}^{T}) are counted. The efficiency r may depend on one or several variables; detector geometry effects are taken into account by parametrization in η and resolution effects by a parametrization in p_{T}. Background events are accounted for by removing the contribution from same sign di-lepton events (N_{ss}^{T} and N_{ss}^{l}), also satisfying the invariant mass requirement. To summarize:

$$r(p_{\mathrm{T}}, \eta) = \frac{N_{os}^{T}(p_{\mathrm{T}}, \eta) - N_{ss}^{T}(p_{\mathrm{T}}, \eta)}{N_{os}^{l}(p_{\mathrm{T}}, \eta) - N_{ss}^{l}(p_{\mathrm{T}}, \eta)} \tag{6.14}$$

The efficiencies do depend on p_{T} and η, as indicated in eq. (6.14), but they are approximately constant in several regions. For the final measurement of

the efficiencies, regions in p_{T} and η with approximately constant efficiencies have been identified. The plots in Figure 6.2 show the real efficiency plotted against electron η for high rate and low rate for 35 pb^{-1} as well as high rate for 689 pb^{-1}. As comparison, the efficiencies from $Z \to \ell\ell$ MC samples, generated by PYTHIA, are shown as well. Some common features because of detector geometry are clearly visible, like the efficiency decrease for η around 1.5, which corresponds to the crack region in the calorimeter, c.f. the electron definition in section 5.4.1.

The low rate real efficiency for 35 pb^{-1} electrons ranges from $\sim 70\%$ for low p_{T} to $\sim 80\%$ at high p_{T}, with statistical uncertainties of a few percent. The high rate real efficiency is slightly higher, ranging from $\sim 80\%$ at low p_{T} to above 90% at high p_{T}, again with a statistical uncertainty of a few percent. The high rate electron real efficiency for 689 pb^{-1} is higher still because of the tightened loose electron definition. For muons the real efficiency is roughly constant; 96% for low rate muons and 99% for high rate muons, both for 35 pb^{-1} and 689 pb^{-1}, with statistical uncertainties below one percent.

Since the statistical uncertainties on the real efficiencies are at the level of at most a few percent they will be ignored in what follows. Systematic uncertainties of the efficiencies are not estimated beacuse the uncertainties of the fake rate are expected to dominate in the final calculation.

6.7 Fake rate measurements

Fake rates are estimated from either a jet or a lepton trigger stream. The jet stream contains events with at least one jet trigger fire, and this stream is used to estimate the rate for the low rate method, since these leptons are too loose to satisfy the lepton trigger requirements. The lepton stream contains events where at least one lepton trigger has fired, and this stream is used to estimate the rate for the high rate method. The same lepton triggers are used in the analysis and they are chosen to not be prescaled, which means that statistics is significantly higher compared to the jet stream with prescaled triggers.

All events are required to pass the standard quality cuts, described in section 5.3, except for an adjustment of the jet electron overlap removal: For each electron, if the closest jet is within $\Delta R < 0.1$ it is removed, unless it is the leading jet. All loose and reconstructed leptons are removed in a cone $\Delta R < 0.7$ around the leading jet. The event is then required to have at least one jet in the case of high rates and two jets for the low rates, to reduce trigger bias.

For the jet stream, events triggered by one of six different jet triggers are used, the jet thresholds are 20, 30, 40, 50, 75 and 95 GeV. In case of a jet 20 trigger, the leading jet is assumed to be the triggered object and its p_{T} is required to be > 20 GeV as well, to further reduce any trigger bias. There are corresponding requirements for the other jet thresholds. Events from the four lower jet thresholds are grouped together in a sample designated *jlow*, and

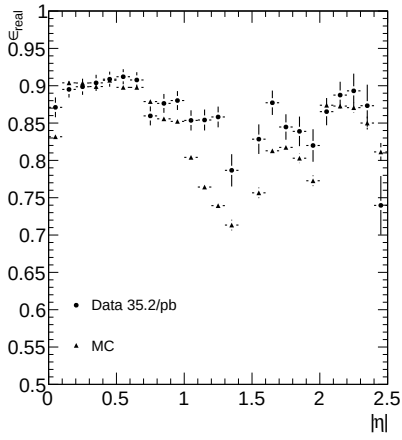

(a) High rate 35 pb^{-1}

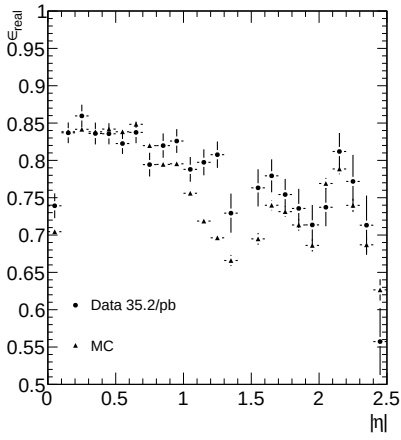

(b) Low rate 35 pb^{-1}

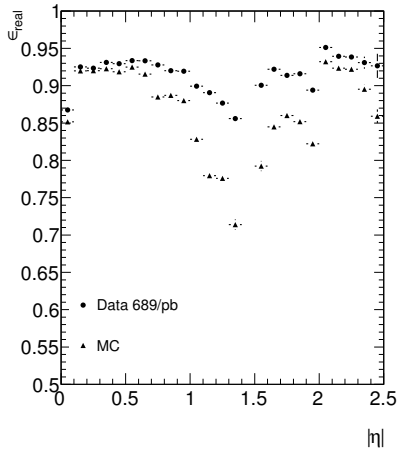

(c) High rate 689 pb^{-1}

Figure 6.2: Real efficiency for electrons as a function of lepton $|\eta|$ for low and high rate electrons in the 35 pb^{-1} dataset together with the high rate efficiency for the 689 pb^{-1} dataset. The efficiency drop in the calorimeter crack region for $|\eta|$ around 1.5 is clearly visible.

events for the two highest triggers are called *jhigh*. In the lepton stream, the same jet thresholds apply for the leading jet, but no jet trigger is required. Instead, a lepton trigger fire is required. The reason for having two jet trigger groups is to have an alternate handle on the uncertainties from event kinematics. This technique was only used for the 35 pb^{-1} dataset.

To get a sample free from signal leptons, an iterative cleaning process is implemented for the 35 pb^{-1} and 689 pb^{-1} datasets. The biggest concerns are contamination from $W+$jets and $Z+$jets, but other processes such as $t\bar{t}$ can

also contribute. Di-lepton events are suppressed by demanding that the events contain only one loose lepton, and consequently at most one tight lepton. $W+$ jets is suppressed by choosing a low $E_{\mathrm{T}}^{\mathrm{miss}}$ region[4]. The procedure uses a data driven MC normalization to remove the signal lepton contribution. In each step the rate is computed using the number of events in the low $E_{\mathrm{T}}^{\mathrm{miss}}$ regions as:

$$f = \frac{N^{T,low} - c^T N_{mc}^{T,low}}{N^{l,low} - c^l N_{mc}^{l,low}} \tag{6.15}$$

where c_T and c_l are MC scale factors, set to zero in the first iteration, $N^{T,low}$ ($N^{l,low}$) is the number of tight (loose) leptons in the low $E_{\mathrm{T}}^{\mathrm{miss}}$ region and $N_{mc}^{T,low}$ ($N_{mc}^{l,low}$) is the number of tight (loose) signal leptons in the low $E_{\mathrm{T}}^{\mathrm{miss}}$ region estimated from MC. When the rate has been estimated, the one lepton matrix method in eq. (6.4) is used to estimate the number of fake leptons in an extended control sample; for the 35 pb^{-1} dataset, this sample is obtained by increasing the $E_{\mathrm{T}}^{\mathrm{miss}}$ threshold, in the first iteration it coincides with the low $E_{\mathrm{T}}^{\mathrm{miss}}$ region, and in subsequent iterations it is increased by 10%. For the 689 pb^{-1} dataset the extended region is fixed to $E_{\mathrm{T}}^{\mathrm{miss}} < 40$ GeV. The number of estimated fake events $N_F^{T,high}$ in the high $E_{\mathrm{T}}^{\mathrm{miss}}$ region is then subtracted from the total number of events in the sample, to give an estimate of the contamination of real leptons. The MC scale factors are computed as:

$$c^T = \frac{N^{T,high} - N_F^{T,high}}{N_{mc}^{T,high}} \qquad c^l = \frac{N^{l,high} - N_F^{l,high}}{N_{mc}^{l,high}}$$

The values of c^T and c^l are then inserted in eq. (6.15) for the subsequent iteration, and a corrected rate is computed. After a few iterations, the rates converge.

6.8 Signal region extrapolation

The fake rates are highly dependent on the flavour composition of the sample, i.e. the fraction of fake leptons from heavy flavour hadrons, light flavour hadrons and photon conversions. Since the flavour compositions differ between the control and the signal regions, an extrapolation procedure has been implemented, which uses flavour compositions determined from MC together with a linear transformation. This procedure is only needed for electrons, a more direct method is sufficient for muons.

The control sample is split into three sub samples, labelled "b-tag", "c-tag" and anti "b-c-tag", and they are defined as:

- **b-tag** All leptons close to a jet tagged by the SV0 [49] b-tagger. This b-tagging algorithm attempts to reconstruct a secondary vertex inside the jet.

[4] $E_{\mathrm{T}}^{\mathrm{miss}} < 50$ GeV for low rate electrons, $E_{\mathrm{T}}^{\mathrm{miss}} < 20$ GeV for high rate electrons as well as low rate muons and $E_{\mathrm{T}}^{\mathrm{miss}} < 10$ GeV (20 GeV for 689 pb^{-1}) for high rate muons.

The fraction of fake leptons from heavy flavour jets is enhanced in this sample.

- **c-tag** All leptons that are within $\Delta R < 0.1$ of a conversion vertex. This sample is completely dominated by fake leptons from conversions.
- **anti b-c-tag** All leptons not satisfying the b-tag and c-tag requirements above. This sample is enriched in light flavour fake leptons.

Figures 6.3 and 6.4 show the fake rates with the different flavour tags, for high rate electrons and muons, and low rate electrons and muons.

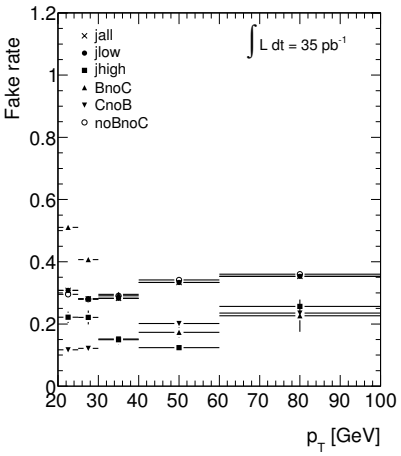

(a) Electron p_{T}, $35pb^{-1}$

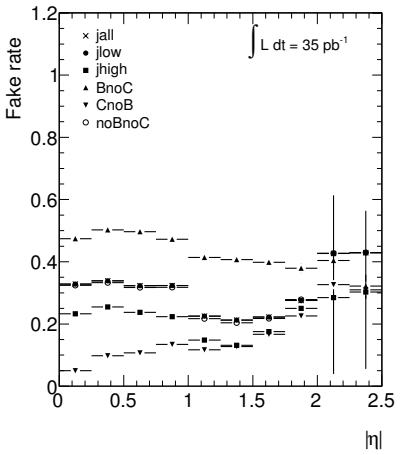

(b) Electron $|\eta|$, $35pb^{-1}$

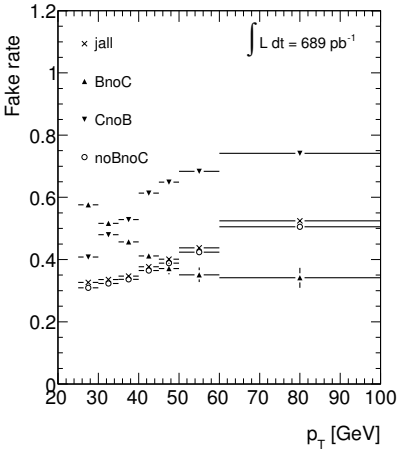

(c) Electron p_{T}, $689pb^{-1}$

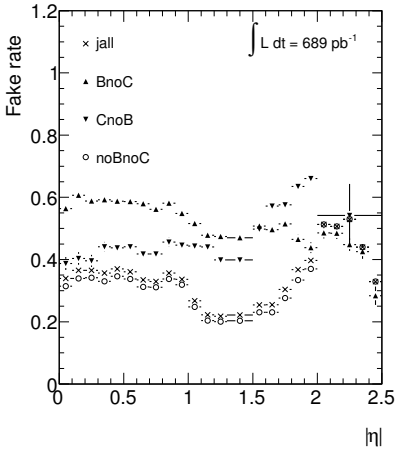

(d) Electron $|\eta|$, $689pb^{-1}$

Figure 6.3: High rate electron fake rate for different flavor tags.

The rates in the three sub samples in the control region, b-tag, c-tag and anti b-c-tag, are related to the "true" rates for heavy flavour, photon conversions

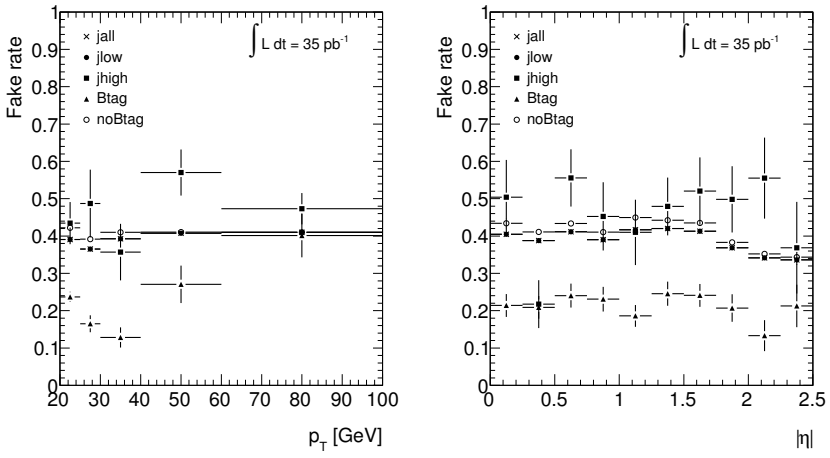

(a) Muon p_{T}, $35pb^{-1}$ (b) Muon $|\eta|$, $35pb^{-1}$

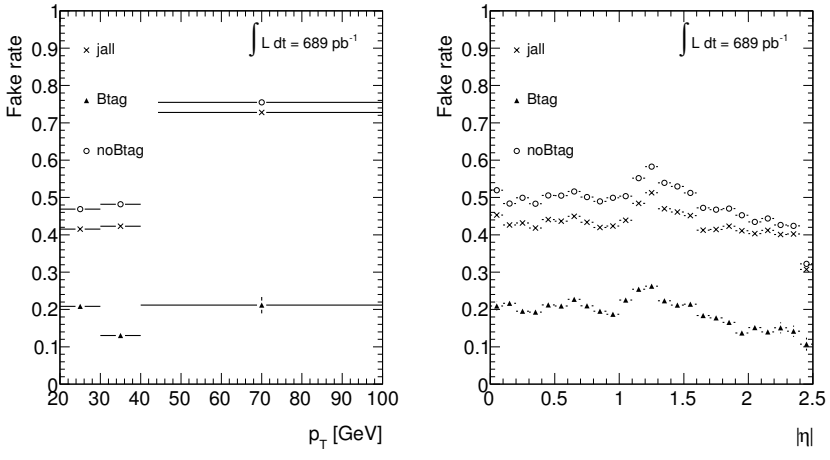

(c) Muon p_{T}, $689pb^{-1}$ (d) Muon $|\eta|$, $689pb^{-1}$

Figure 6.4: High rate muon fake rate for different flavor tags.

and light flavour by a matrix containing the flavour compositions:

$$\begin{pmatrix} R_{bt} \\ R_{ct} \\ R_{!bc} \end{pmatrix} = \begin{pmatrix} HF_{bt} & PC_{bt} & LF_{bt} \\ HF_{ct} & PC_{ct} & LF_{ct} \\ HF_{!bc} & PC_{!bc} & LF_{!bc} \end{pmatrix} \begin{pmatrix} R_{HF} \\ R_{PC} \\ R_{LF} \end{pmatrix} \tag{6.16}$$

where HF_x, PC_x and LF_x are the heavy flavour, conversion and light flavour fractions, x denotes the tagged sub samples: bt for the b-tag sample, ct for the conversion tag sample and $!bc$ for the light flavour sample with anti b-c-tag. All fractions are positive and less than one and their sum is one. R_x denotes the rates measured in the different sub samples.

Given the control region flavour composition, the matrix in eq. (6.16) can be inverted to give the rates R_{HF}, R_{PC} and R_{LF} that, to a first approximation, correspond to pure rates for the different flavour fractions. The extrapolation to the signal region is done using the composition of fake leptons in the signal MC samples[5].

p_{T}(GeV)	HF_{bt}	PC_{bt}	HF_{ct}	PC_{ct}	$HF_{!bc}$	$PC_{!bc}$
$20 \to 25$	0.81	0.034	0	1	0.12	0.11
$25 \to 30$	0.78	0.035	0	1	0.082	0.12
$30 \to \infty$	0.69	0.030	0	1	0.043	0.14

Table 6.1: Flavour composition of the control sample for high rate electrons, 35 pb^{-1}.

p_{T}(GeV)	HF_{bt}	PC_{bt}	HF_{ct}	PC_{ct}	$HF_{!bc}$	$PC_{!bc}$
$20 \to 25$	0.17	0.18	0	1	0.0091	0.30
$25 \to 30$	0.15	0.18	0	1	0.0074	0.30
$30 \to \infty$	0.13	0.16	0	1	0.064	0.28

Table 6.2: Flavour composition of the control sample for low rate electrons, 35 pb^{-1}.

p_{T}(GeV)	HF_{bt}	PC_{bt}	HF_{ct}	PC_{ct}	$HF_{!bc}$	$PC_{!bc}$	HF	LF
$25 \to 30$	0.91	0.02	0	1	0.19	0.11	0.27	0.21
$30 \to 40$	0.97	0.01	0	1	0.07	0.12	0.21	0.30
$40 \to \infty$	0.50	0.00	0	1	0.02	0.14	0.11	0.29

Table 6.3: Flavour composition of the control and signal samples for high rate electrons, 689 pb^{-1}.

The systematic uncertainty due to the unknown composition of the signal sample is estimated by assuming a 40% uncertainty on the flavour contents HF and PC for the 35 pb^{-1} dataset and 20% for the 689 pb^{-1} dataset. The extrapolated rate is given by the expression:

$$f_e(\vec{x}, p_{\mathrm{T}}, \eta) = HF(\vec{x})R_{HF}(p_{\mathrm{T}}, \eta) + PC(\vec{x})R_{PC}(p_{\mathrm{T}}, \eta) + LF(\vec{x})R_{LF}(p_{\mathrm{T}}, \eta)$$

where $\vec{x}$ represents the variable(s) that parametrize the flavour fractions in the signal region. In case of the low rate electrons for 35 pb^{-1}, the variables are N_{jets} and $E_{\mathrm{T}}^{\mathrm{miss}}$, and the flavour fractions are given in Table 6.4. For the high rate electrons with the 35 pb^{-1} dataset, the flavour fractions are constant with $HF = 23.2\%$ and $PC = 20.6\%$. In case of high rate electrons for 689 pb^{-1}

[5] $t\bar{t}$, $b\bar{b}$, single top, di-boson(WW, WZ and ZZ), W + jets and Z + jets

the flavour fractions, shown in Table 6.3, are parametrized by electron p_{T}. A special fake rate for use in a b-tagged signal sample is produced by using constant fractions $HF = 0.5$ and $PC = 0.1$.

For high rate muons in the 35 pb^{-1} dataset, the rate is the mean of the heavy flavour and light flavour rates and the systematic uncertainty is half the difference:

$$f_{\mu}(p_{\mathrm{T}}, \eta) = 0.5(R_{HF}(p_{\mathrm{T}}, \eta) + R_{LF}(p_{\mathrm{T}}, \eta))$$

$$\delta f_{\mu}(p_{\mathrm{T}}, \eta) = 0.5|R_{HF}(p_{\mathrm{T}}, \eta) - R_{LF}(p_{\mathrm{T}}, \eta)|$$

The rate for the 689 pb^{-1} dataset is computed by letting the heavy flavour fraction increase from 50% to 53%, and to 75% for the b-tagged rate.

Region	HF	PC
$N_{jets} < 2$ $E_{\mathrm{T}}^{\mathrm{miss}} < 40$	0.034	0.50
$N_{jets} \geq 2$ $E_{\mathrm{T}}^{\mathrm{miss}} < 40$	0.049	0.35
$N_{jets} < 2$ $E_{\mathrm{T}}^{\mathrm{miss}} > 40$	0.008	0.30
$N_{jets} \geq 2$ $E_{\mathrm{T}}^{\mathrm{miss}} > 40$	0.020	0.26

Table 6.4: Flavour composition of the signal sample for low rate electrons in the 35 pb^{-1} dataset.

The extrapolation is done for each p_{T} and η bin and the result for hMM electrons is shown in Table 6.5 and for hMM muons in Table 6.6 with both statistical and systematic uncertainties. For the lMM electrons the rate for electron goes from about 10% at low p_{T} to 5% at high p_{T}, for muons the rate is around 15%. The extrapolated fake rates for electrons in the 689 pb^{-1} dataset are shown in Table 6.7, and for muons in Table 6.8.

For the 3 pb^{-1} dataset, the extrapolated rate and uncertainties were estimated using only two different sub samples, a heavy flavour enriched sample and a heavy flavour depleted sample, and the extrapolation is done using flavour fractions from MC with 100% uncertainties.

Like the real efficiency, the fake rate for electrons has geometric dependencies, visible in the η plots of Figure 6.3, while the muon rate is flat in η, which can be seen in Figure 6.4. The electron flavor rates have strong kinematic dependencies, seen in the p_{T} plots of Figure 6.3. The b-tagging is efficient in enhancing or depleting the sample of fake leptons from heavy flavor, the purity is high as seen in Tables 6.1, 6.2 and 6.3. The kinematic and geometric dependencies are evened out by the extrapolation, but some differences in η regions and p_{T} remain, as visible in Tables 6.5, 6.6, 6.7 and 6.8.

p_T(GeV)	$\|\eta\|$	Fake rate
$20 \to 25$	$0 \to 1$	$0.34 \pm 0.95\% \pm 44\%$
$25 \to 30$	$0 \to 1$	$0.30 \pm 2.05\% \pm 39\%$
$30 \to 60$	$0 \to 1$	$0.29 \pm 3.6\% \pm 36\%$
$60 \to \infty$	$0 \to 1$	$0.31 \pm 33\% \pm 52\%$
$20 \to 25$	$1 \to 2.5$	$0.29 \pm 1.5\% \pm 38\%$
$25 \to 30$	$1 \to 2.5$	$0.28 \pm 3.0\% \pm 24\%$
$30 \to 60$	$1 \to 2.5$	$0.27 \pm 5.1\% \pm 24\%$
$60 \to \infty$	$1 \to 2.5$	$0.31 \pm 31\% \pm 24\%$

Table 6.5: Extrapolated high electron fake rates for the 35 pb^{-1} dataset with statistical and systematic uncertainties.

p_T(GeV)	$\|\eta\|$	Fake rate
$20 \to 30$	$0 \to 1.6$	$0.34 \pm 2.2\% \pm 33\%$
$30 \to \infty$	$0 \to 1.6$	$0.34 \pm 1.7\% \pm 41\%$
$20 \to 30$	$1.6 \to 2.5$	$0.36 \pm 2.6\% \pm 42\%$
$30 \to \infty$	$1.6 \to 2.5$	$0.34 \pm 2.6\% \pm 42\%$

Table 6.6: Extrapolated high muon fake rates for the 35 pb^{-1} dataset with statistical and systematic uncertainties.

6.9 Cross checks

In order to check the validity of the extrapolated fake rate from the previous section, the one lepton matrix in eq. (6.5) is applied in the ℓ+jetssample. Only the high rate is tested because the tight lepton trigger requirements prevent the testing of the low rate.

The plots in Figure 6.5 show the estimated fake lepton yield for electrons in events with at least one jet with the 35 pb^{-1} dataset, versus the kinematic variables lepton p_T and lepton η. The two bottom plots show results for a b-tagged sample. Figures 6.6 show the same plots for muons. In the figures, the contribution for all processes, except fake leptons, are taken from simulations. The model plus the fake lepton background agrees with data, and the same holds for the b-tag sample, where a larger contribution from heavy flavour fake leptons is expected. A cut $E_T^{miss} > 30$ GeV is applied.

An important variable is the transverse mass, denoted m_T, defined as:

$$m_T = \sqrt{2 p_T E_T^{miss} (1 - cos\Delta\phi)}$$

p_T(GeV)	$\|\eta\|$	Fake rate	B-tag fake rate
$25 \to 30$	$0.0 \to 1.0$	$0.35 \pm 0.5\% \pm 45\%$	$0.44 \pm 0.5\% \pm 36\%$
$30 \to 35$	$0.0 \to 1.0$	$0.35 \pm 1.0\% \pm 35\%$	$0.41 \pm 1.0\% \pm 29\%$
$35 \to 40$	$0.0 \to 1.0$	$0.35 \pm 2.0\% \pm 24\%$	$0.38 \pm 2.0\% \pm 22\%$
$40 \to 50$	$0.0 \to 1.0$	$0.35 \pm 3.2\% \pm 34\%$	$0.47 \pm 3.2\% \pm 25\%$
$50 \to \infty$	$0.0 \to 1.0$	$0.42 \pm 9.2\% \pm 48\%$	$0.37 \pm 9.2\% \pm 54\%$
$25 \to 30$	$1.0 \to 1.8$	$0.21 \pm 0.9\% \pm 76\%$	$0.31 \pm 0.9\% \pm 53\%$
$30 \to 35$	$1.0 \to 1.8$	$0.27 \pm 1.7\% \pm 48\%$	$0.31 \pm 1.7\% \pm 41\%$
$35 \to 40$	$1.0 \to 1.8$	$0.27 \pm 3.1\% \pm 50\%$	$0.29 \pm 3.1\% \pm 47\%$
$40 \to 50$	$1.0 \to 1.8$	$0.28 \pm 5.0\% \pm 56\%$	$0.41 \pm 5.0\% \pm 39\%$
$50 \to \infty$	$1.0 \to 1.8$	$0.35 \pm 9.0\% \pm 50\%$	$0.38 \pm 9.0\% \pm 45\%$
$25 \to 30$	$1.8 \to 2.5$	$0.40 \pm 1.9\% \pm 17\%$	$0.42 \pm 1.9\% \pm 17\%$
$30 \to 35$	$1.8 \to 2.5$	$0.44 \pm 3.9\% \pm 24\%$	$0.41 \pm 3.9\% \pm 26\%$
$35 \to 40$	$1.8 \to 2.5$	$0.45 \pm 5.9\% \pm 28\%$	$0.41 \pm 5.9\% \pm 30\%$
$40 \to 50$	$1.8 \to 2.5$	$0.46 \pm 8.1\% \pm 43\%$	$0.40 \pm 8.1\% \pm 50\%$
$50 \to \infty$	$1.8 \to 2.5$	$0.52 \pm 10\% \pm 33\%$	$0.47 \pm 10\% \pm 37\%$

Table 6.7: Extrapolated high electron fake rates for the 689 pb^{-1} dataset with statistical and systematic uncertainties.

p_T(GeV)	$\|\eta\|$	Fake rate	B-tag fake rate
$20 \to 30$	$0.0 \to 1.0$	$0.34 \pm 1.4\% \pm 40\%$	$0.28 \pm 48\% \pm 72\%$
$30 \to 40$	$0.0 \to 1.0$	$0.30 \pm 6.2\% \pm 58\%$	$0.22 \pm 78\% \pm 90\%$
$40 \to \infty$	$0.0 \to 1.0$	$0.47 \pm 17\% \pm 62\%$	$0.34 \pm 86\% \pm 59\%$
$20 \to 30$	$1.0 \to 1.6$	$0.37 \pm 1.7\% \pm 38\%$	$0.31 \pm 46\% \pm 65\%$
$30 \to 40$	$1.0 \to 1.6$	$0.33 \pm 7.9\% \pm 58\%$	$0.24 \pm 78\% \pm 82\%$
$40 \to \infty$	$1.0 \to 1.6$	$0.45 \pm 18\% \pm 60\%$	$0.33 \pm 81\% \pm 60\%$
$20 \to 30$	$1.6 \to 2.5$	$0.29 \pm 2.3\% \pm 45\%$	$0.23 \pm 56\% \pm 87\%$
$30 \to 40$	$1.6 \to 2.5$	$0.26 \pm 9.9\% \pm 64\%$	$0.18 \pm 90\% \pm 110\%$
$40 \to \infty$	$1.6 \to 2.5$	$0.46 \pm 19\% \pm 50\%$	$0.36 \pm 64\% \pm 55\%$

Table 6.8: Extrapolated high muon fake rates for the 689 pb^{-1} dataset with statistical and systematic uncertainties.

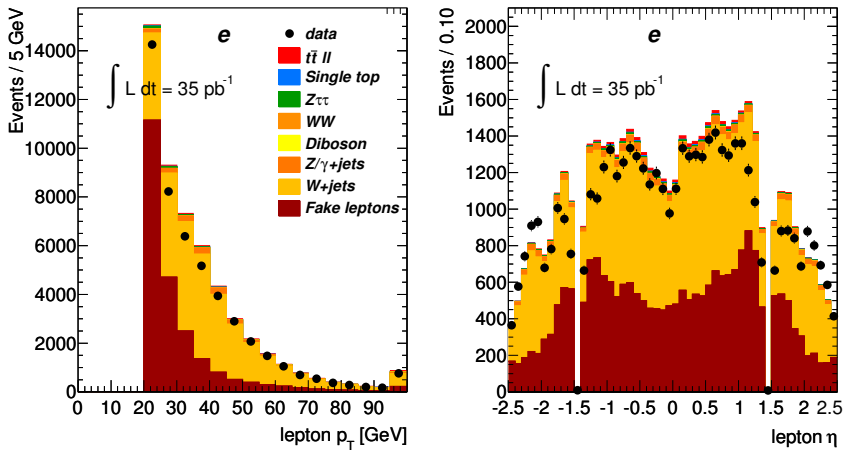

(a) Electron p_{T} (b) Electron η

(c) Electron p_{T}, b-tag sample (d) Electron η, b-tag sample

Figure 6.5: $e+$jets yield for kinematic variables in the region $E_{\mathrm{T}}^{\mathrm{miss}} > 30$ GeV for the 35 pb^{-1} dataset

where $\Delta\phi$ is the distance in ϕ between the $E_{\mathrm{T}}^{\mathrm{miss}}$ vector and the transverse lepton momentum vector and p_{T} is the transverse lepton momentum. The plots in Figure 6.7 show the estimated electron yield distributions in p_{T}, η and m_T for the 689 pb^{-1} dataset, with $E_{\mathrm{T}}^{\mathrm{miss}} > 30$ GeV and at least one jet in the events. Figure 6.8 show the same distributions but in a b-tagged region. The corresponding distributions for muons are shown in Figures 6.9 and 6.10.

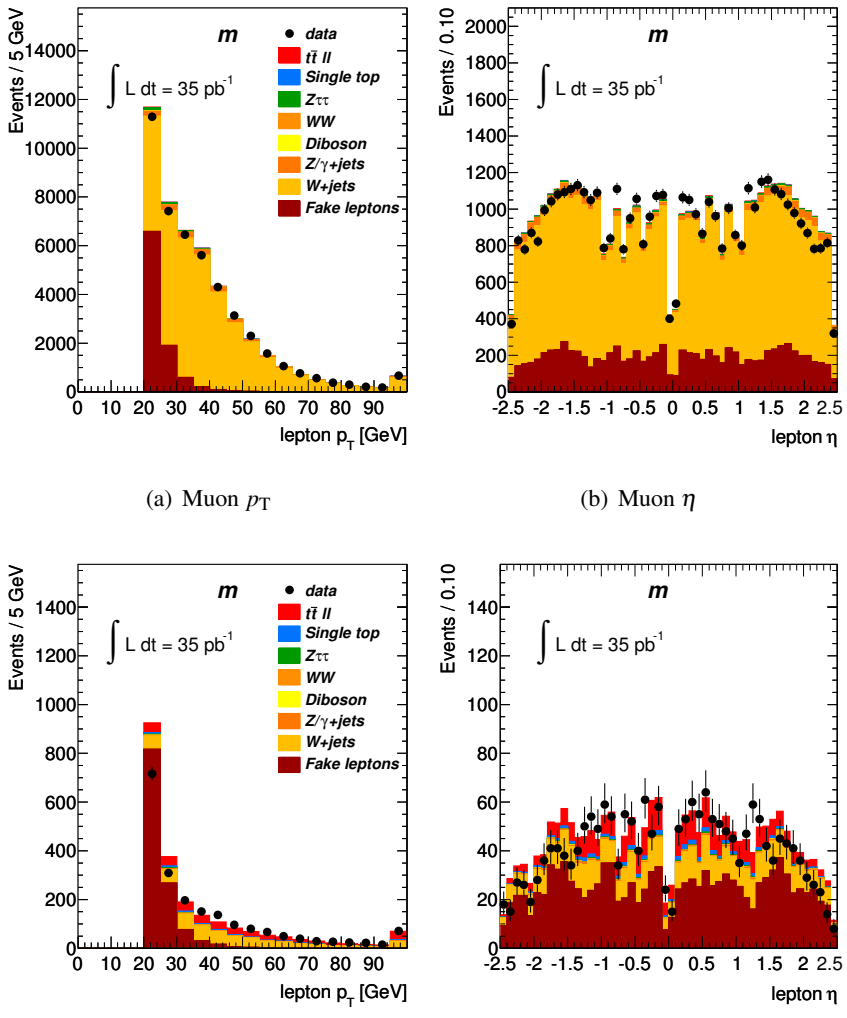

(a) Muon p_{T}

(b) Muon η

(c) Muon p_{T}, b-tag sample

(d) Muon η, b-tag sample

Figure 6.6: μ + jets yield for kinematic variables in the region $E_{\mathrm{T}}^{\mathrm{miss}} > 30$ GeV for the 35 pb^{-1} dataset

6.10 Fake di-lepton yield estimation

The matrix method, using weights given by eq. (6.12) and eq.(6.5), can now be applied to get an estimate of the fake lepton yield in the di-lepton signal region, defined in section 5.3, with relaxed cuts on jet multiplicity.

Table 6.9 shows the high rate fake lepton yield versus the number of jets in the 35 pb^{-1} dataset. Because of low statistics, the predicion for same charge lepton was used in the ee and $\mu\mu$ channels. A global systematic uncertainty of 50% has been introduced. Table 6.10 lists the prediction from the low rate

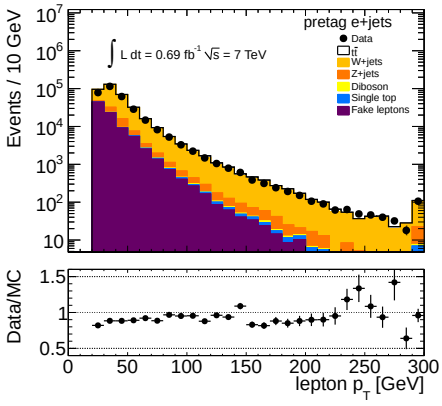

(a) Electron p_{T}

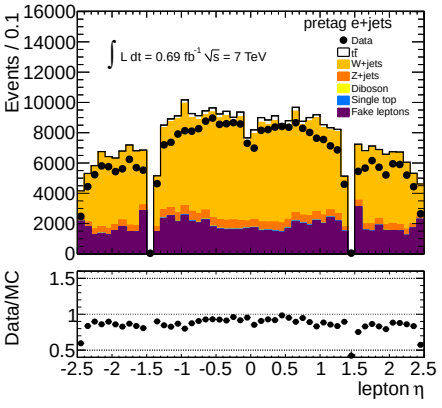

(b) Electron η

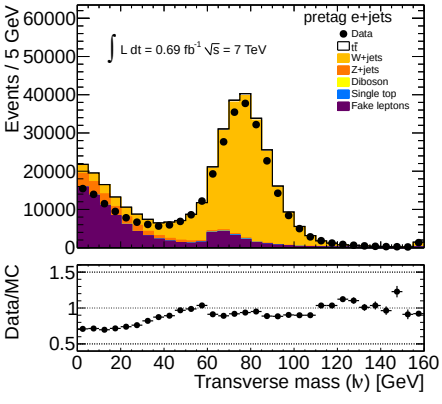

(c) Electron m_{T}

Figure 6.7: Electron + jets yield in the region $E_{\mathrm{T}}^{\mathrm{miss}} > 30$ GeV for the 689 pb^{-1} dataset.

method for the 35 pb^{-1} dataset. The results from the high and low rate methods agree in the signal region (≥ 2 jets).

The opposite sign fake lepton yield for the 689 pb^{-1} dataset is shown in Table 6.11.

N_{jets}	ee	eμ	$\mu\mu$
0	$1.61 \pm 0.81 \pm 0.81$	$0.0 \pm 0.7 \pm 0.35$	$0.47 \pm 0.48 \pm 0.24$
1	$0.55 \pm 0.54 \pm 0.28$	$1.12 \pm 0.93 \pm 0.56$	$0.0 \pm 0.46 \pm 0.23$
≥ 2	$0.98 \pm 0.7 \pm 0.5$	$1.92 \pm 1.52 \pm 0.96$	$0.44 \pm 0.44 \pm 0.22$

Table 6.9: High rate fake lepton yieldfor the 35 pb^{-1} dataset.

N_{jets}	ee	eμ	$\mu\mu$
0	$1.1 \pm 0.093 \pm 1.6$	$0.25 \pm 0.039 \pm 0.21$	$0.15 \pm 0.038 \pm 0.13$
1	$0.81 \pm 0.075 \pm 1.3$	$1.1 \pm 0.088 \pm 1.3$	$0.12 \pm 0.035 \pm 0.11$
$\geq$2	$1.1 \pm 0.092 \pm 1.4$	$2.5 \pm 0.14 \pm 3.5$	$0.055 \pm 0.027 \pm 0.055$

Table 6.10: Low rate fake lepton yield for the 35 pb^{-1} dataset.

N_{jets}	ee	eμ	$\mu\mu$
0	$3.3 \pm 2.5 \pm 3.3$	$3.8 \pm 2.3 \pm 3.8$	$0 \pm 0.39 \pm 0$
1	$4.1 \pm 2.8 \pm 4.1$	$19 \pm 5.6 \pm 19$	$0.4 \pm 1 \pm 0.4$
$\geq$2	$4.0 \pm 4.6 \pm 2.0$	$44 \pm 9.5 \pm 22$	$6.3 \pm 2.7 \pm 3.2$

Table 6.11: High rate fake lepton yield for the 689 pb^{-1} dataset.

Inclusive distributions in the variables jet multiplicity and $E_{\mathrm{T}}^{\mathrm{miss}}$ are shown for same charge $e\mu$ events in Figures 6.11 for the 35 pb^{-1} dataset. For the low rate method, the fake lepton yield is notably lower, while the statistics is higher. In the region dominated by $t\bar{t}$ (events with at least 2 jets and some $E_{\mathrm{T}}^{\mathrm{miss}}$) the methods are in agreement.

The result from the low rate method is used as a cross-check, while the result from the high rate method is the primary result, and it is used in the cross-section measurement in paper III and II. The differences between model and data in the control regions and the low statistics warrants a 50% systematic uncertainty in the entire region.

For the 689 pb^{-1} dataset, the jet multiplicity and $E_{\mathrm{T}}^{\mathrm{miss}}$ distributions for same sign $e\mu$ events are shown in Figure 6.12. In the region with high $E_{\mathrm{T}}^{\mathrm{miss}}$ or two jets, the model predictions agree with data, but in the low $E_{\mathrm{T}}^{\mathrm{miss}}$ and jet multiplicity bins there seems to be a deficit in the fake lepton predictions. To account for the differences, a systematic uncertainty of 50% is decided for

the opposite sign signal region with high $E_{\mathrm{T}}^{\mathrm{miss}}$ and two jets, and 100% for the region with 0 and 1 jets.

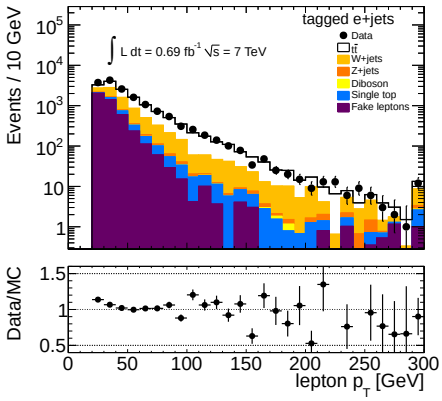

(a) Electron p_{T}

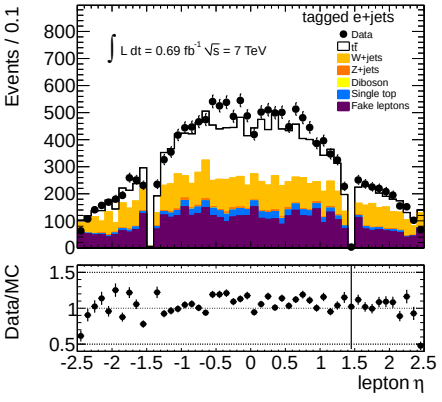

(b) Electron η

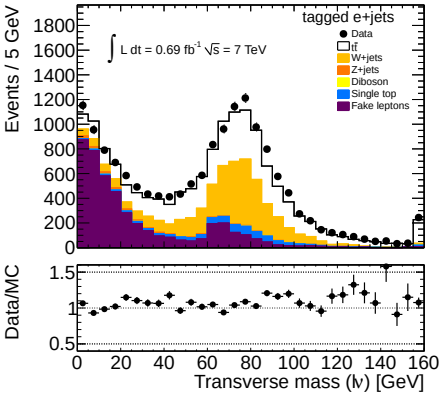

(c) Electron m_{T}

Figure 6.8: Electron + jets yield with b-tagging in the region $E_{\mathrm{T}}^{\mathrm{miss}} > 30$ GeV for the 689 pb^{-1} dataset.

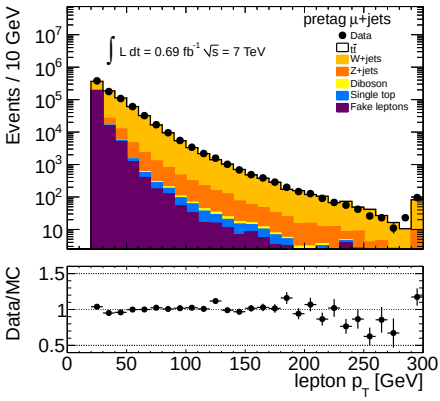

(a) μ p_{T}

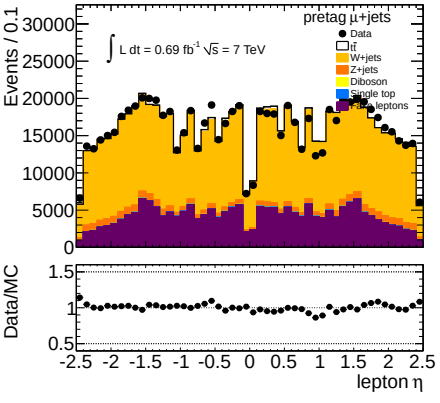

(b) μ η

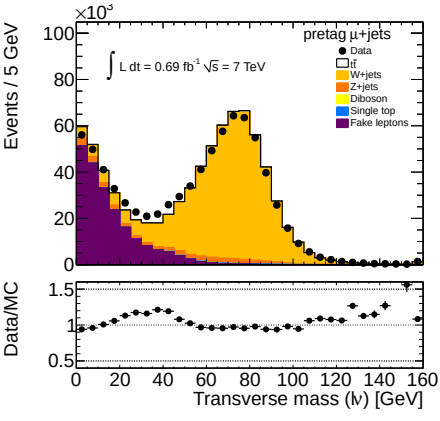

(c) μ m_{T}

Figure 6.9: μ + jets yield in the region $E_{\mathrm{T}}^{\mathrm{miss}} > 30$ GeV for the 689 pb^{-1} dataset.

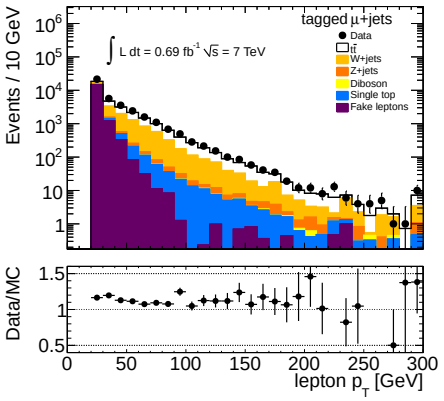

(a) μ p_{T}

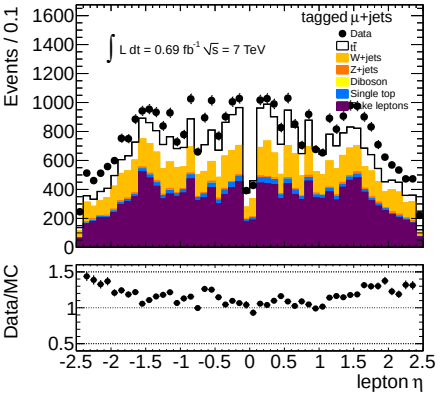

(b) μ η

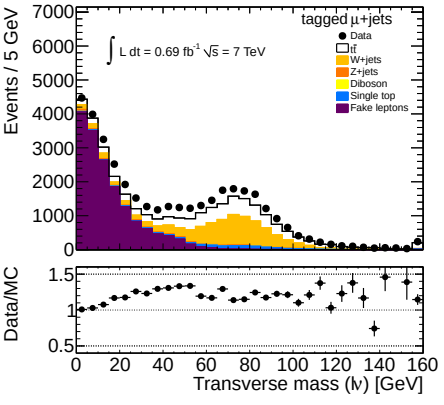

(c) μ m_{T}

Figure 6.10: μ + jets yield with b-tagging in the region $E_{\mathrm{T}}^{\mathrm{miss}} > 30$ GeV for the 689 pb^{-1} dataset.

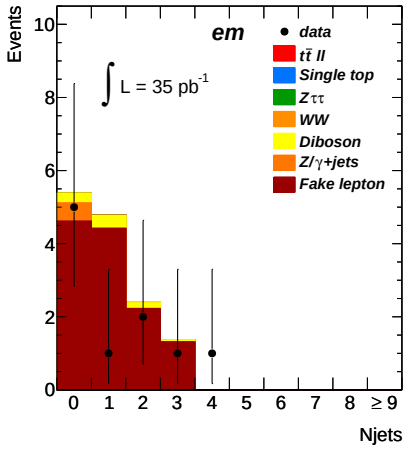

(a) Number of jets, high rate

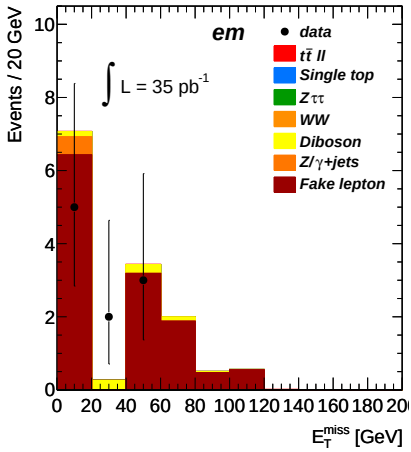

(b) $E_{\mathrm{T}}^{\mathrm{miss}}$, high rate

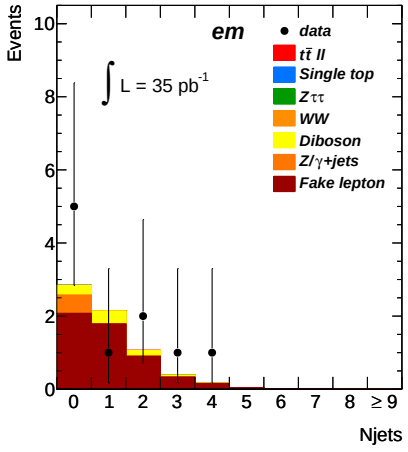

(c) Number of jets,low rate

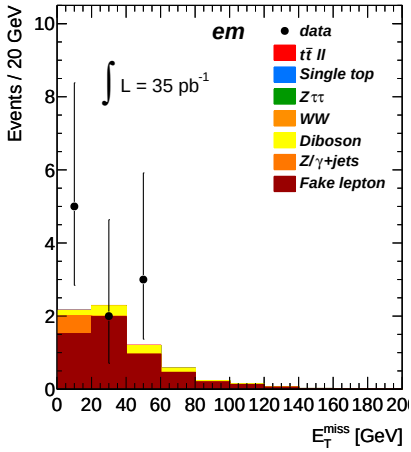

(d) $E_{\mathrm{T}}^{\mathrm{miss}}$, low rate

Figure 6.11: Fake lepton yield in eμ same sign for the 35 pb^{-1} dataset.

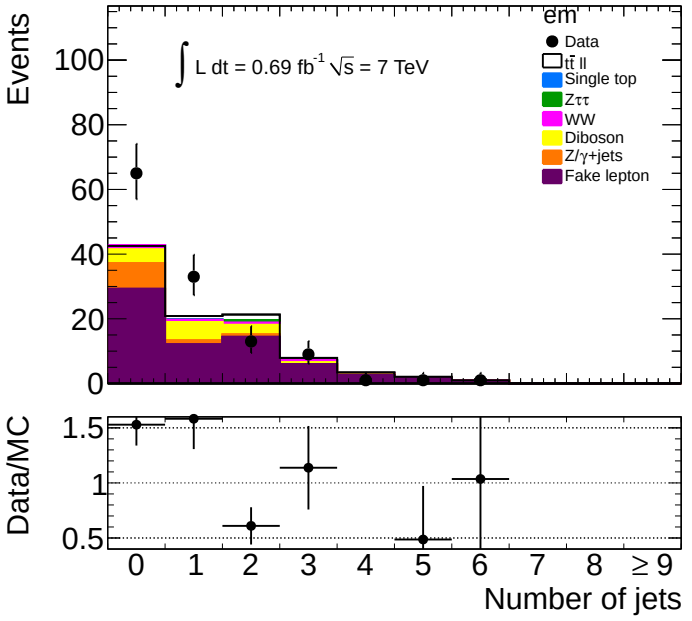

(a) Number of jets

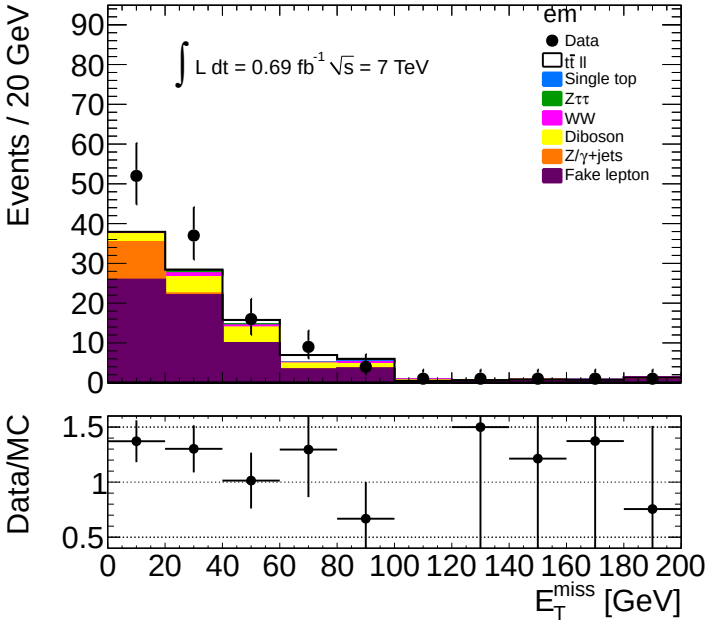

(b) $E_{\mathrm{T}}^{\mathrm{miss}}$

Figure 6.12: Fake lepton yield in eμ same sign for the 689 pb^{-1} dataset.

7 Measuring the total cross-section of $t\bar{t}$ pair production

7.1 Overview

Three measurements of the top pair production cross-section are presented in this chapter. All of them are made in the di-lepton channel, although the final published results are in some cases combined with measurements from other channels, e.q. $\ell+$jets and di-lepton with b-tagging. Successively larger data sets are used for the measurements, starting with 2.9 pb^{-1} in paper I through 35 pb^{-1} in III ending with 689 pb^{-1} in paper IV. All data were collected by ATLAS during 2010 and 2011.

The remarkable increase in integrated luminosity has been achieved by tuning the beam parameters, thus increasing the instantaneous luminosity, c.f. section 3.1. Increasing instantaneous luminosity has allowed for gradually tightened object and event selection criteria, to reduce background contamination of the signal region, and hereby lowering the uncertainty due to background modelling. The downside of increased instantaneous luminosity is that the effects of pile-up become more problematic. More protons in each bunch, smaller bunches and shorter time between colliding bunches increase the number of secondary interactions.

Pile-up can be either *in time* or *out of time*, where the former refers to multiple interactions within the same bunch crossing as the hard interaction, while the latter refers to interactions belonging to other bunch crossings, later or earlier. Both types of pile-up will increase the entire energy level in the detector, as well as giving rise to additional jets or energy depositions. Most objects and observables are affected by pile-up to varying degrees. As a consequence, systematic uncertainties may receive additional contribution from pile-up. The average number of interactions per bunch crossing will rise from 2 at the highest instantaneous luminosity in the 2.9 pb^{-1} dataset, to 5.6 in the 689 pb^{-1} dataset.

With increased running time of the experiment, experiences are gained that allow for more advanced analysis strategies. One example is the use of b-jet tagging methods. Identifying jets from hadronized b quarks from the top decay can greatly increase the signal efficiency for $t\bar{t}$. No b-tagging information is used for the di-lepton channel in the first analysis; but already in the second analysis of ten times the integrated luminosity, a baseline b-tagger [50] is used. An even more advanced b-tagger [51] is used in the third analysis. How-

ever, the introduction of b-tagger demands additional corrections and uncertainties; differences in b-tagging efficiencies between MC and data are taken into account by scaling MC to match the efficiency in data. The mis-tagging efficiency of light jets is dealt with in the same way. Uncertainties on both tagging and mis-tagging efficiencies are propagated to the final result. The background modelling also takes b-tagging into account. This is especially true for the fake lepton background estimate since application of a b-taggger changes the sample composition, which the fake rate is highly dependent upon, c.f. section 6.8.

The usefulness of $t\bar{t}$ total cross-section measurements is shown in references [52] and [53]. Here the total cross-section is used to find or constrain new physics in the language of an effective field theory.

7.2 Backgrounds

7.2.1 Z+jets

One of the largest background processes with two high p_{T} leptons in the final state, is $Z+$jets. At low di-lepton invariant mass and around the Z pole mass (91 GeV) this process dominates. To reduce its contribution, events with invariant mass below some threshold or around the Z pole mass are removed. There remains however a large contribution with a large uncertainty in the $t\bar{t}$ signal region. The uncertainty is both due to uncertainties in the $Z+$jets $E_{\mathrm{T}}^{\mathrm{miss}}$ spectrum and to theoretical uncertainties from the production of a Z together with at least 2 jets. A data driven method is used to estimate this background, which reduces the systematic uncertainty. The region around the Z peak is used as a control region. Other processes are insignificant in this region, but the small contributions are removed using the estimated MC values. Next, a scale factor is computed using the ratio between Z events in the control and signal regions, and this factor is used to extrapolate the $Z+$jets contribution from the control- to the signal region:

$$N_{data}^{SR} \approx \frac{N_{MC}^{SR}}{N_{MC}^{CR}} N_{data}^{CR}$$

where N_{data}^{CR} is the background corrected value.

7.2.2 Fake leptons

The fake lepton backgrounds were estimated using the methods described in chapter 6.

7.2.3 Other backgrounds

All other backgrounds to $t\bar{t}$, i.e. single top and dibosons, described in section 5.5, are simulated.

7.3 Cross-section measurement

The final cross-section is estimated by combining measurements in different channels. In the first paper using 3 pb^{-1} of data, the combination is between the three di-lepton and the two ℓ + jets channels. In the second analysis of 35 pb^{-1} the result is a combination of the three di-lepton channels and the two lepton plus track channels. In the last analysis, using 689 pb^{-1} of data, the di-lepton channels and the two lepton plus track channels are combined with ee and $\mu\mu$ with b-tagging.

A likelihood method is used to combine the channels, and the impact of systematic uncertainties is estimated using profiling, c.f. section 5.2. The number of expected events in channel i has background contributions from both MC (N_{ji}^{MC}) and data driven methods (N_{ji}^{DD}):

$$N_i^{exp}(\sigma_{t\bar{t}}, \mathscr{L}, \vec{\alpha}) = \mathscr{L} A_i(\vec{\alpha})\sigma_{t\bar{t}} + \sum_j N_{ij}^{MC}(\vec{\alpha}) + \sum_j N_{ij}^{DD}(\vec{\alpha})$$

A_i is the acceptance for channel i. For all three di-lepton channels together the acceptance is 1.43% in the first measurement, 1.69% in the second and 0.96% in the last. This expression for N^{exp} is used in a likelihood function, eq. (5.2). The background expectation uncertainty distributions are modelled differently depending in the analysis; in the first low luminosity analysis, they are modelled by Gamma distributions, because the expected yield is small and the uncertainties asymmetric. In the two subsequent analyses, Gaussian distributions are used, the uncertainties are assumed to be symmetric. The methods with likelihood ratios and profile likelihood ratios are used to estimate the cross-section and its uncertainties.

7.4 Results

The final cross-section values, and the SM predictions, are presented and compared in chapter 10. Table 7.1 shows an overview of the observed and total expected number of events as well as the expected number of $t\bar{t}$ events and predicted fake lepton background in each di-lepton channel. Two numbers are given for the fake lepton background, both the baseline estimate, which is the high rate method from chapter 6, and the backup low rate method labelled “Fake lepton II" in the table. The uncertainties are purely statistical for the observed event yield, and purely systematic for $t\bar{t}$ and the fake lepton pre-

dictions. The two fake lepton predictions agree within uncertainties, giving credibility to the presented numbers.

The impact of some important uncertainties are shown in Table 7.2. Statistical uncertainties dominate in the first two measurements, for all channels. As the luminosity reaches 689 pb^{-1}, systematic uncertainties, especially from jet energy scale (JES), dominate. Improvements in luminosity measurements [30, 54] reduced the uncertainty drastically from the earliest analysis of 2.9 pb^{-1} of data. As the object definitions and event selection is tightened, the expected fake lepton background decreases and so does its impact on the overall uncertainty.

The top mass dependency of the total cross-section was investigated in the 2.9 pb^{-1} analysis. It was found that changing the mass by ± 1 GeV changes the cross-section by $\mp 0.5\%$.

		2.9 pb^{-1}	35 pb^{-1}	689 pb^{-1}
ee	Observed	2	17	165
	Expected	1.79 ± 0.30	14 ± 1.7	149 ± 18
	$t\bar{t}$	1.19 ± 0.19	10.9 ± 1.2	124 ± 17
	Fake lepton I	0.16 ± 0.18	1.0 ± 0.9	4.0 ± 5.0
	Fake lepton II	0.10 ± 0.10	1.1 ± 1.4	–
$\mu\mu$	Observed	3	30	301
	Expected	2.75 ± 0.55	26.6 ± 2.1	$298 + 17/-20$
	$t\bar{t}$	1.87 ± 0.26	19.4 ± 1.5	$241 + 15/-18$
	Fake lepton I	-0.08 ± 0.07	0.5 ± 0.5	6.2 ± 4.1
	Fake lepton II	0.0 ± 0.06	0.06 ± 0.06	–
$e\mu$	Observed	4	57	963
	Expected	4.82 ± 0.65	55.1 ± 4.4	906 ± 54
	$t\bar{t}$	3.85 ± 0.51	45.7 ± 3.7	746 ± 42
	Fake lepton I	0.47 ± 0.28	1.9 ± 1.7	44 ± 24
	Fake lepton II	0.10 ± 0.10	2.5 ± 3.5	–

Table 7.1: Summary of predicted and observed number of events for each channel in the total cross-section measurements.

		2.9 pb^{-1} [%]	35 pb^{-1} [%]	689 pb^{-1} [%]
ee	Statistics	$+126/-79$	$+33/-29$	± 8.1
	Total systematic	$+44/-25$	$+15/-13$	$+16.4/-14.4$
	Jet reconstruction	$+13/-7$	$+5/-4$	± 5.7
	Fake leptons	$+24/-31$	$+8/-6$	± 3.3
	Luminosity	$+16/-11$	± 4	$+4.4/-3.8$
$\mu\mu$	Statistics	$+100/-67$	$+26/-23$	± 6.1
	Total systematic	$+30/-25$	$+9/-8$	$+8.8/-6.4$
	Jet reconstruction	$+9/-14$	$+4/-3$	$+6.4/-3.5$
	Fake leptons	$+1/-4$	$+3/-1$	$+1.5-1.3$
	Luminosity	$+16/-11$	± 4	$+4.4/-3.9$
$e\mu$	Statistics	$+77/-56$	$+17/-15$	± 3.9
	Total systematic	$+25/-14$	± 8	$+8.2/-6.8$
	Jet reconstruction	$+5/-3$	± 3	$+4.7/-3.2$
	Fake leptons	$+8/-15$	$+3/-4$	± 3.0
	Luminosity	$+14/-12$	± 4	± 4.2

Table 7.2: Overview of the impact on the final cross-section values for dominant uncertainties for each di-lepton channel.

8 Simultaneously measuring the total cross-sections of $t\bar{t}$, WW and $Z \to \tau^+\tau^-$

8.1 Overview

This chapter gives a summary and some background to the di-lepton template cross-section measurement in paper II. In this analysis the production cross-sections of three very important SM processes are simultaneously measured in 35 pb^{-1} of data taken during 2010. The strategy behind this analysis has been presented under several different names: in the ATLAS CSC book [36] it was referred to as "inclusive template analysis", and it has also been called AIDA (An Inclusive Di-lepton Analysis). in this context, inclusive refers to jet multiplicity, i.e. there is no jet multiplicity requirement.

Objects, electrons, jets and muons, in the events are selected according to the object definitions in section 5.4. All events satisfy the criteria given in section 5.3 with $E_{\mathrm{T}}^{\mathrm{miss}} > 40$ GeV in the ee and $\mu\mu$ channels, but without any requirement on the number of jets.

Section 8.2 gives an overview of the method, and the expected signal and background distributions are shown in section 8.3. Section 8.4 lists the systematics affecting this measurement, and section 8.5 gives the signal model and the likelihood function used to compute the results that are shown in section 8.6.

8.2 The method

The idea behind this analysis is to simultaneously measure the total production cross-sections of $t\bar{t}$, WW and $Z \to \tau^+\tau^-$ in the di-lepton channels. The basic observation is that these three processes populate different regions in a plane spanned by the topological variables jet multiplicity (number of jets) and $E_{\mathrm{T}}^{\mathrm{miss}}$. In the di-lepton final state of $t\bar{t}$ one expects at least two jets and a substantial amount of $E_{\mathrm{T}}^{\mathrm{miss}}$, because of the two neutrinos, c.f. section 2.8. In WW and $Z \to \tau^+\tau^-$ events one expects jets only from higher order QCD corrections. A substantial amount of $E_{\mathrm{T}}^{\mathrm{miss}}$ is again expected for WW events while less is expected in $Z \to \tau^+\tau^-$ events.

MC is assumed to give a good description of the shape of the distributions for the signal processes. Shape templates[1] parametrized by the number of jets and $E_{\mathrm{T}}^{\mathrm{miss}}$ in each event, are created for these three processes, for each of the three di-lepton channels. In addition, several absolute valued templates are created for the background processes single-top, dibosons (WZ and ZZ), Drell-Yan and fake leptons. Results from the high rate method, presented in chapter 6, are used to create the templates for the fake lepton background.

Template distributions for the $e\mu$ channel are shown in Figure 8.1. The lower right plot shows the absolute template for fake leptons while the other plots show normalized shape templates for the signal processes. There is one rectangle for each histogram bin, and their sizes are proportional to the bin content. Bins with negative content are marked with a cross. Some of the bins in the fake lepton template have a negative estimated yield, which is an inconvenient side effect of the fake lepton method when applied with limited statistics.

A likelihood function is constructed from the expected number of events in each bin, parametrized by the cross-sections for he signal processes and a set of nuisance parameters describing the systematic uncertainties in the analysis. The cross-section values are estimated in a profile likelihood fit combined with pseudo experiments, c.f. section 5.2.

8.3 Expected yield

Figures 8.2, 8.3 and 8.4 show the expected number of events in each $E_{\mathrm{T}}^{\mathrm{miss}}$ and jet multiplicity bin, for $e\mu$, ee and $\mu\mu$, compared to data. The expected yield for all processes, except for the fake lepton background, are taken from simulations using theoretical production cross-sections. Shaded areas show the systematic uncertainties on the expected yield, of which the fake lepton uncertainty is a large part.

Very few fake lepton events are predicted for the $\mu\mu$ channel, which seems to be consistent with data. In $e\mu$ the largest contribution to fake leptons is from fake electrons. The distributions of fake leptons are not smooth, and in some bins the prediction is negative, because of the problem with limited statistics mentioned earlier.

8.4 Systematic uncertainties

All significant systematic uncertainties, listed in section 5.6, are taken into account. Uncertainties affect not only the acceptances and background normalizations, but also the shape of the model templates.

[1] Histograms normalized to one, i.e. the bin sum is one.

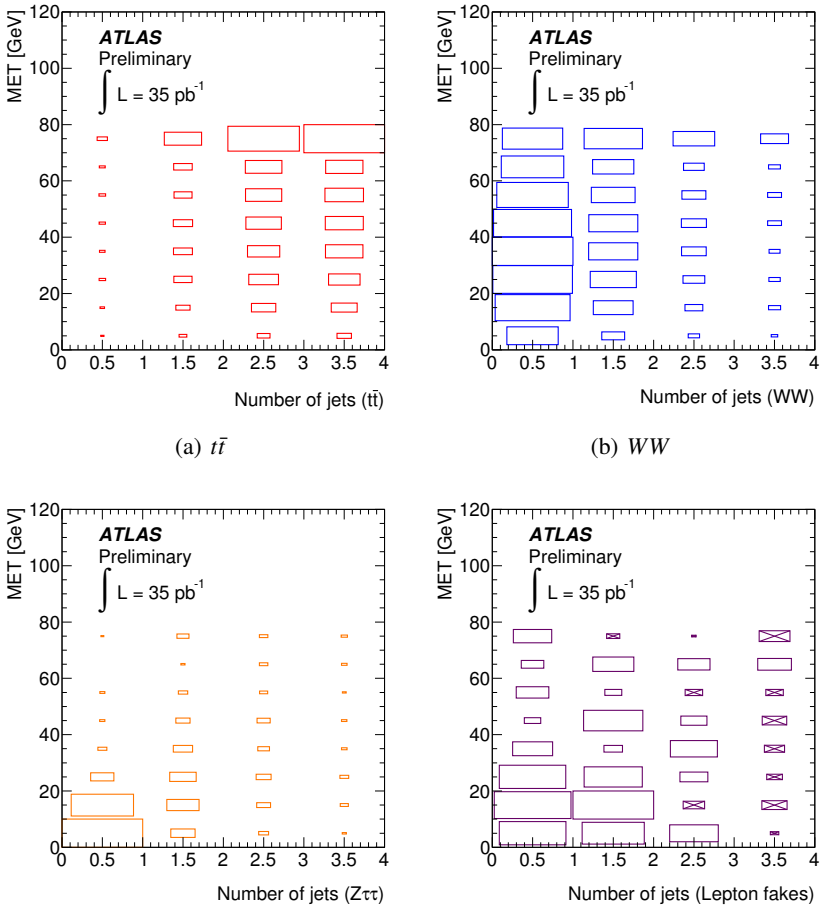

(a) $t\bar{t}$ (b) WW

(c) $Z \rightarrow \tau^+\tau^-$ (d) Fake leptons

Figure 8.1: Shape templates for $t\bar{t}$ WW and $Z \rightarrow \tau^+\tau^-$ as well as the absolute template for the fake lepton background in the $e\mu$ channel, parametrized by $E_{\mathrm{T}}^{\mathrm{miss}}$ and jet multiplicity.

The jet reconstruction efficiency uncertainty is estimated by removing 2% of the jets at random. The uncertainty from the fake lepton background normalization is constrained to 50% and the shape uncertainty is estimated by comparing the data driven shape to the shape from MC. The $Z+$jets normalization uncertainty is constrained to 50% and the uncertainty on the theoretical cross-section for single top is constrained to 10%. The parton shower uncertainty, affecting acceptance, is estimated by comparing result from POWHEG [55, 56, 57] with both HERWIG and PYTHIA and MC@NLO with HERWIG. Uncertainties from the modelling of ISR and FSR (see section 2.7) are estimated using the ACERMC generator [58]. Uncertainties on $t\bar{t}$ and single-top acceptance from the PDF:s is estimated to 2% per channel from the error band

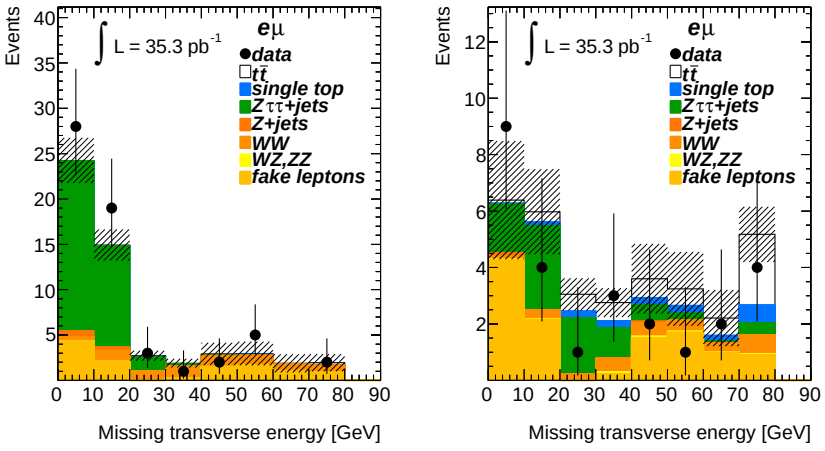

(a) jet bin 0 (b) jet bin 1

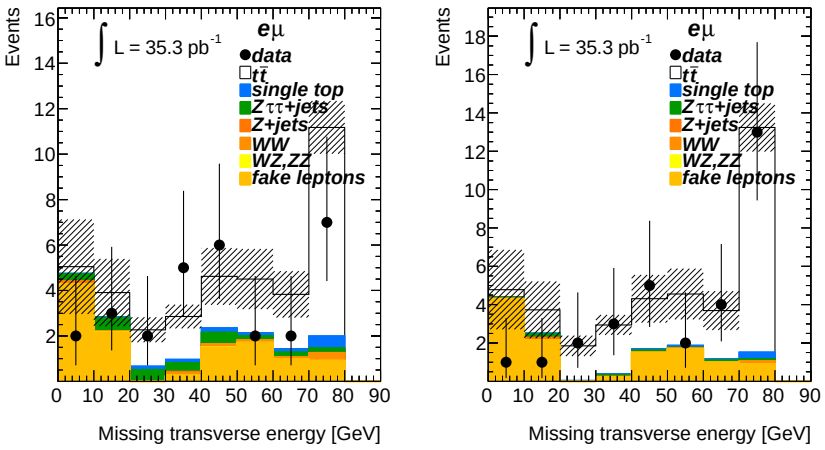

(c) jet bin 2 (d) jet bin 3

Figure 8.2: Templates for $e\mu$, compared to data in each jet multiplicity bin.

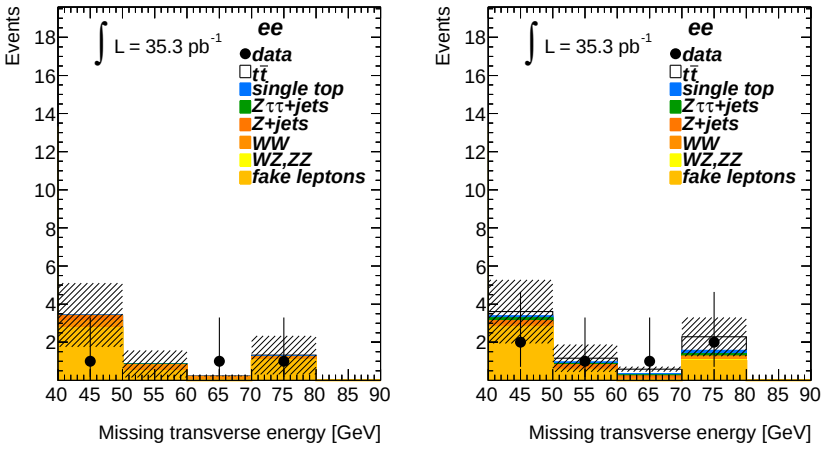

(a) jet bin 0 (b) jet bin 1

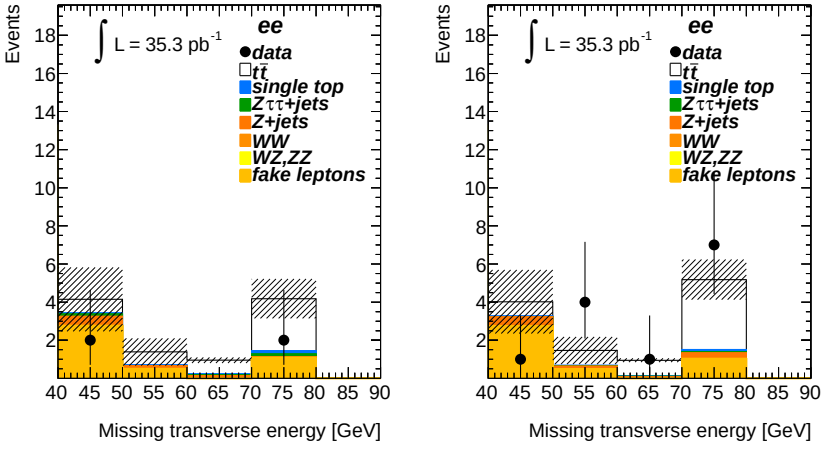

(c) jet bin 2 (d) jet bin 3

Figure 8.3: Templates for *ee*, compared to data in each jet multiplicity bin.

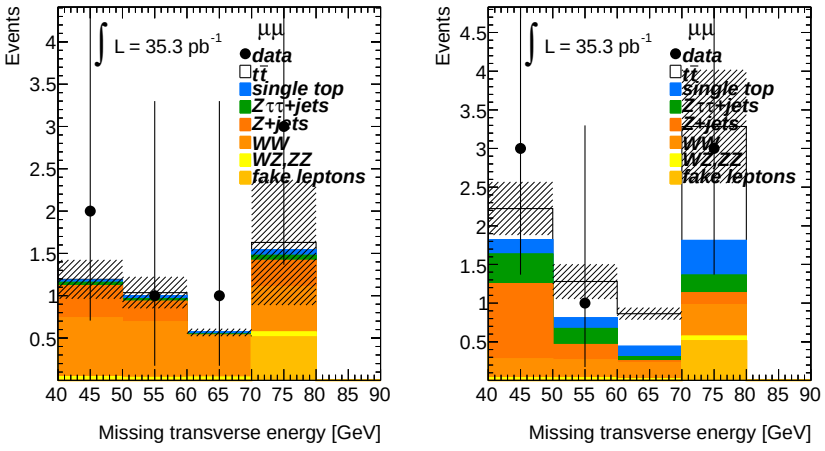

(a) jet bin 0 (b) jet bin 1

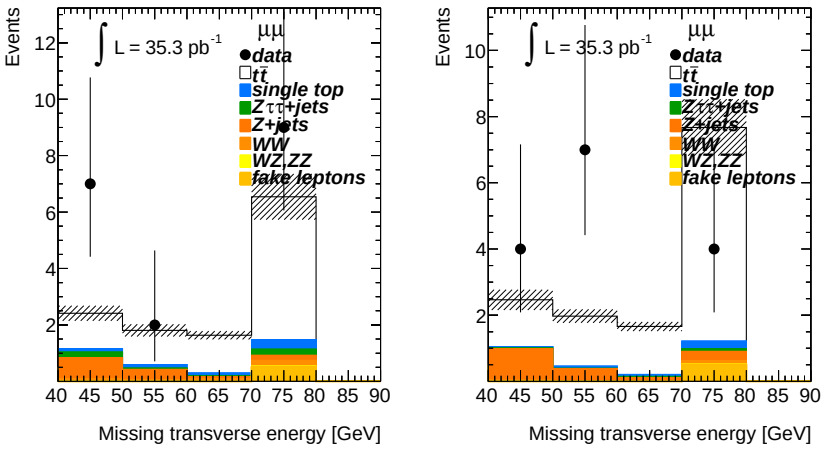

(c) jet bin 2 (d) jet bin 3

Figure 8.4: Templates for $\mu\mu$, compared to data in each jet multiplicity bin.

envelope for the PDF sets CTEQ66, MSTW08 [59] and NNPDF 2.0 [60]. The uncertainty on the total integrated luminosity, α_L, is constrained to 3.4%

All systematic uncertainties are incorporated into the final likelihood function as nuisance parameters, their impact on the total cross-section are estimated by profiling, except for JER, JEE, ISR/FSR, PS, GEN, PDF and the fake lepton shape. These uncertainties are one sided or have no well described dependency on a single parameter. All individual uncertainties are estimated in pseudo experiments using MC only. For a profiled uncertainty the corresponding d is kept at zero, and the result from the pseudo experiments is subtracted in quadrature from the total uncertainty, i.e. when all d are varied. The impact from a non-profiled uncertainty is estimated by symmetrizing the quadratic difference between nominal and shifted. The final uncertainty on the cross-sections is estimated by profiling in data, one cross-section at a time, and the non-profiled uncertainties are added in quadrature. A modified Barlow–Beeston method [61] is used to include uncertainties from MC statistics; one parameter per bin is used.

8.5 Signal model

The expected number of events in bin ij, for one channels, is given by:

$$N_{ij}^{pred}(\vec{\sigma}^{sig},\vec{\alpha}) = \sum_{sig} \mathscr{L} A^{sig}(\vec{\alpha}) T_{ij}^{sig}(\vec{\alpha}) \sigma^{sig} + \sum_{bkg} \mathscr{L} \tilde{A}^{bkg}(\vec{\alpha}) T_{ij}^{bkg}(\vec{\alpha}) \sigma^{bkg}(\vec{\alpha}) + \sum_{DD} N_{ij}^{DD}(\vec{\alpha}) \tag{8.1}$$

where *sig* denotes the signal processes: $t\bar{t}$, WW and $Z \to \tau^+\tau^-$, and *bkg* are the EWK background processes: di-bosons (WZ and ZZ) and single-top. The other ingredients are:

- A : Acceptance.
- $\mathscr{L}$: Integrated luminosity.
- $\vec{\alpha}$: Nuisance parameters for systematic uncertainties.
- T_{ij}^{sig} : Signal process template, normalized to 1.
- $\vec{\sigma}$: The cross-section for each signal processes.
- T_{ij}^{bkg} : Expected EWK background templates.
- σ^{bkg} : Constrained EWK background cross-sections.
- N_{ij}^{DD} : Data driven background estimates: Drell-Yan and fake leptons.

All templates (T_{ij} and N_{ij}^{DD}) are expanded, like the acceptances, in the systematic shifts and morphed by the corresponding nuisance parameters.

Assuming Poisson statistics for the number of observed events in each bin and Gaussian constraints for all nuisance parameters, the signal model is used in a likelihood function, eq. (5.2).

8.6 Results

The results from the inclusive template analysis are summarized in Tables 8.1 and 8.2. The first row shows cross-section for the $e\mu$ channel only, and the second row for all three channels combined. Row three shows recent measurements for comparison and the last line shows the theoretical cross-sections. The last column in Table 8.1 shows the measured $t\bar{t}$ cross-sections when the cross-section of $Z \to \tau^+\tau^-$and WW are constrained to within 15% of their predicted values. All measured cross-sections are compatible with the SM predictions and the other measured vales. The $t\bar{t}$ cross-section is compared to the other measurements in this thesis of the total cross-section in chapter 10.

	$\sigma_{t\bar{t}}$ [pb]	$\sigma_{t\bar{t}}$ [pb] (Z & WW fixed)
$e\mu$	163±28±14±6	164±27±14±5
All ch.	171±22±14±5	173±21±14±5
Other	$145 \pm 31^{+42}_{-27}$ (section 7.4)	$145 \pm 31^{+42}_{-27}$
Theory	165^{+11}_{-16} [19]	165^{+11}_{-16} [19]

Table 8.1: cross-sections for $t\bar{t}$ measured with the inclusive template method for 35.3 pb^{-1} of data, compared to recent measurements and theoretical values.

	σ_{WW} [pb]	$\sigma_{Z\to\tau\tau}$ [pb]
$e\mu$	46±26±9±2	1400±290±160±40
All ch.	59±21±12±2	1400±290±160±40
Other	41±15±6±4 [62]	$970 \pm 70 \pm 60 \pm 30$ [63]
Theory	$46.2^{+2.3}_{-2.3}$	1076^{+54}_{-54}

Table 8.2: cross-sections for WW and $Z \to \tau^+\tau^-$ measured with the inclusive template method for 35.3 pb^{-1} of data, compared to recent measurements and theoretical values.

The impact of each source of systematic uncertainty on the total cross-section for $t\bar{t}$ are shown in Table 8.3, for WW in Table 8.4 and for $Z \to \tau^+\tau^-$ in Table 8.5.

	Relative $\sigma_{t\bar{t}}$ uncert. [%]	
Source	$\pm e\mu$	$\pm$All
Statistical uncertainty	18	13
Object selection		
Lepton reconstruction, ID, trigger	5	5
Jet energy reconstruction	2	2
Background rates		
Fake leptons	2	1
Drell-Yan	1	1
Monte-Carlo simulation stat.	0	1
Signal simulation		
Initial/final state radiation	6	6
Generator	2	1
Integrated luminosity	4	3
Total systematic uncertainty	9	9
Stat. + syst. uncertainty	20	16

Table 8.3: Uncertainties on the $t\bar{t}$ cross-section.

All parameter values, including nuisance parameters, after the fit are shown in Table 8.6. The middle column shows the values in the fit of the $e\mu$ channel only, and the right column the values for the fit to all channels.

	Relative σ_{WW} uncert. [%]	
Source	$\pm e\mu$	$\pm$All
Statistical uncertainty	56	36
Object selection		
Lepton reconstruction, ID, trigger	5	5
Jet reconstruction efficiency	1	2
Jet energy reconstruction	1	13
Jet energy resolution	3	0
Background rates		
Fake leptons	17	13
Drell-Yan	1	2
Single top	0	5
Signal simulation		
Initial/final state radiation	2	2
Generator	4	1
Integrated luminosity	3	3
Total systematic uncertainty	19	20
Stat. + syst. uncertainty	59	41

Table 8.4: Uncertainties on the WW cross-section.

	Relative $\sigma_{Z\to\tau\tau}$ uncert. [%]	
Source	$\pm e\mu$	$\pm$All
Statistical uncertainty	21	21
Object selection		
Lepton reconstruction, ID, trigger	6	6
Background rates		
Fake leptons	10	10
Monte-Carlo simulation stat.	1	1
Signal simulation		
Initial/final state radiation	0	1
Integrated luminosity	3	3
Total systematic uncertainty	12	12
Stat. + syst. uncertainty	24	24

Table 8.5: Uncertainties on the $Z \to \tau\tau$ cross-section.

Parameter	Value ($e\mu$)	Value ($e\mu + ee + \mu\mu$)
$\sigma_{t\bar{t}}$	163^{+30}_{-27}	171^{+25}_{-23}
σ_{WW}	46^{+27}_{-22}	59^{+23}_{-20}
$\sigma_{Z\to\tau\tau}$	1396^{+311}_{-275}	1400^{+314}_{-278}
α_{efake}	$-0.31^{+0.58}_{-0.41}$	$-0.32^{+0.45}_{-0.37}$
α_{mfake}	$-0.31^{+0.58}_{-0.41}$	$-0.40^{+0.51}_{-0.37}$
α_{JES}	$0.85^{+0.88}_{-0.88}$	$0.78^{+0.84}_{-0.83}$
α_{L}	$0.00^{+0.03}_{-0.03}$	$0.00^{+0.03}_{-0.03}$
α_{DYee}	$0.00^{+0.50}_{-0.50}$	$0.05^{+0.48}_{-0.48}$
α_{DYmm}	$0.05^{+0.50}_{-0.50}$	$0.56^{+0.43}_{-0.43}$
α_{WZ}	$0.00^{+0.10}_{-0.10}$	$0.00^{+0.10}_{-0.10}$
α_{st}	$0.00^{+0.10}_{-0.10}$	$0.00^{+0.10}_{-0.10}$
$\alpha_{e\mu}$	$0.00^{+0.05}_{-0.05}$	$-0.01^{+0.05}_{-0.05}$
α_{ee}	–	$0.01^{+0.05}_{-0.05}$
$\alpha_{\mu\mu}$	–	$0.01^{+0.05}_{-0.05}$

Table 8.6: Parameters of the likelihood function after the maximum likelihood fit

9 Measuring the differential $t\bar{t}$ production cross-section

9.1 Overview

This chapter gives a summary of and some additional information to the measurement of the differential $t\bar{t}$ production cross-section in paper V.

After studying the total cross-section the natural step to take, when enough data has been collected, is to analyse differential cross-sections, i.e. the cross-section as a function of some variable: $d\sigma_{t\bar{t}}/dx$. Three different variables have been used in this analysis: the invariant mass ($m_{t\bar{t}}$), the transverse momentum ($p_{\mathrm{T}t\bar{t}}$) and the rapidity ($y_{t\bar{t}}$) of the $t\bar{t}$ system. From a theoretical point of view, new phenomena could alter the shape of the distribution in one of these variables relative the SM prediction, without changing the total cross-section significantly [52].

In order to compute the kinematic variables of the top pair, the four-vectors of the produced top quarks are needed. In this analysis, the four-vectors are obtained by making a kinematic likelihood fit of the event using reconstructed objects and $E_{\mathrm{T}}^{\mathrm{miss}}$. The same method of reconstructing $t\bar{t}$ four-vectors was previously used in a measurement of the $t\bar{t}$ charge asymmetry [64]. The reconstructed particle four-momenta have been smeared by experimental effects with respect to the parton four-vectors. To retain the unsmeared values, the distributions are unfolded [37]. The reason for presenting unfolded results is to enable comparisons of the measured values to theoretical predictions by people outside the ATLAS experiment that do not have access to the simulation infrastructure. To reduce the impact of systematic uncertainties, *relative* differential cross-sections $1/\sigma_{t\bar{t}}d\sigma_{t\bar{t}}/dx$ are measured. Large systematic uncertainties, correlated between the total and differential cross-section, cancel, giving a lower overall uncertainty.

9.2 Object and event selection

The basic event selection is one isolated lepton, electron or muon, fulfilling high quality requirements, together with at least four well separated jets and a substantial amount of $E_{\mathrm{T}}^{\mathrm{miss}}$, c.f. section 5.3.

9.2.1 Electrons

Electrons are reconstructed with tight quality requirements and $p_{\mathrm{T}} > 25$ GeV, as described in section 5.4.1. The calorimeter energy sum within a cone $\Delta R < 0.2$ is required to be less than 3.5 GeV. Every electron is also required to match an event filter trigger object.

In about 42% of the data taken, front end electronics malfunctioned in a specific region of the electro magnetic calorimeter ($0 < \eta < 1.45$ and $0.578 < \phi < 0.788$). An equal fraction (about 6%) of MC has to be adjusted to account for this loss of acceptance by removing electrons falling in this detector region. A systematic uncertainty is associated to this procedure.

Figure 9.1 show the invariant mass distributions for opposite sign electrons, with no requirement on jets. The uncertainty band includes all systematic uncertainties described in section 9.5, except for theory uncertainties. In particular, the electron energy scale and resolution as well as scale factor uncertainties are important. Agreement between data and MC, within uncertainties, indicate that the reconstruction, trigger and identification efficiencies as well as the electron energy scale and resolution are well described.

The $e+$jets signal region is defined by the cut $E_{\mathrm{T}}^{\mathrm{miss}} > 35$ GeV, to reduce the background contributions, primarily from fake leptons and $Z+$jets.

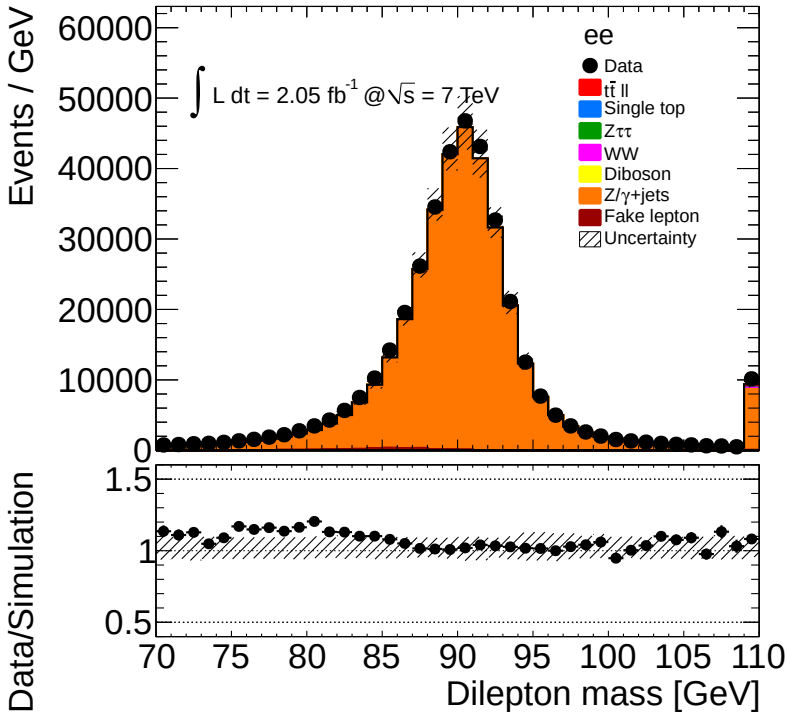

Figure 9.1: Invariant mass distribution for opposite sign electrons.

9.2.2 Muons

Muons are reconstructed as described in section 5.4.3. Analysis muons are required to have $p_{\mathrm{T}} > 20$ GeV and $|\eta| < 2.5$. The sum of all track p_{T} within 0.3 cone is required to be less than 4 GeV and the sum of calorimeter depositions in a cone 0.3 is also required to be less than 4 GeV.

No trigger matching is done for muons because of a misconfiguration in the simulation that affects muons with a p_{T} larger than 150 GeV. Instead the simulated events are re-weighted with the measured trigger efficiency.

The muon momentum is calibrated in data. Figure 9.2 shows the invariant mass distribution for opposite sign muons. The uncertainty band includes all uncertainties described in section 9.5 except for theory uncertainties. The distributions for MC and data agree within uncertainties, which shows that the scales, resolution and efficiencies for muons are well modelled.

In the signal region, a lower cut on $E_{\mathrm{T}}^{\mathrm{miss}} > 20$ GeV is applied together with a triangular cut $(E_{\mathrm{T}}^{\mathrm{miss}} + m_{\mathrm{T}}) > 60$ GeV. The latter cut is optimized to reduce the fake lepton background, in particular.

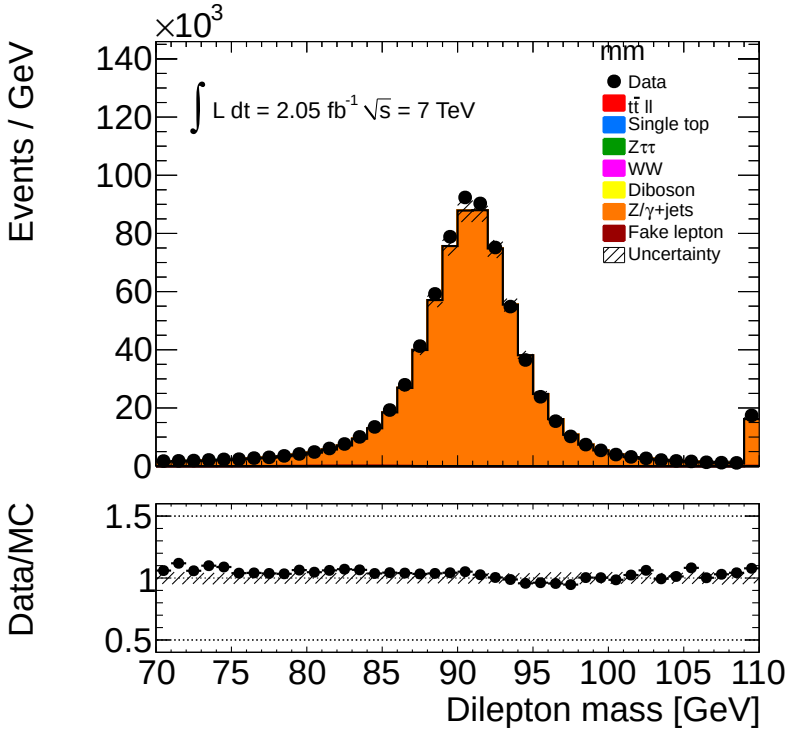

Figure 9.2: Invariant mass distribution for opposite sign muons.

9.2.3 Jets

Analysis level jets are selected according to the description in section 5.4.2. Jets are required to have $p_{\mathrm{T}} > 25$ GeV. The effects of the malfunctioning front end electronics are simulated by vetoing events. 42% of the events in MC, having a jet with $p_{\mathrm{T}} > 20$ GeV in the dead region, are rejected.

One of the largest systematic uncertainties is the jet energy scale (JES) and another jet related uncertainty is the jet energy resolution (JER). Figure 9.3 show a profile plot of the p_{T} balance in Z events. Opposite sign di-electron events have been selected that contain one jet that satisfy $\Delta R(jet, p_Z) > 3\pi/4$, i.e. the jet and the Z are roughly back-to-back. The spread in jet-$p_{\mathrm{T}}/Zp_{\mathrm{T}}$ is plotted as a function of Zp_{T} for both data and MC. The central values agree, implying that the energy scale of the jets match between data and MC. There is a tendency for data to have slightly larger spread, i.e. the jet energy resolution is slightly worse in data. To estimate the Jet Energy Resolution (JER) systematic the jet energy is smeared to give a worse jet resolution.

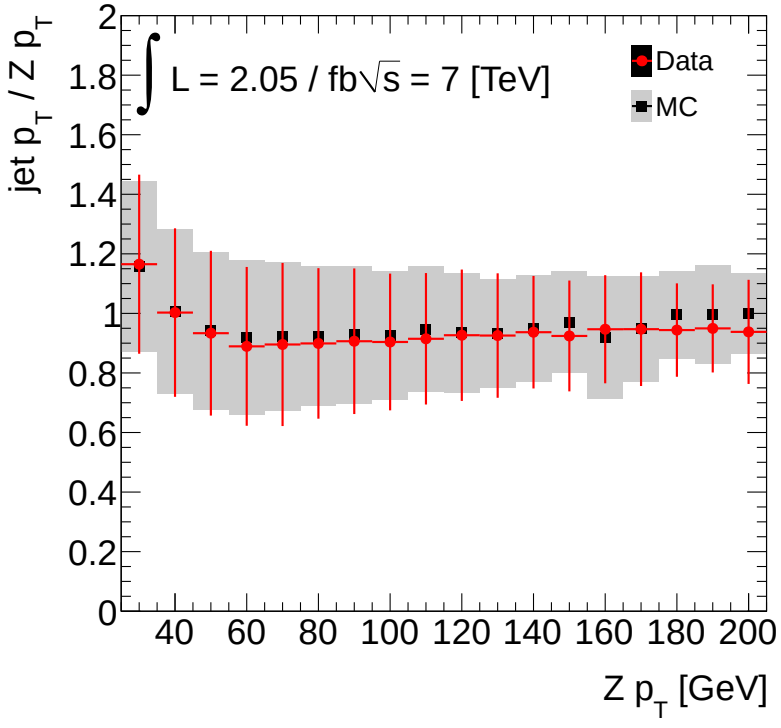

Figure 9.3: Comparison of jet energy resolution between data and MC. The plots shows profile histograms of the ration of jet to Z p_{T} in di-electron + jet events, where the di-electrons have a mass compatible with Z, and the Z and jet momenta are roughly back-to-back.

9.2.4 B-tagging

Since $t\bar{t}$ contains two possible b-jets, the use of jet b-tagging increases the purity of the signal region. A b-tagger consisting of two sub algorithms [51] is used in this analysis. The first tagger (JetFitter) attempts to reconstruct secondary vertices and the second tagger (IP3D) uses the impact parameter significance of the tracks belonging to the jet. In JetFitter, the path of the heavy hadron from the primary vertex to the decay vertex is approximated using a Kalman filter [65] and a likelihood discriminant between c- and b-hadrons is built out of masses, momenta and flight length significances. An artificial neural network combines the two taggers and constructs a single discriminating variable which is cut at a value corresponding to 70% b-tagging efficiency in $t\bar{t}$ events and a light jet rejection of 99 together with a c-jet rejection of 5.

There are differences between the tagging efficiencies in data and simulation. To compensate for this, scale factors are applied to MC. There are factors both for tagging efficiency of b-jets and mis-tagging efficiency for light jets.

Figure 9.4 show data and MC comparisons of tag rates for the $e+$jets and $\mu+$jets channels, as a function of jet p_{T}. The tag rate is computed by dividing the number of tagged jets by the total number of jets, the tagging efficiency scale factors are included in case of MC. The plots show the data tag rate divided by the MC tag rate. Data and MC are in agreement, especially in the high p_{T} region, where the b-tagger was less thoroughly tested.

Figure 9.6 show the jet multiplicity distributions in the two channels for events with at least one b-tagged jet. The signal purity can be seen to increase with respect to the un-tagged sample shown in Figure 9.5. The model predictions agree with data, within uncertainties, which shows that the background normalizations are well estimated. In Figure 9.7 the b-tag multiplicity distributions are shown. The results corroborate the conclusion drawn from Figure 9.4, that the tag rates in data and MC are compatible within uncertainties.

9.3 Backgrounds

9.3.1 Fake leptons

The fake lepton background is estimated using a single lepton matrix method like the one outlined in chapter 6. Fake rates are estimated in a $\ell+$jets region dominated by fake leptons; this is a low $E_{\mathrm{T}}^{\mathrm{miss}}$ region, slightly different between $e+$jets and $\mu+$jets. The contribution from real leptons is subtracted using simulation of $W+$jets and $Z+$jets, the dominating real lepton processes in this region.

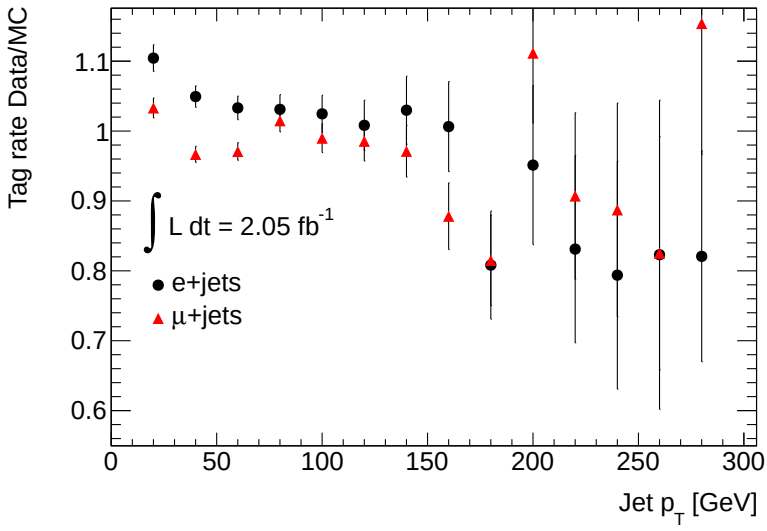

Figure 9.4: B-tag rate comparisons between data and simulation as a function of jet p_{T}. Events are selected according to section 9.2.2 for $e+$jets and according to section 9.2.2 for $\mu+$jets. Only statistical uncertainties are included.

Fake muons

A loose muon is defined by removing the isolation requirement on the tight muon. The fake rate is measured in a $\mu+$jets sample with $m_{\mathrm{T}} < 20$ GeV and a triangular cut $E_{\mathrm{T}}^{\mathrm{miss}} + m_{\mathrm{T}} < 60$ GeV.

Fake electrons

A loose electron is a medium electron with additional requirements on a hit in the pixel b-layer and a loosened isolation requirement, from 3.5 to 6 GeV. The fake rate is measured in a $e+$jets control sample defined by 5 GeV $< E_{\mathrm{T}}^{\mathrm{miss}} <$ 20 GeV

9.3.2 W+jets

As $W+$jets is the largest process after $t\bar{t}$ in the signal region, an accurate estimate is required. A three stage data driven method is used to normalize the MC generated distributions. The base of the estimate are the six ALPGEN samples for W production in association with zero to five partons, assumed to be massless. Zero mass is a good approximation for light quark production, but for production of b and c quarks, mass effects have to be included. Separate ALPGEN samples for Wbb+jets, Wcc+jets and Wc+jets exists for up to a total of five outgoing partons[1]. The first step is to estimate the flavour composition, i.e. the fractions of the W+light, Wbb, Wcc and Wc contributions. The method

[1]The cross-section for Wb+jets is very small and thus ignored.

uses measurements of one lepton plus one or two jets, with a possible b-tag. Equations containing the different heavy flavour fractions are then solved. The number of unknowns are reduced by estimating fractions between Wbb in one and two jets and the fraction between Wcc and Wbb, from simulation. The W+light jet fraction is adjusted to keep the overall normalization constant.

In the second step, the $W+$jets normalization is estimated from data with a method that exploits the fact that W production is charge asymmetric in proton-proton collisions; roughly 40% more W^+ is produced. One of the underlying, and well founded [59, 66, 67], assumptions is that this ratio (r) between W^+ and W^- can be accurately computed from MC:

$$r = \frac{N_{W^+}^{MC}}{N_{W^-}^{MC}} = \frac{N_{W^+}^{data}}{N_{W^-}^{data}} \tag{9.1}$$

Next, one assumes that the dominating source of charge asymmetry in data is due to $W+$jets (the small contribution from single top is removed by subtracting the MC expectation):

$$N_{W^+}^{data} - N_{W^-}^{data} \approx N_{+}^{data} - N_{-}^{data} \tag{9.2}$$

Equation (9.1) and (9.2) can be used to solve for $N_{W^+}^{data}$ and $N_{W^-}^{data}$:

$$N_{W^+}^{data} = \frac{r}{r-1}(N_{+}^{data} - N_{-}^{data}) \qquad N_{W^-}^{data} = \frac{1}{r-1}(N_{+}^{data} - N_{-}^{data})$$

and the expression for the total $W+$jets estimate becomes:

$$N_W = N_{W^+}^{data} + N_{W^-}^{data} = \frac{r+1}{r-1}(N_{+}^{data} - N_{-}^{data}) \tag{9.3}$$

Finally, the W normalization for b-tagged events has to be estimated, which is done using a method similar to the one used in paper I. The plots of the transverse mass in Figure 9.8, with cuts on jet multiplicity and $E_{\mathrm{T}}^{\mathrm{miss}}$, show agreement between data and model within uncertainties.

9.4 Reconstruction of event kinematics

The aim of the event kinematics reconstruction is to get the complete four-vectors of the two top quarks. Given an event with at least four jets, one isolated lepton and $E_{\mathrm{T}}^{\mathrm{miss}}$, there are several ways to assign the jets to outgoing partons in the $t\bar{t}$ decay, see Figure 2.6(b). If there are more than five jets in the event, only the five leading jets, i.e. with highest p_{T}, are considered. A likelihood is constructed out of a possible assignment of the jets to outgoing partons in the event, combined with the lepton and the neutrino momenta. The likelihood is then maximized once for each possible jet permutation, and the permutation with the largest likelihood is kept.

The first step in the kinematic reconstruction is to approximate the neutrino z-component by combining the lepton four-vector with the transverse $E_{\mathrm{T}}^{\mathrm{miss}}$ components and demanding that the sum should be compatible with the four-vector of an on-shell W. Since this is a second degree equation, there might be two real solutions that can serve as initial values.

The likelihood consists of two parts: the transfer function part and the Breit-Wigner part. A transfer function ($f(\hat{E},E)$) will give the probability for a particle of true energy E to be reconstructed with energy $\hat{E}$. There are separate transfer functions for b-jets as well as light jets, leptons (both e and μ) and neutrino momenta. The Breit-Wigner part contains factors for both leptonic and hadronic W and top decays. The full likelihood can be summarized as:

$$\begin{aligned}\mathcal{L} \;=\; & f_b(\hat{E}_b^{lep},E_b^{lep})f_b(\hat{E}_b^{had},E_b^{had}) \\ & f_{light}(\hat{E}_{light}^{1},E_{light}^{1})f_{light}(\hat{E}_{light}^{2},E_{light}^{2}) \\ & f_{lept}(\hat{E}_{lept},E_{lept})f_x(\hat{E}_x^{miss},E_x^{miss})f_y(\hat{E}_y^{miss},E_y^{miss}) \\ & BW(\hat{M}_W^{lept},M_W,\Gamma_W)BW(\hat{M}_W^{had},M_W,\Gamma_W) \\ & BW(\hat{M}_t^{lept},M_t,\Gamma_t)BW(\hat{M}_t^{had},M_t,\Gamma_t)\varepsilon_b \end{aligned} \tag{9.4}$$

where a quantity with circumflex denotes a free (output) parameter in the likelihood fit. Quantities with a superscript $lept$ (had) means that it belongs to the leptonic (hadronic) W decay branch. ε_b is a factor that take b-tagging efficiency and light jet rejection into account. A measured b-tagged jet that is assigned to a b in the top decay will contribute with a factor of the tagging efficiency, i.e. probability for tagging a true b-jet. If the b in the top decay is assigned a jet without b-tag, there will be a factor $1-\varepsilon$, and the same for light jets and the rejection efficiency.

Figure 1 of paper V show the distributions of the negative log likelihood for $e+$jets and $\mu+$jets. The region below -52 corresponds to badly reconstructed events, typically one jet in the $t\bar{t}$ decay escapes detection because of the acceptance limits, and an ISR-, or possibly FSR-, jet is reconstructed and this combination happens to give the largest likelihood.

The plots in Figure 2 of paper V show the reconstructed $t\bar{t}$ mass, $t\bar{t}$ p_{T} and rapidity distributions, for events with a cut on likelihood and b-tagging requirement.

9.5 Systematic uncertainties

The systematics listed in section 5.6 apply to this analysis, with some modifications and additions. There is an uncertainty associated with the dead calorimeter region that is estimated by varying the jet threshold ± 4 GeV. The total PDF uncertainty is the convolution of the uncertainties from the 44 pdf:s for CTEQ66, the 40 pdf:s of MSTW2008 and the 100 pdf:s in NNPDF, according to a prescription in reference [68]. For $W+$jets the normalization

uncertainty is estimated in the data driven method and the shape uncertainty is taken from MC. The normalization uncertainty for $Z+$jets is 48%, and for fake leptons it is 50% in the pretag sample and 100% in the tagged sample. The uncertainty from ISR and FSR modelling is estimated by varying parameters accoring to the Perugia tune [69], using the AcerMC generator [58]. The uncertainty for ISR and FSR in each bin is the difference between a shifted sample and a baseline $t\bar{t}$ AcerMC sample.

9.6 Unfolding, combination and propagation of uncertainties

The starting point for the unfolding and treatment of uncertainties is the total cross-section formula eq. (5.1). For differential measurements one has to take *migration* into account, i.e. the fact that the reconstructed variable is smeared with respect to the true variable. Let M_{ij} denote the probability for an event with true value in bin j to have a reconstructed value in bin i. M is called the migration matrix. The differential cross-section for bin j can now be written:

$$\sigma_j = \frac{\sum_i M_{ji}^{-1}(N_i^{data} - N_i^{bg})}{A_j \mathscr{L}} \tag{9.5}$$

A_j is the acceptance for true bin j. Figure 4 in paper V shows plots of the effective acceptance as a function of $m_{t\bar{t}}$, $p_{\mathrm{T},t\bar{t}}$ and $y_{t\bar{t}}$. Only statistical uncertainties are included. Table 2 in paper V show the acceptance in the final bins used in the unfolding step.

M is estimated from simulated $t\bar{t}$ events, and it has to be invertible in order for the unfolding procedure to work. The bins are chosen to be broader than the resolution of the variable in question, to make sure that the matrix is invertible, even under systematic shifts. To ensure a total probability, the following normalization is applied:

$$\sum_i M_{ij} = 1$$

After normalization, the diagonal elements are expected to have a value of about 0.68, corresponding to one standard deviation of the true variable. The normalization ensures that operation with the matrix preserves the L1 norm.

Systematic uncertainties affect the migration matrix (M), the acceptance (A) and the background estimate (N^{bg}). To propagate these uncertainties to the cross-section and to combine the measurements for the $e+$jets and $\mu+$jets channels, a method based on pseudo experiments was devised, see section 5.2. The method was implemented in a tool-kit called CASE[2]. This method

[2]Combination And Systematics Evaluation tool, developed by colleagues at Stockholm University.

also takes the statistical uncertainties in the two channels into account. Each source of systematic uncertainty is associated with a normal distributed parameter: $d_k \sim \mathcal{N}(0,1)$. The quantities in eq. (9.5), N^{bg}, A and M are then Taylor expanded about d_k, and only linear terms are kept. Assuming Poisson statistics for measurements in bin i, the cross-section formula can be written:

$$\sigma_j = \frac{\sum_i M_{ij}^{-1}(\vec{d})(Po(N_j^{data}) - N^{bg}(\vec{d}))}{A_j(\vec{d})\mathscr{L}(\vec{d})} \tag{9.6}$$

For each pseudo experiment, the parameters $d_0 \ldots d_n$ are picked at random from $\mathcal{N}(0,1)$ and the cross-section is computed for each bin and channel.

To reduce the impact of systematic uncertainties the quantity estimated is the relative differential cross-section $\frac{\sigma_j}{\sigma_{total}}$, where the total cross-section (σ_{total}) is computed as:

$$\sigma_{total} = \frac{Po(N^{data}) - N^{bg}(\vec{d})}{A(\vec{d})\mathscr{L}(\vec{d})}$$

where A is the total effective acceptance and N^{data} is the total number of measured events in data. Estimates from $e+$jets and $\mu+$jets are then combined with a BLUE[3] that uses the covariance matrix (C_j) between $\sigma_j^e/\sigma_{total}$ and $\sigma_j^\mu/\sigma_{total}$:

$$\frac{\sigma_j}{\sigma_{total}} = \frac{1}{w_j}(1,1)C_j^{-1}\begin{pmatrix} \sigma_j^e/\sigma_{total} \\ \sigma_j^\mu/\sigma_{total} \end{pmatrix} \qquad w_j = (1,1)C_j^{-1}\begin{pmatrix} 1 \\ 1 \end{pmatrix}$$

The covariance matrix C is estimated from pseudo experiments using simulation of $t\bar{t}$. The result for each bin is the median of $\frac{\sigma_j}{\sigma_{total}}$ together with the 68% confidence limits.

9.7 Results

The final unfolded results for $m_{t\bar{t}}$, $p_{\mathrm{T},t\bar{t}}$ and $y_{t\bar{t}}$ are shown in Figure 5 of paper V. In the first plot the $m_{t\bar{t}}$ result is compared to theoretical predictions from two cross-section integrators: MCFM that produces a result at NLO, and a special MC [70] that provides a result at NLO+NNLL accuracy. The second plot shows the same result for $m_{t\bar{t}}$ compared to two event generators with parton showering, MC@NLO and ALPGEN. The other two plots show the results for $p_{\mathrm{T},t\bar{t}}$ and $y_{t\bar{t}}$. Here the comparison is between MC integration at NLO with MCFM and event generation by MC@NLO and ALPGEN. An overview of the impact of all uncertainties is shown in Table 4 of paper V. One noticeable thing is that the systematic uncertainties dominate over the statistical, even in

[3] Best Linear Unbiased Estimate

the high mass bins, were statistics is low. Jet systematics, including JES and JER, are large contributors together with the generator systematics, especially ISR/FSR.

The measured differential cross-sections agree with the SM predictions, within uncertainties. The total cross-section is also measured and its value agree with the corresponding SM prediction. See chapter 10 for a comparison of the total cross-section to the other values presented in this thesis.

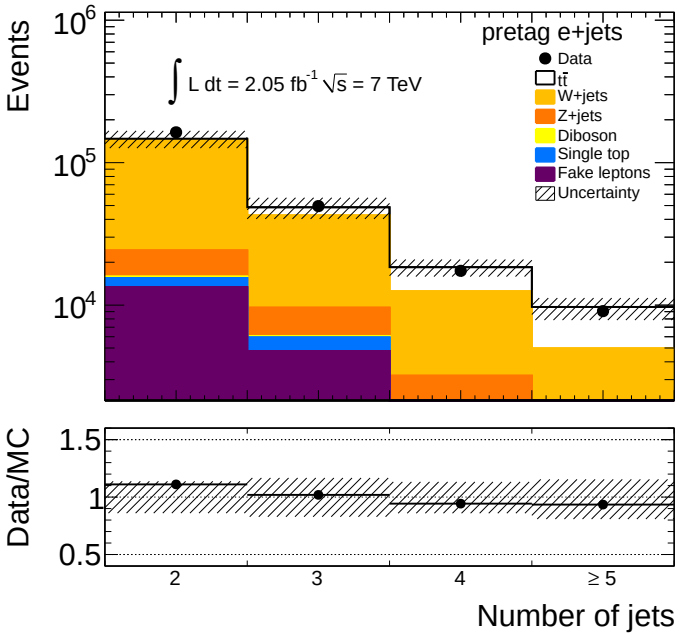

(a) $e+$jets

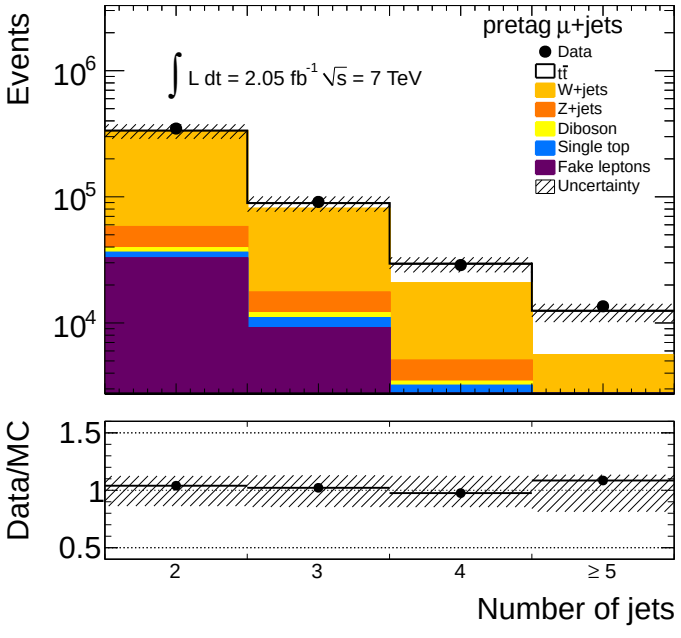

(b) $\mu+$jets

Figure 9.5: Jet multiplicity distributions in the $t\bar{t}$ signal region with a relaxed cut on jet multiplicity and without b-tagging requirement, for $e+$jets (top) and $\mu+$jets (bottom). All uncertainties except for theoretical uncertainties are included.

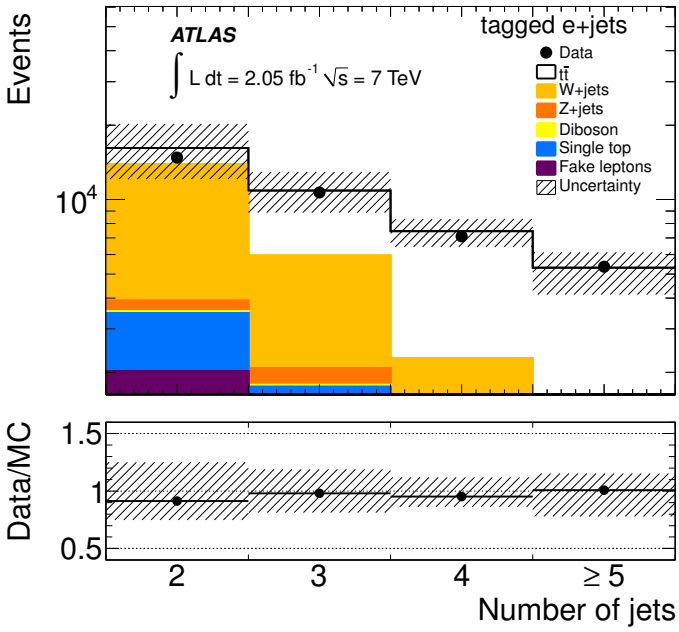

(a) $e+$jets

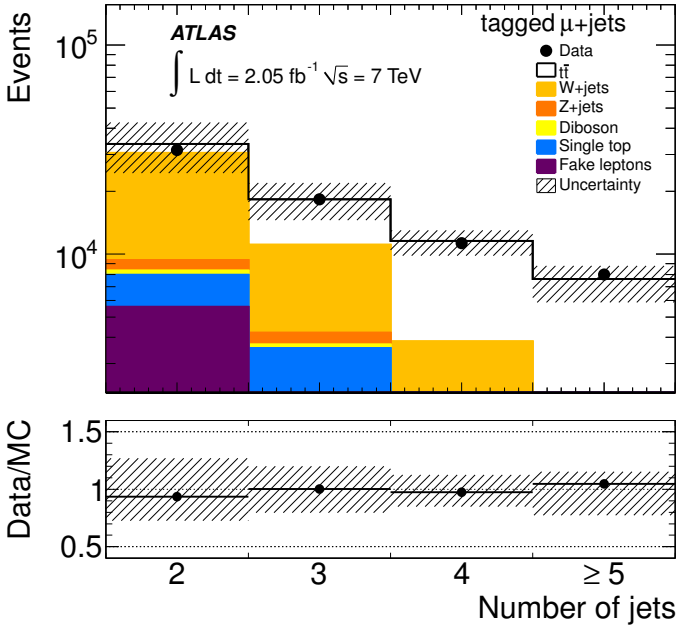

(b) $\mu+$jets

Figure 9.6: Jet multiplicity distributions in the $t\bar{t}$ signal region with a relaxed cut on jet multiplicity, for $e+$jets (top) and $\mu+$jets (bottom). All uncertainties except for theoretical uncertainties are included.

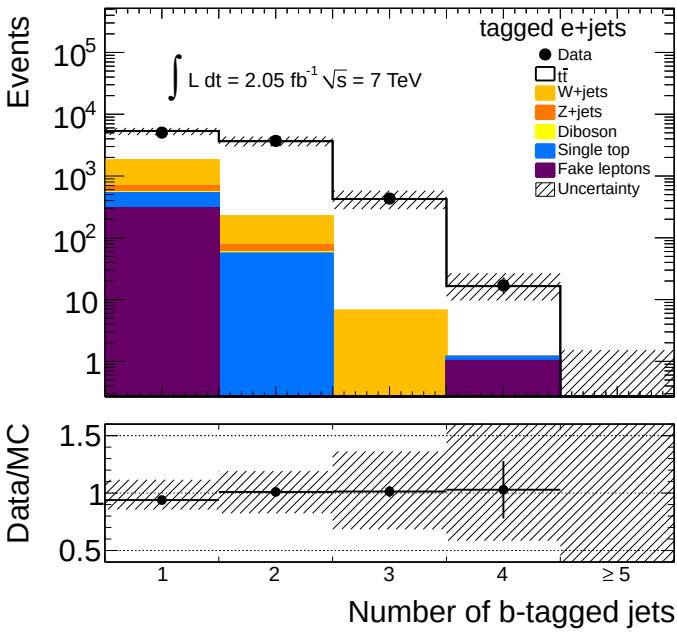

(a) $e+$jets

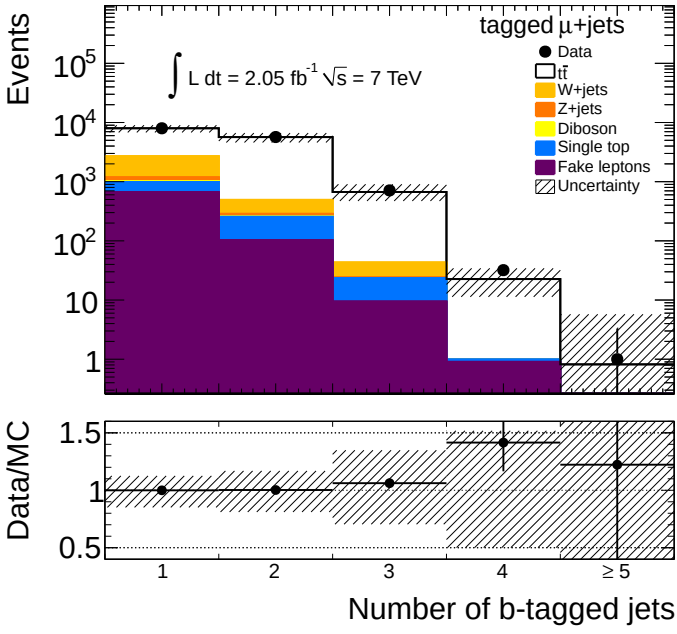

(b) $\mu+$jets

Figure 9.7: b-tagged jet multiplicity distributions in the $t\bar{t}$ signal region, for $e+$jets (top) and $\mu+$jets (bottom). All uncertainties except for theoretical uncertainties are included.

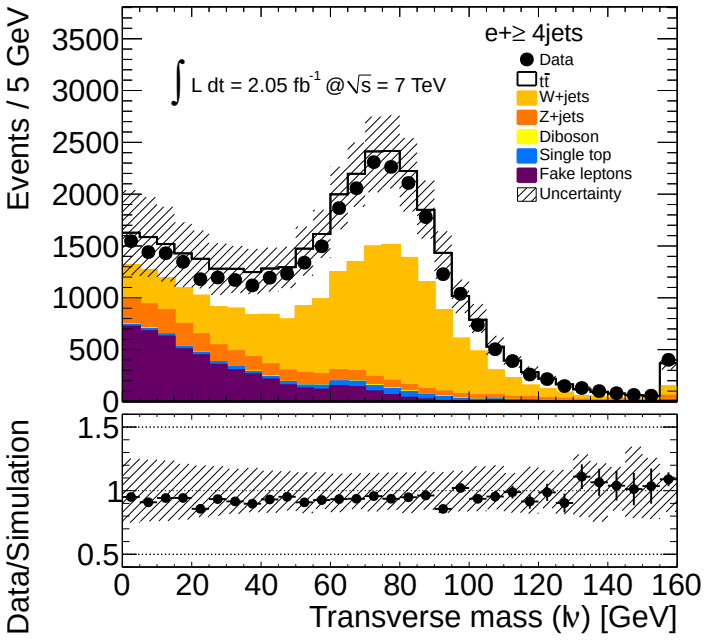

(a) $e+$jets

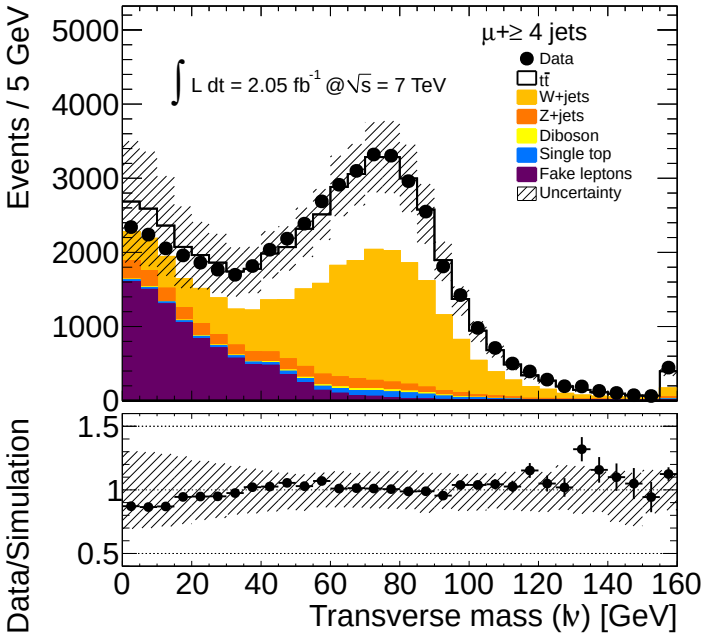

(b) $\mu+$jets

Figure 9.8: Transverse mass distributions in the $t\bar{t}$ signal region with a relaxed cut on jet m_{T} and without b-tagging requirement, for $e+$jets (top) and $\mu+$jets (bottom). All uncertainties except for theoretical uncertainties are included.

10 Conclusions and outlook

10.1 Summary

This thesis has presented measurements of the $t\bar{t}$ cross-section in both the ℓ + jets and di-lepton channels. Both channels have their strengths and weaknesses. The ℓ + jets channel has a large irreducible W + jets background but much higher branching ratio and it also offers the possibility to make a more accurate reconstruction of the parton four-momenta, since the di-lepton channel has got two neutrinos in the final state. The di-lepton channel has low background, especially in the $e\mu$ channel, but suffers from a small branching fraction, 6.5% compared to 47.8% for ℓ + jets. The Z + jets process is both an asset and a great problem; it provides a clean control region for performance measurements, but it contaminates the signal region in both channels. All measured values agree with the corresponding SM prediction, within uncertainties.

10.2 Total cross-section measurements

Figure 10.1 shows an overview of the cross-section measured in each di-lepton channel for the three dedicated $t\bar{t}$ cross-section measurements. Results from the template cross-section measurement, chapter 8, are also included for the $e\mu$ channel, both for the case when WW and $Z \to \tau^+\tau^-$ are constrained to 15% of their theoretical predictions (b), and when they are unconstrained (c). The theoretical computation (a) is made with HATHOR v1.2 [19] and the uncertainties from scale shifts and PDF:s are added linearly to give the total theoretical uncertainty. One thing to note is that the $e\mu$ channel by itself is very strong, (b) to (f), i.e. it has both low statistical and systematic uncertainties compared to the other di-lepton channels.

An overview of the final combined cross-section measurements is shown in Figure 10.2. Here the total cross-section estimated in the differential cross-section measurement (h) has been included as well as the results from the template measurement, (e) and (f). There is a trend towards higher cross-section values in the measurements, not significant however. Recent theoretical developments [71] give a higher cross-section (b) and almost no uncertainty due to scale shifts, one of the motivations behind the Principle of Maximum Conformality (PCM) used to set the renormalization scale in the computations.

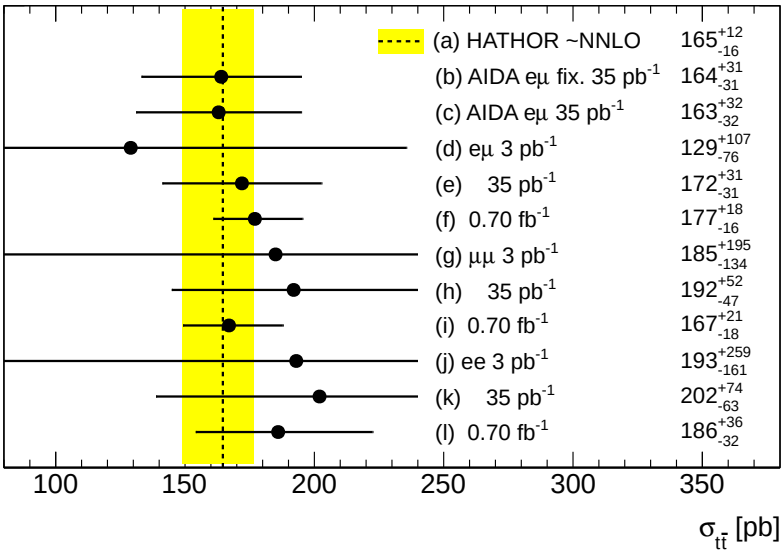

Figure 10.1: Results for total $t\bar{t}$ cross-section measurements in each di-lepton channel.

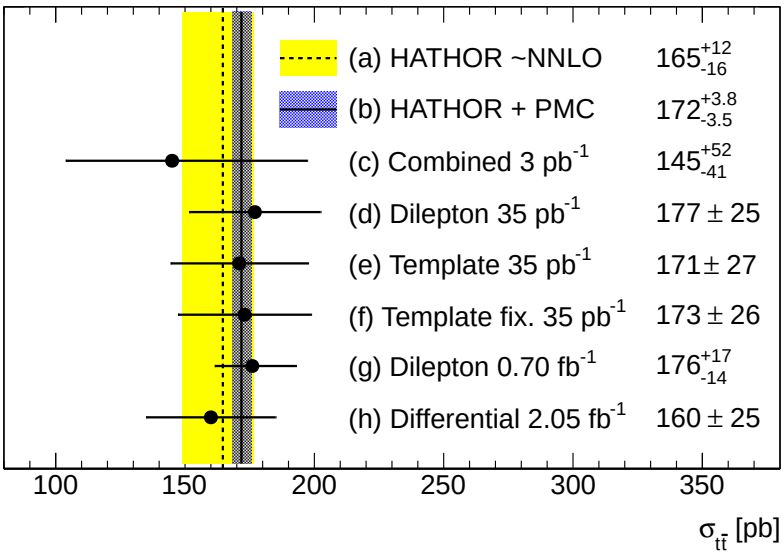

Figure 10.2: Combined results for total $t\bar{t}$ cross-section measurements.

10.3 Fake lepton estimation

Getting a reliable estimate of the fake lepton background is a difficult problem. Since the fake rate is highly dependent on the loose lepton definition, this has to be chosen with care. The dependency enters in three major ways; first in the

measurement of the raw rate, then in the extrapolation procedure and finally in the yield determination from the loose signal sample.

Two methods for estimating the fake yield in the di-lepton final state were presented in chapter 6. Using the freedom to choose the loose definition, two significantly different loose leptons were chosen and the fake rates and reconstruction efficiencies determined from data. The definition leading to a high rate was tested in the $\ell+$jets final state, and the result agreed with data. Next, the estimates from both methods were used on the di-lepton final state. The results for the high rate gave a higher estimate in the low $E_{\mathrm{T}}^{\mathrm{miss}}$ and jet multiplicity regions, but the methods agreed in the high $E_{\mathrm{T}}^{\mathrm{miss}}$ and jet multiplicity region that is dominated by $t\bar{t}$.

An approximation that has been implicitly made is that the di-lepton matrix method ignores TTL events, that are included in the signal region selection. A possible extension of the method is to add the *three* lepton fake estimate, transformed to the TTL basis, to the two lepton result, to get a more accurate di-lepton estimate. Adding a veto on additional loose leptons is another solution, but this has the unfortunate drawback of introducing a dependency on the loose lepton definition in the final analysis.

The matrix method itself as well as the implementation and evaluations have proven successful. This is evident from the fact that the resulting estimates were used in other top analyses [5, 6] besides the top cross-section analyses. However, greater accuracy and lower uncertainties on the estimate will likely be required in the future, which means that the method will be continuously updated and refined.

Higher instantaneous luminosity will require tighter trigger object definitions, to meet the trigger budget; but the matrix method needs a significantly looser lepton definition, with respect to the analysis lepton definition, in order to work. New strategies might soon be needed to work around the problems posed by increased instantaneous luminosity and tighter trigger definitions.

10.4 Differential cross-section measurement

Chapter 9 summarized the measurement of the relative differential cross-section for $t\bar{t}$, from paper V. Much effort went into finding a method that minimized the bias and the uncertainties. The unfolding technique with matrix inversions provided a method with low bias, since it does not rely on regularization, such as comparable methods like SVD unfolding [72]. The small bias was verified in pseudo experiments with $t\bar{t}$ baseline MC, and in tests with artificially enhanced signal in single bins.

A big fraction of the systematic uncertainties come from ISR/FSR, but a recent published measurement of $t\bar{t}$ production with a veto on extra central jets from ATLAS [5] shows that the current shift with the Perugia tune [69] is

too conservative in the top sector. The measurement in reference [5] constrains the ISR/FSR variations to a narrower interval.

The slight tension seen between the unfolded rapidity distribution in Figure 5.d in paper V, and the simulated distribution was first though to be due to the lack of higher order emissions in the cross-section integrator result, but a comparison to results from ALPGEN still shows some discrepancies, not significant however. The measured and simulated mass and p_{T} distributions, Figure 5 in paper V agree. For p_{T} there is a (non significant) tendency for MC@NLO to agree better with the measured values in the low p_{T} bins, which is expected since that region is highly sensitive to soft parton radiation mainly through ISR. These effects are in general better handled by event generators with parton showers than a cross-section integrator with resummation, because the former includes emissions of many low p_{T} partons.

Although the uncertainties are already dominated by systematics in many bins, the analysis can benefit from higher statistics. Increased luminosity together with an effort to reduce dominating systematics such as jet energy scale can improve the measurement. A higher centre of mass energy, together with increased statistics and lower systematics will enable the analysis to probe higher masses. There is however one phenomena that tends to get more problematic at higher masses and energies: the merging of jets and leptons. As the energy in the hard collision increases, the outgoing particles, quarks and leptons, gets boosted. This gives rise to merging of jets, and of leptons with jets. This was already seen in the analysis presented in this thesis, as an acceptance drop at high $t\bar{t}$ masses. A possible improvement of the analysis is to consider semi boosted final states, where two partons are allowed to merge. This would require a more complicated likelihood but could increase the acceptance in high mass bins.

10.5 Future top measurements

With the recent observation at the LHC of a new boson with a mass around 126 GeV, by both ATLAS [15] and CMS [16], the top sector will receive renewed attention. In order to establish if the observed boson is indeed the elusive Higgs boson, its couplings to other particles must be measured. Since Higgs couples to mass, and the top quark is the heaviest known particle, the Higgs-top couplings will be one of the most important quantities to study in the near future.

As new energy domains become available, and low energy regions exhaustively searched, boosted and semi-boosted analysis strategies have to be explored.

11 Bibliography

[1] The ATLAS Collaboration, "Measurement of the top quark-pair production cross section with ATLAS in pp collisions at $\sqrt{s} = 7$ TeV," *Eur.Phys.J.* **C71** (2011) 1577, arXiv:1012.1792 [hep-ex].

[2] The ATLAS Collaboration, "Measurement of the top quark pair production cross section with ATLAS in pp collisions at $\sqrt{s} = 7$ TeV in dilepton final states," Tech. Rep. ATLAS-CONF-2011-034, 2011.

[3] The ATLAS Collaboration, "Measurement of the top quark pair production cross section in pp collisions at sqrt(s) = 7 TeV in dilepton final states with ATLAS," *Phys.Lett.* **B707** (2012) 459–477, arXiv:1108.3699 [hep-ex].

[4] The ATLAS Collaboration, "Measurement of the cross section for top-quark pair production in pp collisions at sqrt(s) = 7 TeV with the ATLAS detector using final states with two high-pt leptons," *JHEP* **1205** (2012) 059, arXiv:1202.4892 [hep-ex].

[5] The ATLAS Collaboration, "Measurement of $t\bar{t}$ production with a veto on additional central jet activity in pp collisions at sqrt(s) = 7 TeV using the ATLAS detector," *Eur. Phys. J.* **C72** (2012) 2043, arXiv:1203.5015 [hep-ex].

[6] The ATLAS Collaboration, "Observation of spin correlation in $t\bar{t}$ events from pp collisions at sqrt(s) = 7 TeV using the ATLAS detector," *Phys.Rev.Lett.* **108** (2012) 212001, arXiv:1203.4081 [hep-ex].

[7] The ATLAS Collaboration, "Measurements of top quark pair relative differential cross-sections with ATLAS in pp collisions at $\sqrt{s} = 7$ TeV," arXiv:1207.5644 [hep-ex].

[8] K. Gellerstedt, "Data Driven Estimates of Dilepton Final State Backgrounds in ATLAS," Tech. Rep. CERN-THESIS-2011-249, 2011.

[9] B. Martin and G. Shaw, *Particle Physics*. Wiley, second ed., 1997.

[10] F. Mandl and G. Shaw, *Quantum Field Theory*. John Wiley & Sons, revised ed., 1993.

[11] M. E. Peskin and D. V. Schroeder, *An Introduction to Quantum Field Theory*. Westview Press, 1995.

[12] K. Nakamura et al., "(Particle Data Group)," *J. Phys. G* **37** (2010) 075021.

[13] D. Griffiths, *Introduction to elementary particles*. Wiley, 1987.

[14] G. 't Hooft, "Symmetry Breaking through Bell-Jackiw Anomalies," *Phys. Rev. Lett.* **37** (Jul, 1976) 8–11. http://link.aps.org/doi/10.1103/PhysRevLett.37.8.

[15] The ATLAS Collaboration, "Observation of a new particle in the search for the Standard Model Higgs boson with the ATLAS detector at the LHC," *Phys.Lett.B* (2012) , arXiv:1207.7214 [hep-ex].

[16] The CMS Collaboration, "Observation of a new boson at a mass of 125 GeV with the CMS experiment at the LHC," *Phys.Lett.B* (2012) , arXiv:1207.7235 [hep-ex].

[17] J.C. Collins, D.E. Soper and G. Sterman, "Factorization for one-loop corrections in the Drell-Yan process," *Nucl. Phys. B* **223** (1983) 381.

[18] J.C. Collins and D.E. Soper, "Back-to-back jets in QCD," *Nucl. Phys. B* **193** (1981) 381.

[19] M. Aliev *et al.*, "– HATHOR – HAdronic Top and Heavy quarks crOss section calculatoR," arXiv:1007.1327 [hep-ph].

[20] J. M. Campbell and R. K. Ellis, "An Update on vector boson pair production at hadron colliders," *Phys.Rev.* **D60** (1999) 113006, arXiv:hep-ph/9905386 [hep-ph].

[21] T. Sjöstrand, S. Mrenna and P.Z. Skands, "PYTHIA 6.4 Physics and Manual," *JHEP* **05** (2006) 026, arXiv:0603175 [hep-ph].

[22] S. Frixione and B. R. Webber, "Matching NLO QCD computations and parton shower simulations," *JHEP* **0206** (2002) 029, arXiv:0204244 [hep-ex].

[23] M. L. Mangano, M. Moretti, F. Piccinini, R. Pittau and A. D. Polosa, "ALPGEN, a generator for hard multiparton processes in hadronic collisions," *JHEP* **0307** (2003) 001, arXiv:0206293 [hep-ph].

[24] G. Corcella *et al.*, "HERWIG 6.5: an event generator for Hadron Emission Reactions With Interfering Gluons (including supersymmetric processes)," *JHEP* **01** (2001) 010, arXiv:0011363 [hep-ph].

[25] G. Corcella *et al.*, "HERWIG 6.5 release notes," arXiv:0210213 [hep-ph].

[26] S. Frixione and B. R. Webber, "Matching NLO QCD and parton showers in heavy flavour production," *JHEP* **0308** (2003) 007, arXiv:0305252 [hep-ex].

[27] S. Frixione, E. Laenen and P. Motylinski, "Single-top production in MC@NLO," *JHEP* **0603** (2006) 092, arXiv:0512250 [hep-ex].

[28] P.M. Nadolsky *et al.*, "Implications of CTEQ global analysis for collider observables," *Phys. Rev. D* **78** (2008) 013004, arXiv:0802.0007 [hep-ph].

[29] R. Haag, J. T. Lopuszański and M. Sohnius, "All possible generators of supersymmetries of the S-matrix," *Nucl. Phys. B* **88** (1975) 257–274.

[30] The ATLAS Collaboration, "Luminosity Determination in pp Collisions at sqrt(s)=7 TeV Using the ATLAS Detector at the LHC," *Eur.Phys.J.* **C71** (2011) 1630, arXiv:1101.2185 [hep-ex].

[31] The ATLAS Collaboration, "The ATLAS Experiment at the CERN Large Hadron Collider," *JINST* **3** (2008) S08003.

[32] The ATLAS Collaboration, "The ATLAS Simulation Infrastructure," *Eur. Phys. J.* **516 C 70** (2010) 823–874, arXiv:1005.4568 [physics.ins-det].

[33] S. Agostinelli, et al., "Geant4 – a simulation toolkit," *Nucl. Instr Meth. A* **506** (2003) 250.

[34] J. Allison, et al., "Geant4 developments and applications," *IEEE Transactions on Nuclear Science 53 No. 1* (2006) 270–278.

[35] C. Clément, B. Nordkvist, O. Solovyanov, I. Vivarelli, "Time Calibration of the ATLAS Hadronic Tile Calorimeter using the Laser System," Tech. Rep. ATL-TILECAL-PUB-2009-003, 2009.

[36] The ATLAS Collaboration, "Expected Performance of the ATLAS Experiment - Detector, Trigger and Physics," arXiv:0901.0512 [hep-ex].

[37] G. Cowan, *Statistical Data Analysis*. Oxford University Press, 2002.

[38] The ATLAS Collaboration, "Electron performance measurements with the ATLAS detector using the 2010 LHC proton-proton collision data," *Eur.Phys.J.* **C72** (2012) 1909, arXiv:1110.3174 [hep-ex].

[39] M. Cacciari, G. P. Salam and G. Soyes, "The anti-k_t jet clustering algorithm," *JHEP* **04** (2008) 063.

[40] M. Cacciari and G. P. Salam, "Dispelling the N^3 myth for the k_t jet finder," *Phys. Lett. B* **641** (2006) 57–61.

[41] M. Cacciari, G. P. Salam and G. Soyes, "The fastjet web page." http://fastjet.fr/.

[42] The ATLAS Collaboration, "Jet energy measurement with the ATLAS detector in proton-proton collisions at sqrt(s) = 7 TeV," arXiv:1112.6426 [hep-ex].

[43] The ATLAS Collaboration, "Performance of Missing Transverse Momentum Reconstruction in Proton-Proton Collisions at 7 TeV with ATLAS," *Eur.Phys.J.* **C72** (2012) 1844, arXiv:1108.5602 [hep-ex].

[44] N. Kidonakis, "Next-to-next-to-leading-order collinear and soft gluon corrections for t-channel single top quark production," *Phys.Rev.* **D83** (2011) 091503, arXiv:1103.2792 [hep-ph].

[45] N. Kidonakis, "NNLL resummation for s-channel single top quark production," *Phys.Rev.* **D81** (2010) 054028, arXiv:1001.5034 [hep-ph].

[46] N. Kidonakis, "Two-loop soft anomalous dimensions for single top quark associated production with a W- or H-," *Phys.Rev.* **D82** (2010) 054018, arXiv:1005.4451 [hep-ph].

[47] C. Anastasiou *et al.*, "High precision QCD at hadron colliders: Electroweak gauge boson rapidity distributions at NNLO," *Phys.Rev.* **D69** (2004) 094008, arXiv:hep-ph/0312266 [hep-ph].

[48] The ATLAS Collaboration, "Expected electron performance in the ATLAS experiment," Tech. Rep. ATL-PHYS-PUB-2011-006, 2011.

[49] The ATLAS Collaboration, "Calibrating the b-Tag and Mistag Efficiencies of the SV0 b-Tagging Algorithm in 3/pb of Data with the ATLAS Detector," Tech. Rep. ATLAS-CONF-2010-099, 2010.

[50] The ATLAS Collaboration, "Impact parameter-based b-tagging algorithms in the 7 TeV collision data with the ATLAS detector: the TrackCounting and JetProb algorithms," Tech. Rep. ATLAS-CONF-2010-041, 2010.

[51] The ATLAS Collaboration, "Commissioning of the ATLAS high-performance b-tagging algorithms in the 7 TeV collision data," Tech. Rep. ATLAS-CONF-2011-102, 2011.

[52] C. Degrande *et al.*, "Non-resonant New Physics in Top Pair Production at Hadron Colliders," *JHEP* **1103** (2011) 125, arXiv:1010.6304 [hep-ph].

[53] C. Zhang and S. Willenbrock, "Effective-Field-Theory Approach to Top-Quark Production and Decay," *Phys.Rev.* **D83** (2011) 034006, arXiv:1008.3869 [hep-ph].

[54] The ATLAS Collaboration, "Updated luminosity determination in pp collisions at sqrt(s) = 7 TeV using the ATLAS detector," Tech. Rep. ATLAS-CONF-2011-011, 2011.

[55] P. Nason, "A new method for combining NLO QCD with shower Monte Carlo algorithms," *JHEP* **11546** (2004) 040, arXiv:0409146 [hep-ph].

[56] S. Frixione, P. Nason, and C. Oleari, "Matching NLO QCD computations with Parton Shower simulations: the POWHEG method," *JHEP* **11** (2007) 070, arXiv:07092092 [hep-ph].

[57] S. Frixione, P. Nason, and G. Ridolfi, "A Positive-Weight Next-to-Leading-Order Monte Carlo for Heavy Flavour Hadroproduction," *JHEP* **09** (2007) 126, arXiv:07073088 [hep-ph].

[58] B.P. Kersevan and E. Richter-Wąs, "The Monte Carlo event generator AcerMC version 2.0 with interfaces to PYTHIA 6.2 and HERWIG 6.5," (2004) , arXiv:0405247 [hep-ph].

[59] A. D. Martin, W. J. Stirling, R. S. Thorne, and G. Watt, "Parton distributions for the LHC," *Eur. Phys. J. C* **63** (2009) 189–285, arXiv:0901.0002 [hep-ph].

[60] R. D. Ball *et al.*, "A first unbiased global NLO determination of parton distributions and their uncertainties," *Nucl. Phys. B* **838** (2010) 136–206, arXiv:1002.4407 [hep-ph].

[61] R. Barlow and C. Beeston, "Fitting using finite Monte Carlo samples," *Comp. Phys. Comm.* **77** (1993) 219–228.

[62] The CMS Collaboration, "First Measurement of W+W- production and Search for Higgs Boson in pp Collisions at sqrt(s) = 7 TeV," Tech. Rep. CERN-PH-EP-2011-015; CMS-EWK-10-009-004, CERN, Geneva, Feb, 2011.

[63] The ATLAS Collaboration, "Measurement of the Z to tau tau Cross Section with the ATLAS Detector," *Phys.Rev.* **D84** (2011) 112006, arXiv:1108.2016 [hep-ex].

[64] The ATLAS Collaboration, "Measurement of the charge asymmetry in top quark pair production in pp collisions at sqrt(s) = 7 TeV using the ATLAS detector," arXiv:1203.4211 [hep-ex].

[65] R. E. Kalman, "A new approach to linear filtering and prediction problems," *Journal Of Basic Engineering* **82** (1960) 35–45.

[66] C. Kom and W. J. Stirling, "Charge asymmetry in W + jets production at the LHC," *Eur.Phys.J.* **C69** (2010) 67–73, arXiv:1004.3404 [hep-ph].

[67] S. Bern *et al.*, "Left-Handed W Bosons at the LHC," *Phys.Rev.* **D84** (2011) 034008, arXiv:1103.5445 [hep-ph].

[68] M. Botje *et al.*, "The PDF4LHC Working Group Interim Recommendations," arXiv:1101.0538 [hep-ph].

[69] P. Z. Skands, "Tuning Monte Carlo Generators: The Perugia Tunes," *Phys.Rev.* **D82** (2010) 074018, arXiv:1005.3457 [hep-ph].

[70] V. Ahrens and others., "Renormalization-Group Improved Predictions for Top-Quark Pair Production at Hadron Colliders," *JHEP* **097** (2010) , arXiv:1003.5827.

[71] S. J. Brodsky and X.-G. Wu, "Application of the Principle of Maximum Conformality to Top-Pair Production," *Phys.Rev.* **D86** (2012) 014021, arXiv:1204.1405 [hep-ph].

[72] A. Hocker and V. Kartvelishvili, "SVD approach to data unfolding," *Nucl.Instrum.Meth.* **A372** (1996) 469–481, arXiv:hep-ph/9509307 [hep-ph].

[73] K. Melnikov and F. Petriello, "Electroweak gauge boson production at hadron colliders through O(alpha(s)**2)," *Phys.Rev.* **D74** (2006) 114017, arXiv:hep-ph/0609070 [hep-ph].